



ATATURK
UNIVERSITY
PUBLICATIONS

Journal of Anatolian Physics *and* Astronomy

Official Journal of Atatürk University Faculty of Science

Volume 3 Issue 2 December 2024

EISSN 2791-8718

<https://dergipark.org.tr/en/pub/japa>

Journal of Anatolian Physics and Astronomy

CHIEF EDITOR / BAŐ EDITÖR

Erdem ŐAKAR 

Science Faculty, Department of Physics,
Atatürk University, Erzurum, Turkey
*Fen Fakóltesi, Fizik Bölümü, Atatürk
Üniversitesi, Erzurum, Türkiye*

ASSOCIATE EDITORS / YARDIMCI EDITÖRLER

Yakup KURUCU 

Science Faculty, Department of Physics,
Atatürk University, Erzurum, Turkey
*Fen Fakóltesi, Fizik Bölümü, Atatürk
Üniversitesi, Erzurum, Türkiye*

Bekir GÖRBULAK 

Science Faculty, Department of Physics,
Atatürk University, Erzurum, Turkey
*Fen Fakóltesi, Fizik Bölümü, Atatürk
Üniversitesi, Erzurum, Türkiye*

Ganim GEÇİM 

Science Faculty, Department of Astronomy
and Astrophysics, Atatürk University,
Erzurum, Turkey
*Fen Fakóltesi, Astronomi ve Astrofizik
Bölümü, Atatürk Üniversitesi, Erzurum,
Türkiye*

Elif DAŐ 

Science Faculty, Department of Physics,
Atatürk University, Erzurum, Turkey
*Fen Fakóltesi, Fizik Bölümü, Atatürk
Üniversitesi, Erzurum, Türkiye*

Melek FIDAN 

Science Faculty, Department of Physics,
Atatürk University, Erzurum, Turkey
*Fen Fakóltesi, Fizik Bölümü, Atatürk
Üniversitesi, Erzurum, Türkiye*

Aykut ÖZDÖNMEZ 

Science Faculty, Department of Astronomy
and Astrophysics, Atatürk University,
Erzurum, Turkey
*Fen Fakóltesi, Astronomi ve Astrofizik
Bölümü, Atatürk Üniversitesi, Erzurum,
Türkiye*

ADVISORY BOARD / DANIŐMA KURULU

Ali GÖROL

Science Faculty, Department of Physics,
Atatürk University, Erzurum, Turkey
*Fen Fakóltesi, Fizik Bölümü, Atatürk
Üniversitesi, Erzurum, Türkiye*

Emre GÜR

Department of Turkish Language and
Literature, Gazi University, Ankara, Turkey
*Gazi Üniversitesi, Türk Dili ve Edebiyatı
Bölümü, Ankara, Türkiye*

Mehmet ERTUĞRUL

Department of Turkish Language and
Literature, Fırat University, Elazığ, Turkey
*Fırat Üniversitesi, Türk Dili ve Edebiyatı
Bölümü, Elazığ, Türkiye*

Orhan İÇELLİ

Department of Turkish Language and
Literature, Trakya University, Trakya, Turkey
*Trakya Üniversitesi, Türk Dili ve Edebiyatı
Bölümü, Edirne, Türkiye*

Cahit YEŐİLYAPRAK

Department of History, Yeditepe University,
Turkey
*Yeditepe Üniversitesi, Tarih Bölümü, İstanbul,
Türkiye*

Lorent JOLISSAINT

Department of Social Sciences and Turkish
Education, Yıldız Technical University,
İstanbul, Turkey
*Yıldız Teknik Üniversitesi, Sosyal Bilimler ve
Türkçe Eğitimi Bölümü, İstanbul, Türkiye*

FOREIGN LANGUAGE

CONSULTANTS /

YABANCI DİL DANIŐMANLARI

Erdinç ÖZ

Science Faculty, Department of Physics,
Atatürk University, Erzurum, Turkey
*Fen Fakóltesi, Fizik Bölümü, Atatürk
Üniversitesi, Erzurum, Türkiye*

Aykut ÖZDÖNMEZ

Science Faculty, Department of Astronomy
and Astrophysics, Atatürk University,
Erzurum, Turkey
*Fen Fakóltesi, Astronomi ve Astrofizik
Bölümü, Atatürk Üniversitesi, Erzurum,
Türkiye*

Elif DAŐ

Science Faculty, Department of Physics,
Atatürk University, Erzurum, Turkey
*Fen Fakóltesi, Fizik Bölümü, Atatürk
Üniversitesi, Erzurum, Türkiye*

AyŐenur ÖZTÖRK AYDIN

Engineering Faculty, Department of Chemical
Engineering, Atatürk University, Erzurum,
Turkey
*Mühendislik Fakóltesi, Kimya Mühendisliđi
Bölümü, Atatürk Üniversitesi, Erzurum,
Türkiye*

About the Journal of Anatolian Physics and Astronomy

Journal of Anatolian Physics and Astronomy is a peer-reviewed, open-access, online-only journal published by Atatürk University.

The journal is published biannual in both Turkish, and English, with articles released in June, and December.

Abstracting and Indexing

Journal of Anatolian Physics and Astronomy is covered in the following abstracting and indexing databases;

- EBSCO

Aims

Journal of Anatolian Physics and Astronomy aims to contribute to the literature by publishing manuscripts at the highest scientific level in physics and astronomy. The journal publishes original articles, and reviews that are prepared in accordance with ethical guidelines.

Scope and Audience

The scope of the journal includes but not limited to relevant to the topics of atomic and molecular physics, condensed matter physics, nuclear physics, particle, physics, quantum physics, optical physics, biophysics, thermodynamics, astrophysics, astronomical techniques and methods, galaxies, gravitation and cosmology, planets, comets, solar and stellar physics, space and all other related interdisciplinary theoretical researches.

The target audience of the journal includes researchers and specialists who are interested or working in all fields in the journal's scope.

Disclaimer

Statements or opinions expressed in the manuscripts published in the journal reflect the views of the author(s) and not the opinions of the editors, editorial board, and/or publisher; the editors, editorial board, and publisher disclaim any responsibility or liability for such materials.

Open Access Statement

Journal of Anatolian Physics and Astronomy is an open access publication. Starting on June 2024, all content published in the journal is licensed under the Creative Commons Attribution-NonCommercial (CC BY-NC) 4.0 International License which allows third parties to use the content for non-commercial purposes as long as they give credit to the original work. This license allows for the content to be shared and adapted for non-commercial purposes, promoting the dissemination and use of the research published in the journal. All published content is available online, free of charge at <https://dergipark.org.tr/en/pub/japa>. When using previously published content, including figures, tables, or any other material in both print and electronic formats, authors must obtain permission from the copyright holder. Legal, financial and criminal liabilities in this regard belong to the author(s).

You can find the current version of the Instructions to Authors at <https://dergipark.org.tr/en/pub/japa/writing-rules>



Contact (Editor in Chief) / İletişim (Baş Editör)

Erdem ŞAKAR

Science Faculty, Department of Physics,
Atatürk University, Erzurum, Turkey
*Fen Fakültesi, Fizik Bölümü, Atatürk Üniversitesi,
Erzurum, Türkiye*

✉ erdem@atauni.edu.tr

✉ japa@atauni.edu.tr

🌐 <https://dergipark.org.tr/en/pub/japa>

☎ +90 442 231 41 72

Contact (Publisher) / İletişim (Yayıncı)

Atatürk University

Atatürk University, Erzurum, Turkey
Atatürk Üniversitesi Rektörlüğü 25240 Erzurum, Türkiye

✉ ataunijournals@atauni.edu.tr

🌐 <https://bilimseldergiler.atauni.edu.tr>

☎ +90 442 231 15 16

Journal of Anatolian Physics and Astronomy Hakkında

Journal of Anatolian Physics and Astronomy, Atatürk Üniversitesi tarafından yayınlanan hakemli, açık erişimli, yalnızca çevrimiçi bir dergidir.

Dergi, Haziran ve Aralık aylarında olmak üzere Türkçe ve İngilizce olarak yılda iki kez yayınlanmaktadır.

Özetleme ve İndeksleme

Journal of Anatolian Physics and Astronomy aşağıdaki özetleme ve indeksleme veri tabanlarında yer almaktadır:

- EBSCO

Amaç

Journal of Anatolian Physics and Astronomy, fizik ve astronomi alanında en yüksek bilimsel düzeyde makaleler yayınlayarak literatüre katkıda bulunmayı amaçlamaktadır. Dergide etik kurallara uygun olarak hazırlanmış özgün makaleler ve derlemeler yayınlanmaktadır.

Kapsam ve Hedef Kitle

Derginin kapsamına atom ve moleküler fizik, yoğun madde fiziği, nükleer fizik, parçacık fizik, fizik, kuantum fiziği, optik fizik, biyofizik, termodinamik, astrofizik, astronomik teknik ve yöntemler, galaksiler, galaksiler, yerçekimi ve kozmoloji, gezegenler, kuyruklu yıldızlar, güneş ve yıldız fiziği, uzay ve ilgili tüm disiplinler arası teorik araştırmalar girmektedir.

Derginin hedef kitlesi, derginin kapsamına giren tüm alanlarla ilgilenen veya çalışan araştırmacı ve uzmanları içermektedir.

Sorumluluk Reddi

Dergide yayınlanan yazılarda ifade edilen ifadeler veya görüşler, editörlerin, yayın kurulunun ve/veya yayıncının görüşlerini değil, yazar(lar)ın görüşlerini yansıtır; editörler, yayın kurulu ve yayıncı bu tür materyaller için herhangi bir sorumluluk veya yükümlülük kabul etmemektedir.

Açık Erişim Bildirimi

Journal of Anatolian Physics and Astronomy açık erişimli bir dergidir. 2024 Haziran ayından itibaren dergide yayınlanan tüm içerik, Creative Commons Attribution-NonCommercial (CC BY-NC) 4.0 International License lisansı ile yayınlanmaktadır. Bu lisans, içeriğin ticari olmayan amaçlarla paylaşılmasını ve adapte edilmesini sağlayarak dergide yayınlanan araştırmaların yayılmasını ve kullanılmasını teşvik eder. Haziran 2024'ten önce yayınlanan içerik, geleneksel telif hakkı kapsamında lisanslanmıştı ancak arşiv ücretsiz olarak hâlâ erişime açıktır. Tüm yayımlanan içerikler <https://dergipark.org.tr/tr/pub/japa> adresinden çevrimiçi olarak ücretsiz olarak erişilebilir. Daha önce yayınlanmış içeriği, figürleri, tabloları veya diğer herhangi bir materyali basılı veya elektronik formatta kullanırken yazarlar, telif hakkı sahibinden izin almakla sorumludur. Bu konuda yasal, mali ve cezai sorumluluklar yazar(lara) aittir.

Yazarlara Bilgi'nin güncel versiyonuna <https://dergipark.org.tr/tr/pub/japa/writing-rules> adresinden ulaşabilirsiniz.



Contact (Editor in Chief) / İletişim (Baş Editör)

Erdem ŞAKAR

Science Faculty, Department of Physics,
Atatürk University, Erzurum, Turkey
*Fen Fakültesi, Fizik Bölümü, Atatürk Üniversitesi,
Erzurum, Türkiye*

✉ erdem@atauni.edu.tr

✉ japa@atauni.edu.tr

🌐 <https://dergipark.org.tr/en/pub/japa>

☎ +90 442 231 41 72

Contact (Publisher) / İletişim (Yayıncı)

Atatürk University

Atatürk University, Erzurum, Turkey
Atatürk Üniversitesi Rektörlüğü 25240 Erzurum, Türkiye

✉ ataunijournals@atauni.edu.tr

🌐 <https://bilimseldergiler.atauni.edu.tr>

☎ +90 442 231 15 16

CONTENTS / İÇİNDEKİLER

Research Articles/Araştırma Makaleleri

- 44** **Structural Characterisation of Grown InSe:Mn Semiconductors and Effect of Doped Manganese**
Büyütülen InSe:Mn Yarıiletkenlerin Yapısal Karakterizasyonu ve Katkılanan Manganezin Etkisi
Bekir GÜRBULAK, Mehmet Kürşat DUMANLI
- 52** **Synthesis, FT-IR, DFT and in silico Antibacterial Activity Studies of Silver Nitrate Complex of Chlorzoxazone**
Chlorzoxazone Molekülünün Gümüş Nitrat Bileşiğinin Sentezlenmesi, FT-IR, DFT ve in silico Antibakteriyel Çalışmaları
Mustafa Tuğfan BİLKAN, Zehra ÇAKIL, Elçin Özgür BÜYÜKATALAY
- 62** **Investigation of Photo-Electrical Properties in (Fe₂O₃-G)/n-Si Device**
(Fe₂O₃-G)/n-Si Cihazında Foto-Elektriksel Özelliklerin İncelenmesi
Elif DAŞ, Gamze BOZKURT
- 75** **Dosimetric Investigation of Acetaminophen Drug Raw Materials by Electron Paramagnetic Resonance Spectroscopy**
Acetaminophen İlaç Hammaddelerinin Elektron Paramanyetik Rezonans Spektroskopisi ile Dozimetrik İncelenmesi
Fırat AKBALIK

Review/Derleme

- 83** **Development of Lithium Ion Batteries From the History of Batteries to the Present and the Latest Technology Statement**
Lityum İyon Pillerin Tarihten Bugüne Gelişimi ve Son Teknolojide Geline Nokta
Hüseyin PEHLİVAN, Erdiç Öz, Muhammet YILDIRIM

Structural Characterisation of Grown InSe:Mn Semiconductors and Effect of Doped Manganese

Büyütülen InSe:Mn Yarıiletkenlerin Yapısal Karakterizasyonu ve Katkılanan Manganezin Etkisi

Bekir GÜRBULAK

Atatürk University, Department of Physics,
Faculty of Sciences, Erzurum, Turkey



Mehmet Kürşat DUMANLI

Atatürk University, Institute of Natural and
Applied Sciences, Department of Physics,
Erzurum, Turkey



Abstract

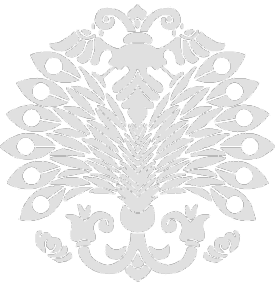
Scientific studies on binary semiconductors have been going on for half a century. The growth and research of semiconductors have contributed greatly to the advancement of semiconductor technology. Indium and selenium were synthesized from elements in stoichiometric ratios and doped with manganese. InSe and InSe:Mn single crystals were successfully grown by the Bridgman/Stockbarger crystal growth method. Since the surfaces of the grown samples do not contain contamination, chemical contamination was not caused by chemical treatment. Since the grown semiconductors have a layered structure, the samples were easily prepared for characteristic analyses along the 001 planes. The structure of the InSe and InSe:Mn semiconductors was analysed using x-ray diffractometers and energy dispersive X-ray techniques. An important study has been carried out on the structural properties of the grown InSe and InSe:Mn semiconductors. The hexagonal structure of the InSe semiconductor with lattice parameters $a = b = 4.025 \text{ \AA}$ and $c = 16.732 \text{ \AA}$ was confirmed with the help of X-ray diffraction. III-VI semiconductors are used in visible and infrared light-emitting diodes, infrared detectors, converters, amplifiers, optical parameter oscillators, and far infrared generator.

Keywords: Crystal Growth, InSe, InSe:Mn, Bridgman/Stockbarger Method, Structural Characterisation.

Öz

İkili yarıiletkenler üzerine yapılan bilimsel çalışmalar yarım asırdır devam etmektedir. Yarıiletkenlerin, büyütülmesi ve araştırılması yarıiletken teknolojisinin ilerlemesine büyük katkı sağlamıştır. İndiyum ve selenyum elementlerden stokiyometrik oranlarda sentezlenmiş ve manganez katkılanmıştır. InSe ve InSe:Mn tek kristalleri, Bridgman/Stockbarger kristal büyütme yöntemiyle başarıyla büyütülmüştür. Büyütülen numunelerin yüzeyleri kontaminasyon içermediğinden kimyasal işleme tabi tutulmayarak kimyasal kirlenmeye sebep olunmamıştır. Büyütülen yarıiletkenler tabakalı bir yapıya sahip olduğundan, numuneler kolayca (001) düzlemleri boyunca karakteristik analizler için hazırlanmıştır. InSe ve InSe:Mn yarı iletkenlerinin yapısı X-ışını difraktometresi ve enerji dağılımlı X-ışını teknikleri kullanılarak analiz edilmiştir. Büyütülen InSe ve InSe:Mn yarıiletkenlerin yapısal özellikleri üzerine önemli bir çalışma yapılmıştır. InSe yarıiletkeninin $a = b = 4.025 \text{ \AA}$ ve $c = 16.732 \text{ \AA}$ kafes parametrelerine sahip olan altıgen yapısı, X-ışını kırınımı yardımıyla doğrulanmıştır. III-VI yarıiletkenler, görünür ve kızılötesi ışık yayan diyotlarda, kızılötesi detektörlerde, dönüştürücülerde, yükselteçlerde, optik parametrelili osilatörlerde ve uzak kızılötesi jeneratörlerde kullanılmaktadır.

Anahtar Kelimeler: Kristal Büyütme, InSe, InSe:Mn, Bridgman/Stockbarger Yöntemi, Yapısal Karakterizasyon



Sorumlu Yazar/Corresponding Author:

B. Gürbulak

E-mail: gurbulak@atauni.edu.tr

Geliş Tarihi/Received 18.07.2024

Kabul Tarihi/Accepted 07.09.2024

Yayın Tarihi/ 12.12.2024

Publication Date

Cite this article

Gurbulak B. & Dumanlı M.K. (2024) Structural Characterisation of Grown InSe:Mn Semiconductors and Effect of Doped Manganese. *Journal of Anatolian Physics and Astronomy*, 3(2), 44-51.



Content of this journal is licensed under a Creative Commons Attribution-Noncommercial 4.0 International License.

Introduction

In recent years, solid and thin films grown by various growth techniques have attracted great interest in producing technological devices and solar cells. Various deposition techniques are employed for preparing thin films, including vacuum evaporation (El-Sayed, 2003), flash evaporation (Julien et al., 1990), chemical vapor deposition (Park et al., 2003), and van der Waals epitaxy (Lang et al., 1996). Among these methods, the electrodeposition technique stands out as an inexpensive, simple, and low-temperature option capable of producing high-quality films for device applications such as heterojunction devices and switching devices.

InSe single crystals have been grown by the Bridgman-Stockbarger method, starting from stoichiometric and non-stoichiometric melts (De Blasi et al., 1982). Semiconductors grown by the Bridgman/Stockbarger technique usually belong to the b and g modifications. Their unit cells crystallize in a hexagonal and rhombohedral structure (Camassel et al., 1978; Gürbulak 2004). InSe belongs to a large class of layered semiconductors in which a prototype of covalent or ionic forces extends in two dimensions instead of being three-dimensionally bonded as in group III-VI or III-V semiconductors (El-Moiz et al., 1993).

There are few studies available on the impurity levels in p-type InSe, with only group II elements Zn and Cd being used as dopants. Investigations into the impurity levels in Zn and Cd-doped InSe have employed deep-level transient spectroscopy (DLTS), photoluminescence (PL), and Hall-effect measurements. The 1.17 eV emission band observed in the Zn-doped sample can be explained by a self-activated luminescence process, which is described by a configurational coordinate model (Ikari et al., 1981). III-VI dilute magnetic semiconductors are formed by bonding a group III element to a group VI element and replacing some group III atoms with transition metal atoms. These transition metal atoms impart magnetic moments to the sample. III-VI dilute magnetic semiconductors are of great interest for electro-optical applications due to their high nonlinear optical properties. In InSe with 1.25 at % Mn, two magnetic subsystems containing Mn ions inside ionic-covalent layers and inside the interlayer van-der-Waals gap were discovered (Suhre et al., 1997; Errandonea et al., 1999; Watanabe et al., 2003; Slyn'ko et al., 2005a; Slyn'ko et al., 2005b).

For different studies, single crystals were grown by the Bridgman method from a non-stoichiometric melt with the composition $\text{In}_{1.03}\text{Se}_{0.97}$. Indium monoselenide single crystals were combined with magnesium from the vapor phase. Electron concentration, electron Hall mobility, anisotropic electrical conductivity, and thermoelectric power of the InSe semiconductor were measured as a function of temperature (Zaslonkin et al., 2006). The crystals have a g-polytype structure and n-type conductivity. In indium monoselenide, the interatomic bond between the layers is ionic-covalent, while the layers are connected by weak van der Waals forces (Kovalyuk et al., 2009). Different studies have been carried out with doped and undoped InSe semiconductors (Kaminskii, 2009; Boledzyuk et al., 2014; Ertap et al., 2019; Sang et al., 2019; Emir et al., 2024).

The aim of this research is to grow pure and doped InSe semiconductors by a modified Bridgman-Stockbarger method. On the other hand, to determine the structural changes induced by the doped manganese (Mn) element in the InSe compound.

Growth and Structural Characterization

The Bridgman-Stockbarger method is a growth technique widely used in the growth of semiconductors. The Bridgman-Stockbarger method is an improved version of the Bridgman method. The Bridgman-Stockbarger method involves cooling a molten alloy very slowly to form a single crystal. As the alloy solidifies, the temperature gradient within the furnace is used to promote controlled crystallization. The sample to be grown is placed in a crucible, usually made of graphite, alumina, or quartz materials that can withstand high temperatures. The vertical temperature gradient of the furnace is determined by the semiconductor to be grown. Growth furnaces usually have two zones. The upper zone is hotter and keeps the material melting, while the lower zone is cooler. The growth furnace heats the elements above the melting point. The temperature of the furnace is gradually reduced. During the formation of the compound, it is very important to control the sensitivity of the temperature change and the cooling rate. It provides a controlled solidification front that moves slowly from the bottom of the to the top. This causes the melting material to solidify from bottom to top. The slow cooling process helps to reduce

impurities and defects in the crystal.

Considering the studies (Shih et. al., 1986; Gürbulak, 2024), it was decided to grow InSe and InSe:Mn crystals using a single ampoule. Indium and selenium are prepared in ratios obtained by stoichiometric calculations. The lower end of the growth ampoule is shaped to be oval according to the layered structure, and the elements (In, Se, and Mn) are placed inside the bulb. The air in the growth ampoule is reduced to 10^{-6} Torr, and the end of the ampoule is sealed under vacuum. Movement up and down in the horizontal growth furnace is required to ensure homogeneity of the ampoule, InSe, and InSe:Mn-doped (0.003) mixture. InSe and InSe:Mn semiconductors were grown by a modified Bridgman-Stockbarger method under specified conditions.

It is very important that binary compounds are grown and the grown semiconductor is of a quality that can be used in scientific studies. In general, the Bridgman-Stockbarger method is a fundamental technique in materials science and engineering. It plays a critical role in the development of high-quality semiconductors for various scientific applications.

The crystal growth process was started after the pre-reaction process of the crystal growth process was completed in approximately 52 hours. It was thought that the In, Se, and Mn mixture would increase the vapor pressure of selenium by chemical reaction as a result of thermal conductivity. The lower and upper zone temperatures of the growth furnace were increased to 640 °C within 30 hours. It was kept at 640 °C for 15 hours. Since the exothermic chemical reaction between the elements In, Se, and Mn continues at 640–650 °C, a long period of time is needed to eliminate the risks such as ampoule explosion and cracking. Again, the alloy was heated to 1050 °C in 25 hours and kept for 12 hours. To ensure homogeneous distribution of In, Se, and Mn, the mixture was agitated by moving the growth furnace up and down at an angle of about 50° for 10 hours. The growth furnace was fixed at an angle of 65-70° to the horizontal.

The temperature in both zones of the crystal growth furnace was first kept constant at 1050 °C for 20 hours. Then the temperature was reduced to 750 °C for 80 hours. The upper zone temperature of the growth furnace was kept constant at 750 °C for 48 hours. It was reduced to 600 °C for 70 hours, 250 °C for 50 hours and 30 °C for 15 hours. The oven bottom zone temperature was reduced to 600 °C in 48 hours, 450 °C in 70 hours, 250 °C in 50 hours, 30 °C in 15 hours, and the growth process was terminated. Thus, using the same environment and the same growth temperature program, the InSe and InSe:Mn semiconductor pre-reaction processes and growth processes were completed in approximately 17 days and 19 hours, including the reaction.

At the end of the growth process, the compounds were removed from the growth furnace. In order to prevent any strain or deformation of the compound in the ampoule, it was removed from the ampoules with the help of a suitable cutter. The compounds should be kept in a very clean environment to prevent external contamination of the samples (Gürbulak, 1997; Gürbulak, 2024). This process is very important for the use of semiconductors in structural, optical, electrical, and magnetic applications.

Experimental results

In the crystal growth laboratory, the modified Bridgman-Stockbarger method was used to grow InSe and InSe:Mn solid compounds. The first basic step in obtaining high-quality binary crystals is to ensure that the basic elements in the structure are of 6N purity. Indium, selenium, manganese doped (0.03%) elements were precisely weighed on a five-digit balance to grow InSe single crystals.

Basic indium and selenium elements were obtained with a purity of about 99.999%, and the growth of InSe and InSe:Mn semiconductors was attempted. The stoichiometric ratios of the basic InSe compound were determined to be 52% indium and 48% selenium. The total mass of the chemical elements was determined to be about 50 grams. InSe crystals were grown in our crystal laboratories using a modified horizontal Bridgman-Stockbarger method. Since the sample ingots have a layered structure, they were easily separated from the layers with plastic tweezers in thicknesses of 50 – 60 mm for use in the study. Photographic views of the InSe:Mn solid crystals grown in Figure 1 are given.

As can be seen from the photographic appearance of the InSe:Mn crystals grown in Figure 1, they have a high quality and

shiny surface that is very suitable for structural analysis. The effect of Mn doping on the InSe compound is seen.

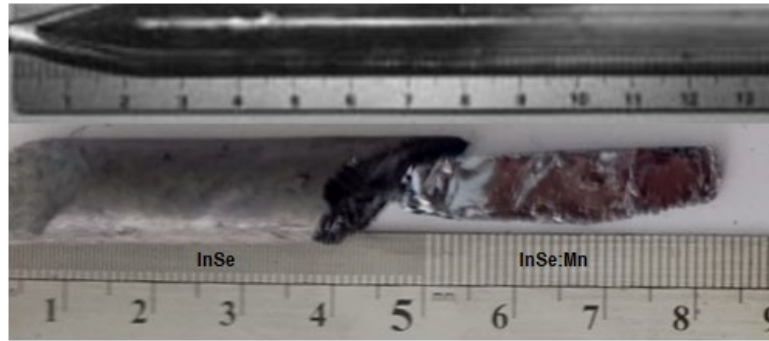


Figure 1. The photographic appearance of InSe:Mn bulk crystals

Experimental results

An important study has been conducted on the structural properties of InSe and InSe:Mn semiconductors grown with the modified Bridgman/Stockbarger technique. It belongs to the family of layered binary semiconductors known as InSe and InSe:Mn compounds. While the bonding in InSe is predominantly covalent between Se atoms and metal cations, weaker van der Waals forces also exist between adjacent layers. Covalent bonding between layers provides stability to the crystal structure, while weaker interlayer interactions allow easy separation along planes. The InSe semiconductor, characterized by anisotropic properties, was examined using X-ray diffraction with a wavelength of 0.154049 nm to determine its crystalline structure. The resulting single crystals were not subjected to any additional annealing. Samples were prepared from InSe and InSe:Mn binary semiconductors with shiny and smooth surfaces. The crystal structure of these samples has been characterized. As a result of the analysis, it was found that the InSe semiconductor has a hexagonal structure with lattice parameters $a = b = 4.025 \text{ \AA}$ and $c = 16.732 \text{ \AA}$. The crystal structure was found to be hexagonal, which coincides with the study by Viswanathan et. al. (2005). Many scientists have grown InSe single crystals using the Bridgman method and the Bridgman-Stockbarger method and carried out structural analyzes of semiconductors. It is concluded that the grown crystal has a hexagonal structure (Chevy et. al., 1977; Imai et. al., 1981; De Blasi et. al., 1982). XRD analysis of the sample phase composition showed that the hexagonal phase with reduced lattice constants $a = 4.0026 \text{ \AA}$ and $c = 16.634 \text{ \AA}$ is the main phase of InSe (P63/mmc) (Lashkarev et. al., 2007).

X-ray diffraction (XRD) is an important technique used to analyze crystal structures and crystal structural changes. It is used to determine the atomic arrangement of crystal structures. Bragg's Law is expressed by the formula $2d \sin\theta = n\lambda$. X-rays are sent to a sample of crystal. The diffraction pattern resulting from the refraction of these rays by the crystal is analyzed. Diffraction patterns usually appear as peaks. The positions of these peaks provide information about the crystal structure in the sample. The crystallization of microstructures formed at different growth stages was analysed using XRD. The XRD spectra of the InSe and InSe:Mn semiconductors are given in Figure 2. Interplane distance was obtained from d_{hkl} XRD data. The θ -2 θ scan data corresponding to (002), (004), (006), and (008) (0012) and (0014) diffraction planes of the InSe:Mn semiconductor were 11.20° , 21.92° , 32.95° , 44.08° , 68.07° , and 81.42° , respectively. Although the intensities of the XRD spectra of the InSe:Mn binary compounds increased compared to the spectra of the InSe compound, no noticeable new peaks were formed due to impurities.

As shown in Figure 2, the XRD peaks in the Mn-doped samples are sharper than those in the undoped sample. The increase in sharpness may be due to the reduction of impurities in the pure material through Mn doping. This can be expected due to the contribution of Mn atoms in InSe. It shows that n-InSe single crystals contain many impurities, which are eliminated by doping with Mn. The doping process can remove impurities between layers and is thought to neutralize existing impurities by forming complexes.

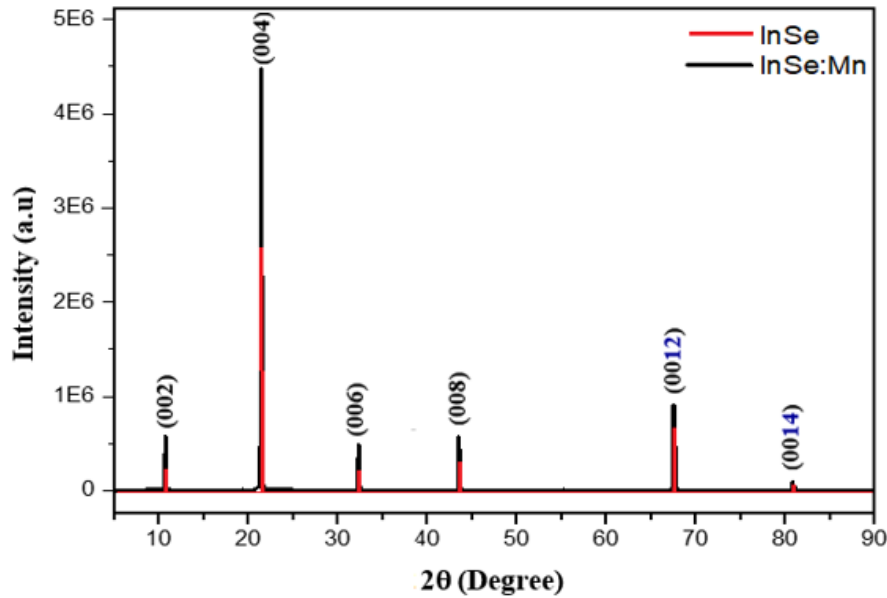


Figure 2. The effect of doping the Mn element on the InSe semiconductor on the peak intensity

If the percentage of Mn dopant ratio is appropriate, the XRD spectra of InSe single crystals increase and become sharper. For doping levels above 0.03 at. %, Mn atoms are predominantly localized between layered packings and can form localized states. In this way, charge carriers recombine intensively. This situation was observed in the study.

Some properties of the grown InSe:Mn compound were realized by interpreting the data taken and calculated with the help of XRD technique. Considering the (004) diffraction plane of the InSe:Mn semiconductor and using the given equations (Williamson, 1956; Cullity, 1972); crystal size (D_{exp}) = 895.75 (Å), dislocation density (ε) = 4.35×10^{-4} (lin⁻²m⁴), residual strain (δ) = 1.27×10^{14} (lin/m²) values were found. It was carried out with the help of high-resolution X-ray diffraction (XRD) data to detect the perfection of the as-grown single crystal.

Energy dispersive X-ray spectrometry (EDX) is an analytical device that can be integrated with an electron microscope. EDX is widely used in many research fields. By measuring the characteristic x-rays of InSe and InSe:Mn semiconductors with the help of EDX, the percentage ratios of the elements in the sample were determined. Energy dispersive x-ray spectrometry data of the Mn-doped InSe semiconductor is given in Figure 3. According to EDX results, InSe and InSe:Mn, In = 55.89%, Se = 38.86% and O = 5.25%, respectively, and InSe:Mn, In = 58.04%, Se = 37.47% and O = Contains 4.49%. The EDX spectrum of the InSe crystal was found to be close to that of the InSe:Mn crystals. The compositions of these samples were characterized by EDX. It has been determined that the Mn effect creates a more homogeneous and high-quality structure in the InSe crystal. It has been observed that the grown InSe and InSe:Mn semiconductors have high quality stoichiometric ratios and homogeneous surfaces. These values are very close to the expected values, and in addition to the formation of some In or Se bonds with O, the effect of added Mn was also observed. Results similar to those obtained from EDX analyzes have been observed in many studies.

This study presents some results of systematic studies. InSe and InSe:Mn single crystals were grown under high vacuum. Single crystals of InSe and InSe:Mn were grown under a high vacuum condition. The structural characterization of these crystals was attempted using X-ray diffraction (XRD) measurements and X energy-dispersive X-ray spectroscopy (EDX). Single crystals of InSe and InSe:Mn were grown using the modified Bridgman-Stockbarger method. The structure and melting points of these InSe and InSe:Mn binary compounds have been determined. The grown samples are shiny and layered and crystallize in hexagonal structures. Interest in the growth and characterization of such derived layered compounds has increased in recent years. Hot probe techniques revealed that both undoped and Mn doped InSe samples are n-type semiconductors. Doping with Mn can change the crystal structure and lead to a new appearance.

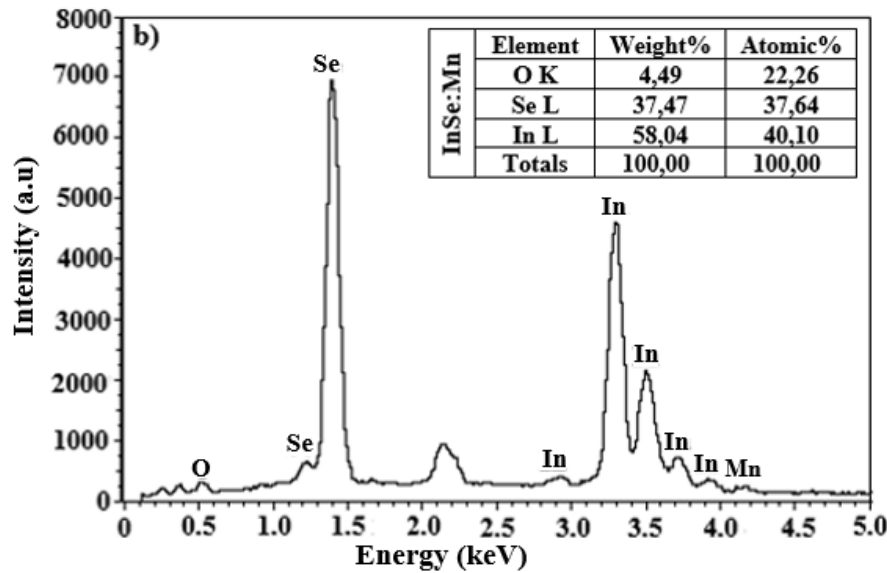


Figure 3. EDX data of InSe:Mn crystal grown at room temperature

Conclusion

An important study has been carried out on the structural properties of the grown InSe and InSe:Mn single crystals. The hexagonal structure of the InSe semiconductor with lattice parameters $a = b = 4.025 \text{ \AA}$ and $c = 16.732 \text{ \AA}$ was confirmed with the help of X-ray diffraction. Doped InSe single crystals were grown by the Bridgman method using Mn-containing In-Se alloys. Samples were taken from the ingot and annealed at 595 K for 70 hours. Mn content was determined by X-ray fluorescence analysis. It has been shown that the impurity is distributed unevenly throughout the nugget and the Mn concentration increases at the tip.

XRD investigation of the sample phase composition was conducted, and it was found that the hexagonal phase InSe (P63/mmc) with lattice constants $a = b = 4.0026 \text{ \AA}$ and $c = 16.634 \text{ \AA}$ was the main phase (Lashkarev et. al., 2007). As is known, b-InSe crystallizes in the hexagonal lattice defined as the D_{6h}^4 space symmetry group. The lattice constants are $a = b = 4.048 \text{ \AA}$, and $c = 16.930 \text{ \AA}$ (Man et. al., 1979). Eight atoms in the unit cell of b-InSe belong to two layers with the Se-In-In-Se structure. This study's results are consistent with those of numerous other studies.

InSe are layered III-VI semiconductors. Each of the structures consists of regularly stacked layers consisting of four atomic planes tightly connected according to the Se-In-Se structure. These structures exhibit strong bonding within the layers and very weak bonding between them. Due to this configuration, crystals of these compounds have high polarizability and optical uniformity, with a naturally mirror-smooth surface. The doping of the layered InSe binary compound with manganese may have led to the formation of an ordered atomic structure. Moreover, the complexation of manganese with impurities in the compound may improve the quality of the InSe semiconductor. Carrying out the procedure of a long-term growth program may have led to the arrangement of layers consisting of indium and selenium atomic planes and may have contributed to a more homogeneous formation of the layers.

When added to semiconductors, manganese alters their optical, magnetic, and electronic properties, enabling controlled optimization of these materials. Manganese-doped semiconductors exhibit magnetic and electronic properties. Ideal for use in magnetic memory and spin-based electronic devices. Manganese can alter semiconductors' band structure and carrier density, leading to phenomena such as magnetic phase transitions at low temperatures. These properties significantly affect critical parameters of the material, such as magnetic resistance, and offer great potential for advanced technology applications (Boledzyuk et al., 2014; Sang et al., 2019; Emir et al., 2024). This study and subsequent studies aim to reveal some of these properties.

Hakem Değerlendirmesi: Dış bağımsız.

Yazar Katkıları: Fikir-BG; Tasarım-; Denetleme-BG; Kaynaklar-BG; Veri Toplanması ve/veya İşlemesi BG, MKD-; Analiz ve/veya Yorum BG, MKD; Literatür Taraması-BG, MKD; Yazıyı Yazan-BG; Eleştirel İnceleme-BG.

Çıkar Çatışması: Yazarlar, çıkar çatışması olmadığını beyan etmiştir.

Finansal Destek: Bu çalışma "ID 8833, FBA-2021-8833" ve "FYL-2023-10176, Proje ID: 10176 Bridgman/Stockbarger Tekniği ile Büyütülen $X^{II}In_2Se_4$ (X^{II} : Cu, Mn, Fe, Ni, vb.) Üçlü Yarıiletkenlerin Yapısal Karakterizasyonu" Atatürk Üniversitesi BAP (Bilimsel Araştırma Projeleri) tarafından desteklenmiştir.

Peer-review: Externally peer-reviewed.

Author Contributions: Concept -BG; Design-BG; Supervision-BG; Resources- BG, MKD; Data Collection and/or Processing- BG, MKD ; Analysis and/or Interpretation- BG, MKD; Literature Search- BG, MKD; Writing Manuscript-BG; Critical Review-BG;

Conflict of Interest: The authors have no conflicts of interest to declare.

Financial Disclosure: This work "ID 8833, FBA-2021-8833" and "FYL-2023-10176, Project ID: 10176 Structural Characterization of $X^{II}In_2Se_4$ (X^{II} : Cu, Mn Fe, Ni, etc.) Ternary Semiconductors Grown by Bridgman/Stockbarger Technique," was supported by Atatürk University BAP (Scientific Research Projects)..

References

- Boledzyuk, V. B., Kovalyuk, Z. D., Kudrynskyi, Z. R., Litvin, O. S., & Shevchenko, A. D. (2014). Structure and magnetic properties of cobalt-intercalated layered InSe crystals. *Technical Physics*, 59(10), 1462–1465. <https://doi.org/10.1134/s1063784214100107>
- Camassel, J., Merle, P., Mathieu, H., & Chevy, A. (1978). Excitonic absorption edge of indium selenide. *Physical Review. B, Condensed Matter*, 17(12), 4718–4725. <https://doi.org/10.1103/physrevb.17.4718>
- Chevy, A., Kuhn, A., & Martin, M. (1977). Large InSe monocrystals grown from a non-stoichiometric melt. *Journal of Crystal Growth*, 38(1), 118–122. [https://doi.org/10.1016/0022-0248\(77\)90381-5](https://doi.org/10.1016/0022-0248(77)90381-5)
- Cullity, B.D. (1972). *Elements of X-Ray Diffraction*, Addison-Wesley, Reading, MA, p.102.
- De Blasi, C., Micocci, G., Mongelli, S., & Tepore, A. (1982). Large InSe single crystals grown from stoichiometric and non-stoichiometric melts. *Journal of Crystal Growth*, 57(3), 482–486. [https://doi.org/10.1016/0022-0248\(82\)90062-8](https://doi.org/10.1016/0022-0248(82)90062-8)
- El-Moiz, A. A., Hefni, M., Reicha, F., & Hafiz, M. (1993). Optical investigations on In_xSe_{1-x} thin films (II). *Physica B Condensed Matter*, 191(3–4), 303–311. [https://doi.org/10.1016/0921-4526\(93\)90089-o](https://doi.org/10.1016/0921-4526(93)90089-o)
- El-Sayed, S. (2003). Optical investigations of the indium selenide glasses. *Vacuum*, 72(2), 169–175. [https://doi.org/10.1016/s0042-207x\(03\)00139-8](https://doi.org/10.1016/s0042-207x(03)00139-8)
- Emir, C., Tataroglu, A., Coşkun, E., & Ocak, S. B. (2024). Structural and Optical Properties of Interfacial InSe Thin Film. *ACS Omega*. <https://doi.org/10.1021/acsomega.3c06600>
- Errandonea, D., Segura, A., Muñoz, V., & Chevy, A. (1999). Effects of pressure and temperature on the dielectric constant of GaS, GaSe, and InSe: Role of the electronic contribution. *Physical Review. B, Condensed Matter*, 60(23), 15866–15874. <https://doi.org/10.1103/physrevb.60.15866>
- Ertap, H., & Karabulut, M. (2018). Structural and electrical properties of boron doped InSe single crystals. *Materials Research Express*, 6(3), 035901. <https://doi.org/10.1088/2053-1591/aaf2f6>
- Gürbulak, B. (1997). İkili ve Üçlü Tek Kristallerin Büyütülmesi Soğurma ve Elektriksel Özelliklerinin İncelenmesi, Doktora Tezi, Atatürk Üniversitesi Fen Bil. Enst. Erzurum, 1997
- Gürbulak, B. (2004). Urbach Tail and Optical Investigations of Gd Doped and Undoped InSe Single Crystals. *Physica Scripta*, 70(2–3), 197–201. <https://doi.org/10.1088/0031-8949/70/2-3/020>
- Gürbulak, B. (2024). Theoretical Structural Characterization of XIn_2Se_4 Ternary Semiconductors Wanted to be Grow Using the Bridgman/Stockbarger Technique. *DergiPark (Atatürk University)*. <https://doi.org/10.5281/zenodo.12193900>
- Ikari, T., Shigetomi, S., Koga, Y., & Shigetomi, S. (1981). Photoluminescence of Zn Doped InSe Single Crystals. *Physica Status Solidi (B)*, 103(1). <https://doi.org/10.1002/pssb.2221030167>
- Imai, K., Suzuki, K., Haga, T., Hasegawa, Y., & Abe, Y. (1981). Phase diagram of In-Se system and crystal growth of indium monoselenide. *Journal of Crystal Growth*, 54(3), 501–506. [https://doi.org/10.1016/0022-0248\(81\)90505-4](https://doi.org/10.1016/0022-0248(81)90505-4)
- Julien, C., Benramdane, N., & Guesdon, J. P. (1990). Transformation steps of structure in flash-deposited films of a-InSe. *Semiconductor Science and Technology*, 5(8), 905–910. <https://doi.org/10.1088/0268-1242/5/8/018>
- Kaminskii, V. M. (2009). Structure and electrical properties of In_2Se_3 layered crystals. *Semiconductor Physics Quantum Electronics & Optoelectronics*, 12(3), 290–293. <https://doi.org/10.15407/spqeo12.03.290>
- Kovalyuk, Z. D., Kushnir, O. I., & Mintyanskii, I. V. (2009). Electrical properties of magnesium-intercalated InSe. *Inorganic Materials*, 45(8), 846–850. <https://doi.org/10.1134/s0020168509080032>

- Lang, O., Klein, A., Pettenkofer, C., Jaegermann, W., & Chevy, A. (1996). Band lineup of lattice mismatched InSe/GaSe quantum well structures prepared by van der Waals epitaxy: Absence of interfacial dipoles. *Journal of Applied Physics*, *80*(7), 3817–3821. <https://doi.org/10.1063/1.363335>
- Lashkarev, G., Slynko, V., Kovalyuk, Z., Sichkovskiy, V., Radchenko, M., Aleshkevych, P., Szymczak, R., Dobrowolski, W., Minikaev, R., & Zasloukin, A. (2006). Anomalies of magnetic properties of layered crystals InSe containing Mn. *Materials Science and Engineering C*, *27*(5–8), 1052–1055. <https://doi.org/10.1016/j.msec.2006.07.028>
- Man, L.I., Imamov, R.M. & Semiletov, S. A. (1979). *Kristallografia*, *21*(3), 628.
- Park, J., Afzaal, M., Helliwell, M., Malik, M. A., O'Brien, P., & Raftery, J. (2003). Chemical Vapor Deposition of Indium Selenide and Gallium Selenide Thin Films from Mixed Alkyl/Dialkylselenophosphorylamides. *Chemistry of Materials*, *15*(22), 4205–4210. <https://doi.org/10.1021/cm0310420>
- Pellicer-Porres, J., Ferrer-Roca, C., Segura, A., Jacquamet, L., & Chevy, A. (2002). Investigation of the local structure of As-related acceptor centres in InSe by means of fluorescence-detected XAS. *Semiconductor Science and Technology*, *17*(9), 1023–1027. <https://doi.org/10.1088/0268-1242/17/9/321>
- Sang, D. K., Wang, H., Qiu, M., Cao, R., Guo, Z., Zhao, J., Li, Y., Xiao, Q., Fan, D., & Zhang, H. (2019). Two Dimensional β -InSe with Layer-Dependent Properties: Band Alignment, Work Function and Optical Properties. *Nanomaterials*, *9*(1), 82. <https://doi.org/10.3390/nano9010082>
- Shih, I., Champness, C., & Shahidi, A. V. (1986). Growth by directional freezing of CuInSe₂ and diffused homojunctions in bulk material. *Solar Cells*, *16*, 27–41. [https://doi.org/10.1016/0379-6787\(86\)90073-6](https://doi.org/10.1016/0379-6787(86)90073-6)
- Slyn'ko, V. V., Khandozhko, A. G., Kovalyuk, Z. D., Slyn'ko, V. E., Zasloukin, A. V., Arciszewska, M., & Dobrowolski, W. (2005a). Ferromagnetic states in the In_{1-x}Mn_xSe layered crystal. *Physical Review B*, *71*(24). <https://doi.org/10.1103/physrevb.71.245301>
- Slyn'ko, V. V., Khandozhko, A. G., Kovalyuk, Z. D., Zasloukin, A. V., Slyn'ko, V. E., Arciszewska, M., & Dobrowolski, W. D. (2005b). Weak ferromagnetism in InSe:Mn layered crystals. *Semiconductors*, *39*(7), 772–776. <https://doi.org/10.1134/1.1992631>
- Suhre, D. R., Singh, N. B., Balakrishna, V., Fernelius, N. C., & Hopkins, F. K. (1997). Improved crystal quality and harmonic generation in GaSe doped with indium. *Optics letters*, *22*(11), 775-777. <https://doi.org/10.1364/OL.22.000775>
- Viswanathan, C., Senthilkumar, V., Sriranjini, R., Mangalaraj, D., Narayandass, S. K., & Yi, J. (2005). Effect of substrate temperature on the properties of vacuum evaporated indium selenide thin films. *Crystal Research and Technology*, *40*(7), 658–664. <https://doi.org/10.1002/crat.200410404>
- Watanabe, K., Uchida, K., & Miura, N. (2003). Magneto-optical effects observed for GaSe in megagauss magnetic fields. *Physical Review. B, Condensed Matter*, *68*(15). <https://doi.org/10.1103/physrevb.68.155312>
- Williamson, G. K., & Smallman, R. E. (1956). III. Dislocation densities in some annealed and cold-worked metals from measurements on the X-ray debye-scherrer spectrum. *Philosophical Magazine*, *1*(1), 34–46. <https://doi.org/10.1080/14786435608238074>
- Zasloukin, A. V., Kaminskii, V. M., Kovalyuk, Z. D., Mintyanskii, I. V., & Tovarnitskii, M. V. (2006). Electrical properties of hydrogenated InSe crystals. *Inorganic Materials*, *42*(12), 1308–1310. <https://doi.org/10.1134/s0020168506120053>

Synthesis, FT-IR, DFT and *in silico* Antibacterial Activity Studies of Silver Nitrate Complex of Chlorzoxazone

Mustafa Tuğfan BİLKAN

Department of Biophysics, Tokat
Gaziosmanpaşa University, Faculty of Medicine,
Tokat, Türkiye

Zehra ÇAKIL

Tokat Gaziosmanpaşa University, Faculty of
Medicine, Tokat, Türkiye

Elçin Özgür BÜYÜKATALAY

Department of Biophysics, Gazi University,
Faculty of Medicine, Ankara, Türkiye



Chlorzoxazone Molekülünün Gümüş Nitrat Bileşiğinin Sentezlenmesi, FT-IR, DFT ve *in silico* Antibakteriyel Çalışmaları

Abstract

In this study, it was aimed to produce a new potential antibacterial agent using Chlorzoxazone and silver nitrate. Within the scope of the study, CZX.AgNO₃ structure was synthesized by chemical synthesis methods. The structure was experimentally characterized by FT-IR and elemental analysis. In addition, the optimized structure and vibration frequencies were obtained by the DFT method. After characterization, ADME and toxicity parameters of the new molecule were revealed using *in silico* methods. In order to determine the antibacterial effect of the molecule, molecular docking studies were performed on gram+ Staphylococcus aureus bacteria, and the data were compared with the frequently used antibiotic clindamycin. The results revealed the ADME, toxicity, and antibacterial effect of the new compound CZX.AgNO₃ is quite superior.

Keywords: Silver Nitrate, Chlorzoxazone, Molecular Spectroscopy, DFT, Molecular Docking, *in silico* ADMET prediction

Öz

Bu çalışmada, Klorzoksazon ve gümüş nitrat kullanılarak yeni bir potansiyel antibakteriyel ajan üretilmesi amaçlanmıştır. Çalışma kapsamında, CZX.AgNO₃ yapısı kimyasal sentez yöntemleri ile sentezlenmiştir. Oluşan yapı, FT-IR ve elementel analiz metotları ile deneysel olarak karakterize edilmiştir. Ayrıca, optimize edilmiş yapı ve titreşim frekansları DFT ile elde edilmiştir. Karakterizasyon işleminin ardından, molekülün ADME ve toksisite parametreleri *in silico* yöntemler kullanılarak belirlenmiştir. Molekülün antibakteriyel etkisini belirlemek amacıyla, gram+ Staphylococcus aureus bakterisi üzerinde moleküler kenetleme çalışmaları yapılmış ve veriler, sıklıkla kullanılan antibiyotik klindamisin ile karşılaştırılmıştır. Sonuçlar, yeni bileşik CZX.AgNO₃'ün ADME, toksisite ve antibakteriyel etkisinin oldukça üstün olduğunu ortaya koymuştur.

Anahtar Kelimeler: Gümüş Nitrat, Klorzoksazon, Moleküler Spektroskopi, DFT, Moleküler Yerleştirme, *in silico* ADMET tahmini

Corresponding Author/ Sorumlu Yazar:

Mustafa Tuğfan Bilkan

E-mail: mtbilkan@gmail.com

Received/ Geliş Tarihi 10.10.2024

Accepted/Kabul Tarihi 12.11.2024

Publication Date/ 12.12.2024

Yayın Tarihi

Cite this article

Bilkan, M. T., Çakıl, Z. & Büyükatay, E.Ö. (2024) Synthesis, FT-IR, DFT and *in silico* Antibacterial Activity Studies of Silver Nitrate Complex of Chlorzoxazone. *Journal of Anatolian Physics and Astronomy*, 3(2), 52-61.



Content of this journal is licensed under a Creative Commons Attribution-Noncommercial 4.0 International License.

Introduction

Chlorzoxazone (CZX) is an effective muscle relaxant to treat muscle spasms and the resulting pain and discomfort. Its relaxant effect on skeletal muscles was discovered in the late 1950s (Stewart et al., 1987). CZX shows this effect by blocking signals to the brain and causing muscle relaxation (Bai & Ma, 2020; Megalamani et al., 2023). It also has therapeutic effects on systemic mastocytosis, conjunctivitis, and ulcerative colitis (Tang et al., 2015). When a detailed examination is made, although many studies have been conducted on CZX recently (Bai & Ma, 2020; Skrejborg et al., 2020; Deng et al., 2020; Creteanu et al., 2024), to the best of our knowledge, there has yet to be a study on the silver metal complexes of CZX. This study aimed to produce and characterize the AgNO_3 metal compound of CZX. Silver nitrate is an odorless, white solid inorganic silver salt with the chemical formula AgNO_3 . Although Albert Magnus first described it in the 13th century, it was frequently used in the treatment of cuts and wounds due to its antiseptic properties in Roman and ancient Greek civilizations. Today, with this feature, it is used in the treatment of warts and also to prevent eye diseases caused by the *Neisseria gonorrhoeae* bacteria in newborn babies (Bilkan et al., 2016). In addition to its antibacterial properties, silver nitrate injection therapy has a long history of use in urology (Sekito et al., 2022). Due to its medical and pharmacological importance, the production of new molecular structures containing silver nitrate has gained significant importance in the last ten years. In this context, in 2023, Aveledo et al. conducted studies on silver nitrate using the Calvet calorimeter (Aveledo et al., 2023). Gutmańska et al. obtained new silver compounds containing 1,4-dicyanobenzene and 3-cyanopyridine (Gutmańska et al., 2022). Pereira et al. conducted toxicity studies on silver nitrate and other silver materials (Pereira et al., 2023). Eady et al. studied Salmonella detection using SERS spectroscopy on silver nitrate nanoparticles (Eady et al., 2023). Recently, Karan and Erenler synthesized silver nanoparticles using antioxidant-effective potato varieties (Karan & Erenler, 2024). In this study, it was aimed to produce a new compound containing AgNO_3 and CZX due to their stated medical and pharmacological importance. CZX. AgNO_3 structure was produced using CZX and AgNO_3 . The structure of the compound was characterized by FT-IR and molecular modeling. Pharmacokinetic parameters and toxicity profiles of the compound were determined. In addition, in order to determine the antibacterial activity, binding conditions of *Staphylococcus aureus* bacteria with tyrosyl-tRNA synthetase (PDB ID: 1JIJ) receptor were revealed. The obtained results were compared with the results of the well-known antibiotic clindamycin, and it was found that the newly produced compound has excellent antibacterial agent potential.

Experimental and Computational Procedures

CZX and AgNO_3 were supplied by Sigma-Aldrich for the production of the compound. Since it has poor water solubility, two mmol CZX was dissolved in 5 ml ether. One mmol AgNO_3 was dissolved in 3 ml pure water. Both solutions were stirred at room temperature for 10 min and added to each other. The final mixture was stirred at 300 K for 5 min, and the precipitate formed was collected using filter paper. The collected material was dried in a sterile oven and stored at +4 °C for analysis. CHNS analyses were performed with varioMICRO CHNS analyzer. FT-IR recordings were performed with Bruker FRA 106/S Spectrometer. In the theoretical studies section, the Gaussview program was used to draw all three-dimensional compounds (Dennington et al., 2008). The drawings were optimized with Gaussian (Frisch et al., 2010), and physical, chemical, spectroscopic, and electronic properties were determined. Potential Energy Distributions for each vibration mode were obtained with the VEDA4 program (Jamróz, 2004). Protox 3.0 to predict the toxicities of the compounds (Banerjee et al., 2024) was used. The PreADMET webserver was utilized to determine the ADME parameters of the compounds (Seul, 2004). Molegro Virtual Docker program was used (Bitencourt et al., 2019) in docking analyses. In the calculations, DFT/6-311++G(d,p) was used for CZX, and LanL2DZ was used for CZX. AgNO_3 . Corrections were made by multiplying the vibration frequencies with scale factors 0.9982 for CZX and 0.9668 for silver nitrate complexes. CHN analyses results for CZX. AgNO_3 : found H(1.47%), C(32.89%), N(1.63%); calc H(1.58%), C(33.04%), N(1.58%).

Results and Discussion

Three-Dimensional Structure and Geometrical Parameters

The stable geometry of a molecular structure plays a fundamental role in determining many physical and chemical parameters of the molecule. The smallest changes in structural parameters directly affect characteristic properties, especially vibration frequencies. Therefore, the first step before working on molecular systems is to obtain a three-dimensional optimized structure. For this purpose, in this study, the three-dimensional structures of CZX and CZX.AgNO₃ molecules were optimized with DFT, and the results are shown in Figure 1.

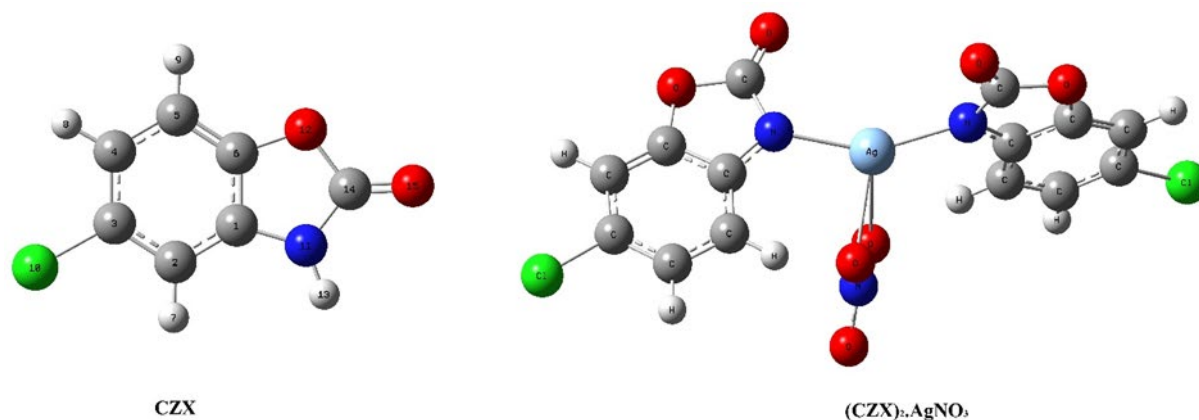


Figure 1. Optimized molecular structures of CZX and CZX.AgNO₃

As seen in Figure 1, the silver atom is bonded with two CZX molecules. As expected, chemical bonding occurred between the nitrogen atoms of the CZX molecule and the silver atom. The calculated parameters of the three-dimensional geometry and the experimental parameters of the CZX molecule are shown in Table 1 (Selected).

Table 1. Selected important geometric parameters of the structures (Å and °).

Parameters	CZX		CZX.AgNO ₃	Parameters	CZX		CZX.AgNO ₃
	Calc.	Exp.*	Calc.		Calc.	Exp.*	Calc.
1C-2C	1.385	1.393	1.421	6C-12O	1.376	1.391	1.386
1C-11N	1.390	1.387	1.372	3C-10Cl	1.758	1.738	1.799
11N-14C	1.384	1.352	1.415	5C-6C	1.377	1.380	1.385
14C-15O	1.196	1.204	1.225	12N-15Ag	-	-	2.160
14C-12O	1.392	1.378	1.465	15Ag-30O	-	2.384	2.316
1C-11N-14C	110.60	110.74	107.74	15Ag-31O	-	-	2.799
1C-6C-12O	109.61	108.44	108.92	2C-12N-15Ag	-	-	129.92
6C-12O-14C	108.27	107.83	105.78	13C-12N-15Ag	-	-	117.83
12O-14C-11N	106.34	107.54	108.49	12N-15Ag-30O	-	-	91.39
12O-14C-15O	124.23	122.04	121.94	12N-15Ag-31O	-	-	104.78
15O-14C-11N	129.43	130.55	129.57	30O-32N-31O	-	-	116.82

*Data were taken from Ref (Bilkan et al., 2016)

As seen in the table, all geometric parameters calculated with DFT are in good agreement with the experimental data taken from the literature (İde & Topaç, 1997). Especially for CZX, the parameters between the atoms in the aromatic ring were calculated with minor deviations. While the length between 1C-2C atoms was 1.393 Å experimentally, it was calculated as 1.385 Å with DFT. There is only a 0.008 Å difference between the two. Another parameter, 1C-11N bond length, was calculated as 1.390 Å, and its experimental value is 1.387 Å. The deviation is 0.003 Å. Similar results are seen for all other bond lengths. The highest deviation is between 0.02 Å and 3C-10Cl atoms, well below the acceptable limit of 0.1 Å. The N-Ag bond length is calculated as 2.16 Å. It is known from the literature that the experimental value is 2.39 Å (Bilkan et al., 2016). In this case, it has been shown that the optimized structure obtained with DFT approaches the experimental values very well. The agreement between the experimental and calculated parameters is also seen in the bond angles. There are deviations of 1-2° in the bond angles between atoms.

Vibrational Modes Analyses

Fourier Transform Infrared Spectroscopy (FT-IR) is a very useful method that allows the characterization of molecular structures by determining the vibration frequencies and intensities of a molecular structure. The method is frequently used in obtaining the structures of biologically active agents. In this study, the FT-IR spectrum for the CZX.AgNO₃ compound produced was recorded with ATR and is given in Figure 2. Experimental IR vibration modes for CZX were taken from the literature (Gnanasambandan et al., 2014).

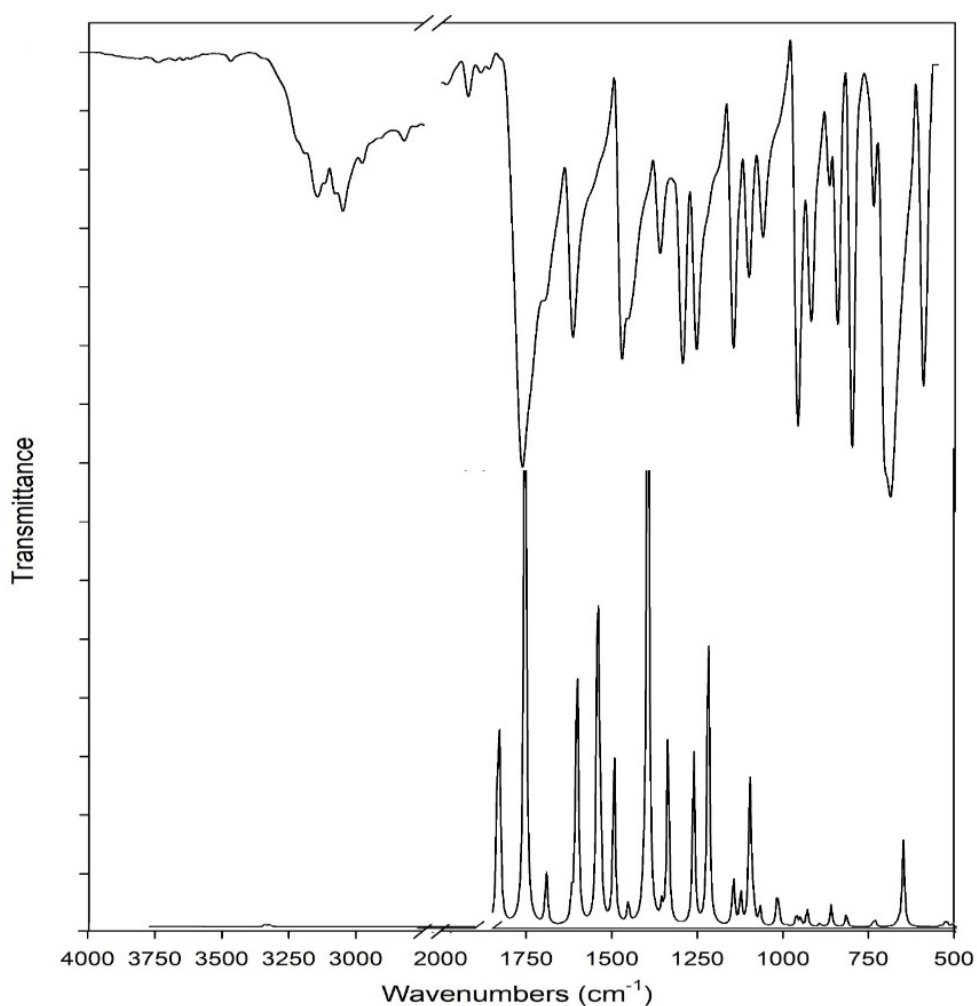


Figure 2. Calculated and recorded mid-IR spectra of CZX.AgNO₃

When Figure 2 is examined, it is seen that the recorded and calculated IR modes for the compound are in good agreement with each other. The number of vibrational modes of a compound with N atoms is given by $3N-6$. CZX has fifteen atoms and thus thirty-nine fundamental vibrational modes, while CZX.AgNO₃ has 33 atoms and 93 fundamental vibrational modes. Some important vibrational modes calculated by DFT, together with those obtained experimentally, are given in Table 2. Calculations were performed with the basis set 6-311++G(d,p) for CZX and the basis set LANL2DZ for AgNO₃. The calculated modes were scaled with the scaling factors 0.9668 and 0.9612 to obtain better agreement with the experimental ones.

Table 2. The calculated and experimental selected vibrational modes of CZX and CZX.AgNO₃

Mode	CZX			CZX.AgNO ₃			PED (%)
	Exp.	Calculated		Exp.	Calculated		
	IR*	Freq.	IR	IR	Freq.	I _{IR}	
32	592s	577	1.54	571m	530	0.97	δ_{CCC} (11)
38	-	-	-	593w	609	0.03	δ_{ONO} (76)+ V_{ON} (13)
39	-	-	-	596w	618	0.43	δ_{ONO} (85)
40	639m	591	0.18	622w	658	1.67	V_{CIC} (16)+ δ_{CCC} (14)+ V_{CC} (10)
42	-	-	-	668w	679	0.22	δ_{CNAG} (15)+ δ_{CCC} (11)+ V_{CC} (10)
46	751w	735	0.84	705m	695	0.96	Γ_{ONOC} (64)
50	-	-	-	719sh	758	2.96	δ_{OCC} (24)+ δ_{CCC} (24)+ δ_{CNAG} (10)
51	842s	837	2.37	802m	813	2.47	Γ_{HCCN} (46)+ Γ_{HCCC} (44)
54	920s	900	5.77	849w	848	14.04	δ_{CCC} (24)+ V_{OC} (22)+ δ_{CNAG} (10)
56	868w	852	0.08	867w	877	2.37	Γ_{HCCC} (78)
59	-	-	-	914m	904	2.03	V_{ON} (93)
63	959vs	920	0.06	950s	984	19.66	V_{NC} (54)
65	1061m	1054	2.38	1029w	1031	4.76	V_{CC} (35)+ δ_{HCC} (17)+ V_{CIC} (13)
66	-	-	-	1106w	1115	26.47	V_{ON} (79)+ δ_{ONO} (14)
68	1147s	1132	2.42	1149m	1136	1.18	δ_{HCC} (48)+ V_{CC} (14)
70	1102m	1080	2.14	1254w	1196	3.09	V_{OC} (38)
73	1230w	1230	0.59	1257m	1292	19.21	V_{NC} (32)+ δ_{HCC} (15)+ V_{CC} (12)
75	-	-	-	-	1337	15.10	V_{ON} (83)
76	1295s	1269	3.84	1362w	1346	48.89	V_{CC} (24)
79	1456m	1457	1.05	1453sh	1417	16.65	δ_{HCC} (39)+ δ_{CCC} (10)
81	-	1352	1.31	1482s	1432	2.37	V_{CC} (36)+ δ_{HCC} (26)
84	1616s	1621	2.97	1622m	1584	100.0	V_{CC} (51)
86	1764vs	1843	100.0	1778vs	1667	21.38	V_{OC} (81)
93	3082w	3149	0.04	3118w	3163	0.28	V_{CH} (98)

C-H stretching vibration is observed in the range of 3100-3200 cm⁻¹. C-H stretching vibrations were obtained at 3149 and 3163 cm⁻¹ wave numbers for the compounds examined in this study. Carboxyl-containing molecules generally show intense bands around 1700-1800 cm⁻¹ due to the intense observation of C-O vibrations. Since CZX contains a carboxyl group, the most intense vibration mode was calculated at 1843 cm⁻¹ and was observed experimentally at 1764 cm⁻¹. The reason for the difference is that the calculations were obtained for a single molecule in the gas phase, while the experimental results were recorded for n mol of molecules. The modes calculated at 609, 618, and 679 cm⁻¹ for CZX.AgNO₃ were not observed in CZX. These modes are due to the internal vibrations of AgNO₃ and ligand-metal bonds. These results and CHN analyses

prove that the structure produced from chemical synthesis is compatible with the theoretically modeled 2-1 bonded CZX.AgNO₃ structure.

Pharmacokinetic Properties and Toxicity Profile of CZX.AgNO₃

The absorption, distribution, metabolism and elimination (ADME) processes of a drug are called pharmacokinetic parameters and provide crucial preliminary information, especially in determining the effectiveness of pharmacological agents in the body. Biological activity can be estimated with high accuracy by examining the functional groups of compounds and comparing them with experienced drugs. In this study, ADME parameters for the CZX.AgNO₃ compound were obtained by *in silico* methods and compared with those of clindamycin, one of the essential antibiotics. The results are shown in Table 3.

Table 3. Some important *in silico* ADME parameters of clindamycin and CZX.AgNO₃

ID	clindamycin	CZX.AgNO ₃
BBB ($C_{\text{brain}}/C_{\text{blood}}$)	0.09	1.08
Caco-2 (nm/sec)	20.43	33.47
HIA (%)	84.30	100.00
MDCK (nm/sec)	0.55	0.35
Plasma Protein Binding (%)	33.65	78.77
Pure water solubility mg/L	700.3	2084.4
Skin Permeability (cm/hour)	-4.27	-3.07

BBB, one of the parameters in the table, represents the blood-brain barrier permeability. It is known as the ratio of the intracranial concentration of a drug to its concentration in plasma. A value greater than two indicates that drugs may significantly affect the central nervous system (CNS). As can be seen from the table, both compounds have a weak effect on the CNS. The Caco-2 and MDCK parameters represent the intestinal epithelial barrier and kidney cell line, respectively, and represent the number of molecules absorbed per second in nanomoles. While the Caco-2 absorption of clindamycin and CZX.AgNO₃ is at a medium level; the MDCK absorption is low. Another important ADME parameter is the HIA value. This parameter, known as Human Intestinal Absorption, gives the absorption percentage from the small intestine. Accordingly, while clindamycin is absorbed by 84.30%, CZX.AgNO₃ is absorbed by 100% from the small intestine. Plasma protein binding rate gives the binding rates of drugs to proteins known as plasma proteins, such as albumin, fibrinogen, and globulin. The higher the binding rate, the lower the drug's effectiveness. However, a binding rate below 90% is considered sufficient for the effectiveness of drugs. In this context, it can be said that the PPB rate of CZX.AgNO₃ is sufficient. In Table 4, *in silico* predicted toxicity profiles of the compounds were given.

The LD50 value (Lethal Dose 50) is the amount of toxic substance that causes the survival of a population to decrease to 50%. As the LD50 value increases, the toxicity decreases. Therefore, it is seen that CZX.AgNO₃ has lower toxicity compared to clindamycin. In addition, the toxicity class was determined as 4 for clindamycin, while it was found as 5 for CZX.AgNO₃. However, there are cases where the toxic effects of both compounds are active and inactive. For example, clindamycin has toxic effects on the immune system, while CZX.AgNO₃ has toxic effects on the liver. This is one of the important situations that should be considered in the research of the compound as a drug.

Table 4. The in silico predicted toxicity parameters of clindamycin and CZX.AgNO₃ compounds

ID	clindamycin		CZX.AgNO ₃	
Predicted LD ₅₀ (mg/kg)	1095		2161	
Predicted Toxicity Class	4	harmful if swallowed	5	May be harmful if swallowed
	Probability	Prediction	Probability	Prediction
Hepatotoxicity	0.65	Inactive	0.51	Active
Immunotoxicity	0.84	Active	0.95	Inactive
Cytotoxicity	0.73	Inactive	0.69	Inactive
Carcinogenicity	0.63	Inactive	0.56	Inactive
Mutagenicity	0.73	Inactive	0.55	Inactive
Neurotoxicity	0.81	Inactive	0.64	Active
Nephrotoxicity	0.51	Active	0.58	Active
Respiratory toxicity	0.78	Active	0.51	Active
Cardiotoxicity	0.73	Inactive	0.62	Inactive

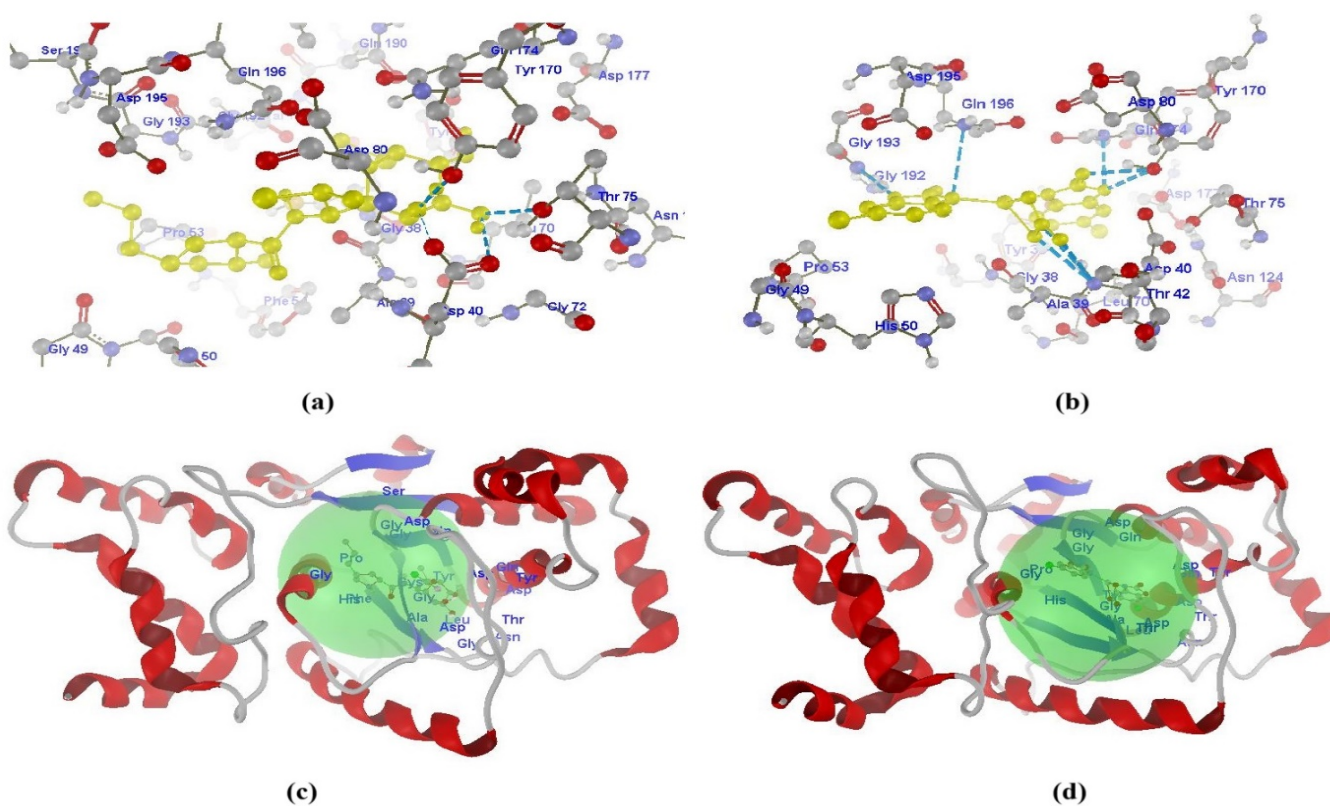
Investigation of Antibacterial Activity

Molecular docking is, in general terms, a macromolecular simulation method used to determine the interaction of a molecule with a target receptor. It is generally used to examine the therapeutic effects of a drug on a disease. After the interaction, a binding score is obtained and this score is directly proportional to the binding efficiency. This binding is mostly based on the inhibition of the protein that is the causative agent of the disease. The degenerations caused by the binding in the structure of the protein stop the proteins from performing their specialized function, and thus, the therapeutic effect occurs. In this study, the antibacterial effect was investigated by comparing the binding affinities of CZX.AgNO₃ and clindamycin (as positive control) with the tyrosyl-tRNA synthetase (PDB ID: 1JJ) receptor enzyme of *Staphylococcus aureus* bacteria. *Staphylococcus aureus* (*S. aureus*) causes some serious infections, such as endocarditis, and has significant lethal effects. The binding scores and other relevant parameters obtained as a result of docking operations are given in Table 5.

As seen in the table, CZX.AgNO₃ performed eight hydrogen bonds with the target receptor. In these bindings, the molecule acted as a hydrogen acceptor and interacted with the amino acids Gly193, Gln196, Gln174, Tyr170 (two bonds), and Asp40 (three bonds) of the protein. The MolDock score of the binding was obtained as -152.123, and a significant portion of the total binding energy originated from steric hindrance (PLP) energy. The binding score for clindamycin was obtained as -127.065. This result confirms that the CZX.AgNO₃ molecule binds to the relevant receptor better than the positive control clindamycin. The bindings for both molecular structures are given in Figure 3.

Table 5. The interaction parameters between clindamycin, CZX.AgNO₃ and the target protein

Parameters	clindamycin	CZX.AgNO ₃
MolDock Score	-127.065	-152.123
Rerank Score	-112.459	-116.705
Hydrogen Bonding energy (kcal/mol)	-3.44782	-7.256
Steric Hindrance Energy (PLP)	-141.458	-136.016
Steric Hindrance Energy (LJ12-6)	-45.523	-45.835
Electrostatic Interaction Energy Short range	-	-
Electrostatic Interaction Energy Long range	-	-
Amino acid-drug bonding (bond length: Å, bond energy: kcal/mol)	Tyr170(O)-ligand(O-H) b.l.:2.81-b.e.: -2.50 Asp40(O)-ligand(O-H) b.l.:2.46-b.e.: -0.74 Thr75(O-H)-ligand(O) b.l.:3.00-b.e.: -2.50 Asp40(O)-ligand(O-H) b.l.:3.17-b.e.: -2.16	Gly193(N-H)-ligand(O) b.l.:2.76-b.e.: -2.50 Gln196(N-H)-ligand(N) b.l.:3.49-b.e.: -0.53 Gln174(N-H)-ligand(O) b.l.:2.89-b.e.: -2.50 Tyr170(O-H)-ligand(O) b.l.:2.76-b.e.: -2.50 Tyr170(O-H)-ligand(O) b.l.:2.83-b.e.: -1.34 Asp40(O-H)-ligand(O) b.l.:3.12-b.e.: -1.92 Asp40(O-H)-ligand(O) b.l.:2.97-b.e.: -0.84 Asp40(N-H)-ligand(N) b.l.:3.46-b.e.: -0.68

**Figure 3.** The three-dimensional molecular docking structures and interaction parameters of 1JJJ protein with clindamycin and CZX.AgNO₃

Figures 3a and 3b represent the binding positions of the compounds to amino acids of the target receptor on a near scale. Figures 3c and 3d show that both compounds (clindamycin and CZX.AgNO₃) bind to the same active sites of the target protein—however, CZX.AgNO₃ has a superior binding score (-25.058 kcal/mol) than clindamycin. These results support that the potential antibacterial agent may exhibit similar binding properties to clindamycin and, thus, therapeutic effects.

Conclusion

In this study, a new potential antibacterial agent CZX.AgNO₃ was synthesized. The synthesized structure was characterized using experimental and theoretical methods. ADME and toxicity profiles of the molecule were determined *in silico*. In addition, the antibacterial activity of the molecule was carried out by molecular docking analyses. The obtained results were compared with the positive control group clindamycin and the following results were obtained:

- The geometrical structure studies show that the optimized structure obtained with DFT approaches the experimental values very well.
- CHN analyses reveal that the structure produced from chemical synthesis is compatible with the theoretically modeled 2-1 bonded CZX.AgNO₃ structure.
- ADME results show that CZX.AgNO₃ has a weak effect on the CNS. Moreover, CZX.AgNO₃ is absorbed 100% by the human intestinal system.
- *in silico* studies reveal that new compound CZX.AgNO₃ has lower toxicity compared to conventional drug clindamycin.
- Molecular docking results support the CZX.AgNO₃ may has antibacterial effect because it exhibits similar binding properties to clindamycin.

Peer-review: Externally peer-reviewed.

Author Contributions: Concept–MTB, EÖB; Design- MTB, ZÇ, EÖB; Supervision- MTB; Resources- MTB, ZÇ; Data Collection and/or Processing- MTB, ZÇ; Analysis and/or Interpretation- MTB, EÖB; Literature Search- MTB, ZÇ; Writing Manuscript- MTB, ZÇ, EÖB; Critical Review- MTB, ZÇ, EÖB Other- MTB, ZÇ, EÖB

Conflict of Interest: The authors have no conflicts of interest to declare.

Financial Disclosure: The authors declared that this study has received no financial support.

Hakem Değerlendirmesi: Dış bağımsız.

Yazar Katkıları: Fikir-MTB, EÖB; Tasarım- MTB, ZÇ, EÖB; Denetleme- MTB; Kaynaklar-MTB, ZÇ; Veri Toplanması ve/veya İşlemesi MTB, ZÇ; Analiz ve/veya Yorum- MTB EÖB; Literatür Taraması-MTB, ZÇ; Yazıyı Yazan- MTB, ZÇ, EÖB;; Eleştirel İnceleme- MTB, ZÇ, EÖB

Çıkar Çatışması: Yazarlar, çıkar çatışması olmadığını beyan etmiştir.

Finansal Destek: Yazarlar, bu çalışma için finansal destek olmadığını beyan etmiştir.

References

- Aveledo, R., Aveledo, A., Lago, N., Mato, M. M., & Legido, J. L. (2023). Antibacterial activity of silver nitrate on *Pseudomonas aeruginosa* bacteria using Calvet calorimetry. *Journal of Thermal Analysis and Calorimetry*, 148(4), 1639-1646.
- Bai, Y., & Ma, X. (2020). Chlorzoxazone exhibits neuroprotection against Alzheimer's disease by attenuating neuroinflammation and neurodegeneration *in vitro* and *in vivo*. *International Immunopharmacology*, 88, 106790.
- Banerjee, P., Kemmler, E., Dunkel, M., & Preissner, R. (2024). ProTox 3.0: a webserver for the prediction of toxicity of chemicals. *Nucleic Acids Research*, gkae303.

- Bilkan, M. T., Yurdakul, Ş., Demircioğlu, Z., & Büyükgüngör, O. (2016). Crystal structure, FT-IR, FT-Raman and DFT studies on a novel compound [C₁₀H₉N₃] 4AgNO₃. *Journal of Organometallic Chemistry*, 805, 108-116.
- Bitencourt-Ferreira, G., & de Azevedo, W. F. (2019). Molegro virtual docker for docking. *Docking screens for drug discovery*, 149-167.
- Creteanu, A., Lisa, G., Vasile, C., Popescu, M. C., Pamfil, D., Lungu, C. N., ... & Tantar, G. (2024). New Hydrophilic Matrix Tablets for the Controlled Released of Chlorzoxazone. *International Journal of Molecular Sciences*, 25(10), 5137.
- Deng, L., Li, H., Su, X., Zhang, Y., Xu, H., Fan, L., ... & Zhao, R. C. (2020). Chlorzoxazone, a small molecule drug, augments immunosuppressive capacity of mesenchymal stem cells via modulation of FOXO3 phosphorylation. *Cell Death & Disease*, 11(3), 158.
- Dennington, R. D., Keith, T. A., & Millam, J. M. (2008). GaussView 5.0, Gaussian, Inc., Wallingford, 20.
- Eady, M., Setia, G., Park, B., Wang, B., & Sundaram, J. (2023). Biopolymer encapsulated silver nitrate nanoparticle substrates with surface-enhanced Raman spectroscopy (SERS) for Salmonella detection from chicken rinse. *International Journal of Food Microbiology*, 391, 110158.
- Frisch, M. J., Trucks, G. W., Schlegel, H. B., Scuseria, G. E., Robb, M. A., Cheeseman, J. R., ... & Cioslowski, J. (2010). Gaussian 09 Revision B. 01 M., and Revision A. 02 SMP J. Gaussian, Inc., Wallingford, CT.
- Gnanasambandan, T., Gunasekaran, S., & Seshadri, S. (2014). FT-IR, FT-Raman, UV-Vis spectral and normal coordinate analysis of chlorzoxazone. *Journal of Molecular Structure*, 1061, 124-133.
- Gutmańska, K., Ciborska, A., Hnatejko, Z., & Dołęga, A. (2022). Nitrate and nitrite silver complexes with weakly coordinating nitriles. *Polyhedron*, 220, 115831.
- İde, S., & Topaç, A. (1997). Tautomeric investigations and crystal structure analysis of chlorzoxazone. *Journal of chemical crystallography*, 27, 303-306.
- Jamróz, M. H., (2004). Vibrational Energy Distribution Analysis. VEDA 4, Warsaw.
- Karan, Y. B., & Erenler, R. (2024). Synthesis of Silver Nanoparticles Using Potato Cultivars with Their Antioxidant Activity. *Communications in Soil Science and Plant Analysis*, 1-9.
- Megalamani, M. B., Patil, Y. N., & Nandibewoor, S. T. (2023). YSZ/MoS₂ modified carbon based sensor for the determination of muscle relaxant agent chlorzoxazone: A novel electroanalytical strategy. *Inorganic Chemistry Communications*, 155, 111074.
- Pereira, S. P., Boyle, D., Nogueira, A. J., & Handy, R. D. (2023). Comparison of toxicity of silver nanomaterials and silver nitrate on developing zebrafish embryos: Bioavailability, osmoregulatory and oxidative stress. *Chemosphere*, 139236.
- Sekito, T., Sadahira, T., Watanabe, T., Maruyama, Y., Watanabe, T., Iwata, T., ... & Watanabe, M. (2022). Medical uses for silver nitrate in the urinary tract. *World Academy of Sciences Journal*, 4(1), 1-6.
- Seul, S. C. (2004) Bioinformatics and Molecular Design Research Center;. PreADMET program.
- Stewart, J. T., & Janicki, C. A. (1987). Chlorzoxazone. In Analytical profiles of drug substances (Vol. 16, pp. 119-144). Academic Press.
- Skrejborg, P., Petersen, K. K., Beck, J., Ulrich, M., Simonsen, O., Nielsen, P. T., ... & Laursen, M. (2020). Investigating the effect of perioperative chlorzoxazone on acute postoperative pain after total hip and knee replacement surgery. *The Clinical Journal of Pain*, 36(5), 352-358.
- Tang, P., Li, S., Wang, L., Yang, H., Yan, J., & Li, H. (2015). Inclusion complexes of chlorzoxazone with β - and hydroxypropyl- β -cyclodextrin: characterization, dissolution, and cytotoxicity. *Carbohydrate polymers*, 131, 297-305.

Investigation of Photo-Electrical Properties in (Fe₂O₃-G)/n-Si Device

(Fe₂O₃-G)/n-Si Cihazında Foto-Elektriksel Özelliklerin İncelenmesi

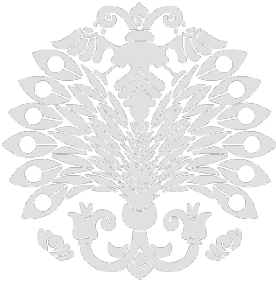
Elif DAŞ^{1,2}

¹Department of Physics, Science Faculty, Atatürk University, Erzurum, Türkiye

²Department of Nanoscience and Nanoengineering, Graduate School of Natural and Applied Science, Atatürk University, Erzurum, Türkiye

Gamze BOZKURT

Technology Transfer Implementation and Research Center, Erzurum Technical University, Erzurum, 25050, Türkiye



Corresponding Author/ Sorumlu Yazar:

G. BOZKURT

E-mail: gamze.bozkurt@erzurum.edu.tr

Received/ Geliş Tarihi 05.08.2024

Accepted/Kabul Tarihi 31.10.2024

Publication Date/ 12.12.2024

Yayın Tarihi

Cite this article

Daş, E. & Bozkurt G. (2024) *Investigation of Photo-Electrical Properties in (Fe₂O₃-G)/n-Si Device*. *Journal of Anatolian Physics and Astronomy*, 3(2), 62-74.



Content of this journal is licensed under a Creative Commons Attribution-Noncommercial 4.0 International License.

Abstract

This study focuses on synthesizing iron oxide-graphene (α -Fe₂O₃-G) composite materials and evaluating their performance in devices constructed on n-type silicon (n-Si) semiconductors under dark and illuminated conditions. Key electrical parameters such as the ideality factor ($n = 2.59$), barrier height ($\Phi_b = 0.74$ eV), and series resistance ($R_s = 70$ k Ω) were determined using Thermionic Emission (TE) and Norde methods from I-V measurements taken in the dark. The device's photoelectrical properties were further examined under illumination, revealing that the Fe₂O₃-G/n-Si device exhibits self-powered behavior, operating without an external power source. The device achieved a maximum ON/OFF ratio of 32496, a specific detectivity (D^*) of 26.6 Jones at 0 V, and a maximum responsivity (R) of 98 mAW⁻¹ at -2 V. These results highlight the device's potential for efficient photodetection, particularly in self-powered applications.

Keywords: I-V characteristic, Norde method, Photosensitive device, Micro-emulsion method

Öz

Bu çalışma, demir oksit-grafen (α -Fe₂O₃-G) kompozit malzemelerin sentezlenmesine ve bunların n-tipi silisyum (n-Si) yarıiletkeni ile oluşturulan cihazlardaki performanslarının hem karanlık hem de aydınlık koşullardaki değerlendirilmesine odaklanmaktadır. İdealite faktörü ($n = 2,59$), bariyer yüksekliği ($\Phi_b = 0,74$ eV) ve seri direnç ($R_s = 70$ k Ω) gibi elektriksel parametreler karanlıkta alınan I-V ölçümlerinden Termiyonik Emisyon (TE) ve Norde yöntemleri kullanılarak belirlenmiştir. Cihazın fotoelektrik özellikleri aydınlatma altında da incelenmiş ve Fe₂O₃-G/n-Si cihazının harici bir güç kaynağı olmadan çalışarak kendi kendine güç sağlama davranışı sergilediği ortaya çıkmıştır. Aygıt, 0 V'ta maksimum ON/OFF oranına (32496), spesifik dedektiviteye (D^* , 26,6 Jones) ve -2 V'ta da maksimum duyarlılığa (R , 98 mAW⁻¹) ulaşmıştır. Bu sonuçlar, cihazın özellikle kendi kendine güç sağlayan uygulamalarda verimli ışık algılama potansiyeline sahip olduğunu vurgulamaktadır.

Anahtar Kelimeler: I-V karakteristiği, Norde metodu, Işığa duyarlı cihaz, Mikro-emülsiyon yöntemi

Introduction

Photodetectors are essential optical devices that transform light into electrical signals (Ramakrishnan et al., 2023; Talebi & Eshghi, 2023). Self-powered photodetectors, which do not require an external power source, have become highly significant in the field of optoelectronics (Kim et al., 2024). Their appeal lies in their high performance, low production costs, and stability. The selection of suitable materials and fabrication techniques is crucial to achieving these benefits (Sarkar & Kumar, 2024).

Metal oxide nanoparticles (MO NPs), particularly iron oxide, play a vital role in optoelectronic technology (Saleem et al., 2023). Iron oxide exists in several forms, including hematite (α -Fe₂O₃), maghemite (γ -Fe₂O₃), and magnetite (Fe₃O₄) (Can et al., 2012). Among them, hematite is known for its stability and suitable band gap for visible light absorption, making it an excellent candidate for photodetector applications (Ghobadi et al., 2019). The inclusion of α -Fe₂O₃ in photodetectors enhances their photoresponse and stability due to its excellent chemical stability, high absorption coefficient, and environmentally friendly nature (Wang et al., 2023).

The synthesis of α -Fe₂O₃ NPs can be achieved through various methods, with the microemulsion method being particularly effective (Han et al., 2011; Muhajir et al., 2019). This method involves creating a microemulsion—a mixture of water, oil, and surfactant—to produce NPs with controlled size and morphology (Li & Park, 1998). The microemulsion technique offers advantages such as simplicity, low cost, and the ability to produce uniform NPs, which are essential for consistent optoelectronic device performance.

Incorporating graphene into composites with MO NPs, such as α -Fe₂O₃, brings additional benefits (Sun et al., 2015; Lu et al., 2019). Graphene, a single layer of carbon atoms arranged in a hexagonal lattice, is known for its exceptional electrical conductivity, mechanical strength, and high surface area (Yurtcan & Daş, 2018; Daş & Yurtcan, 2022). When combined with α -Fe₂O₃ NPs, graphene enhances the charge transport properties, increases the surface area for light absorption, and improves the overall stability of the composite (Alan et al., 2018; Idisi et al., 2023). These enhancements lead to higher sensitivity, faster response times, and greater efficiency in photodetectors.

In this study, we synthesized α -Fe₂O₃-graphene (Fe₂O₃-G) composite materials and fabricated them into thin films on n-type silicon wafers to investigate their impact on device performance. The primary electrical parameters were determined using the Thermionic Emission (TE) theory and the Norde method, which provided insights into the barrier height, ideality factor, and series resistance of the devices. Furthermore, we evaluated the optoelectronic performance of the Fe₂O₃-G composite-based devices by measuring key characteristics such as the ON/OFF ratio, responsivity (R), and specific detectivity (D*) under white light illumination. By systematically analyzing the electrical and optoelectronic parameters, this study provides a detailed understanding of the potential advantages and limitations of Fe₂O₃-G composites in photodetector applications.

Experimental Procedure

Materials

Iron (III) chloride (FeCl₃), sourced from the Merck Company, was used as the precursor in this study. The surfactant dioctyl sulfosuccinate sodium salt (AOT), along with 1-butanol, n-heptane, and sodium hydroxide (NaOH), were acquired from Sigma-Aldrich Company in analytical grade. Graphene was supplied by the Nanografi Company (Türkiye). Additionally, during the device fabrication process, an n-type silicon substrate with a resistivity between 1 and 10 Ω cm, a thickness of about 280 μ m, and a (100) orientation was used. The surface of the silicon substrate underwent a thorough cleaning procedure.

Material Synthesis

α -Fe₂O₃ material was produced using the microemulsion technique, as documented in prior research (Bozkurt, 2020). This technique was chosen for its effectiveness in generating NPs with uniform size and morphology, which are essential for achieving consistent performance in device applications. Following the synthesis of α -Fe₂O₃ NPs, a mixture of graphene and α -Fe₂O₃ NPs was prepared in a mortar to form the Fe₂O₃-G composite. This was achieved using a 1:0.5 weight ratio,

thoroughly grinding the components in the mortar until a homogeneous mixture was obtained.

Device Fabrication

Initially, the n-type Si substrate was cleaned using the established “Radio Corporation of America (RCA) chemical cleaning processes” (Güllü et al., 2008). Subsequently, a layer of pure aluminum (approximately 120 nm thick) was evaporated onto the unpolished surface of the n-Si wafer at a pressure of 2×10^{-6} Torr. The wafer was then annealed at 450 °C for 10 minutes in a nitrogen atmosphere to prevent oxidation on the polished surface. In the next step, the Fe₂O₃-G composite was dissolved in a water/ethanol mixture and applied to the polished surface of the n-Si wafer using the spin coating technique at 1500 rpm, forming a film layer. The coated wafer was left to dry at room temperature overnight. For electrical measurements, gold (Au) dot contacts (with an area of 7.85×10^{-3} cm²) were evaporated onto the Fe₂O₃-G film using the same system employed for the Al back contact. The device design is illustrated in Figure 1. The electrical and photoelectrical properties of the Fe₂O₃-G/n-Si device were examined by using a Keithley sourcemeter at room temperature under both ambient conditions and 1 sunlight intensity.

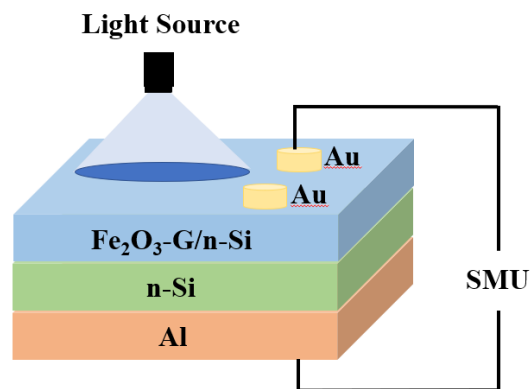


Figure 1. Schematic illustration of the prepared device architecture

Additionally, an Au/n-Si/Al device without Fe₂O₃-G NPs was also fabricated for comparison. This allowed for a detailed assessment of how integrating Fe₂O₃-G affected the device's electrical properties.

Results and Discussion

Some Physical Properties of the Fe₂O₃-G Material

The crystal structure of the Fe₂O₃-G composite was examined through X-ray diffraction (XRD) using a Rigaku Miniflex diffractometer equipped with a Cu K α radiation source ($\lambda = 1.5406$ Å). The XRD pattern displayed distinct peaks corresponding to α -Fe₂O₃, confirming the presence of hematite (α -Fe₂O₃) NPs within the composite material (Bozkurt, 2020), as shown in Figure 2. However, the absence of diffraction peaks for the crystalline phase of graphene could be attributed to the limited amount of graphene mixed with the α -Fe₂O₃ NPs. This lack of peaks may also result from a significant number of α -Fe₂O₃ NPs overlapping on the surface of the graphene (Gao et al., 2022), obscuring the detection of its characteristic peaks in the XRD analysis.

To examine the surface morphology and elemental composition of the Fe₂O₃-G/n-Si structure, SEM and EDS analyses were conducted, as shown in Figure 3. The SEM image reveals a granular texture with irregularly shaped particles, indicating a distinct morphology compared to the previously reported plain Fe₂O₃ structure (Bozkurt, 2020). The incorporation of graphene likely contributes to this altered morphology, promoting the formation of a more interconnected and porous network.

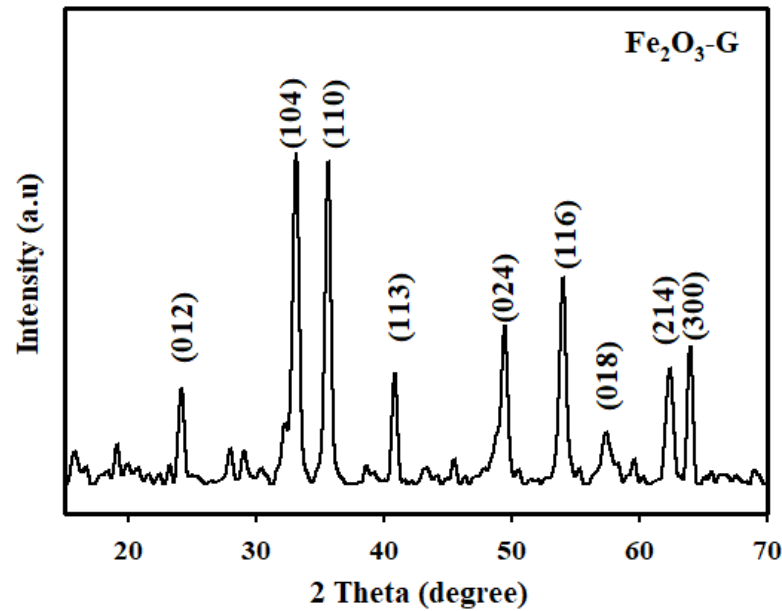


Figure 2. XRD pattern of $\text{Fe}_2\text{O}_3\text{-G}$ material

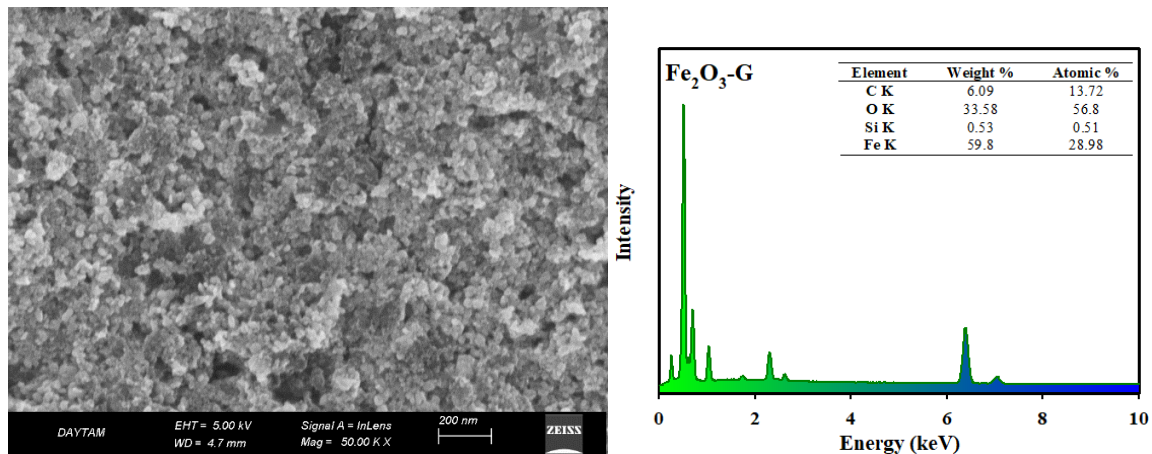


Figure 3. SEM image and the EDS spectrum of $\text{Fe}_2\text{O}_3\text{-G/n-Si}$ structure

Additionally, the EDS analysis confirmed the presence of Fe, C, O, and Si elements in the structure. The slight detection of Si is attributed to the underlying silicon substrate, while the pronounced C peaks confirm the successful incorporation of graphene. The Fe and O peaks correspond to the Fe_2O_3 component, further validating the composition of the composite structure. The EDS results highlight the effective integration of graphene into the Fe_2O_3 matrix, contributing to the material's unique properties.

A UV-Vis absorption analysis was performed to evaluate the optical properties of the $\text{Fe}_2\text{O}_3\text{-G}$ composite. The absorbance spectrum exhibited a wide range of absorption from approximately 300 to 800 nm, indicating strong light absorption across the visible spectrum, which is characteristic of Fe_2O_3 -based materials. To determine the band gap, the Tauc plot was employed, and the band gap energy was calculated to be around 2 eV. This value is consistent with the band gaps typically reported in the literature for $\text{Fe}_2\text{O}_3\text{-G}$ composites, which generally fall between 1.9 and 2.2 eV (Abdel-Salam et al., 2022; Idisi et al., 2023), confirming the effectiveness of the composite for optoelectronic and photocatalytic applications. The result aligns well with the expected electronic properties, indicating successful synthesis and integration of the materials.

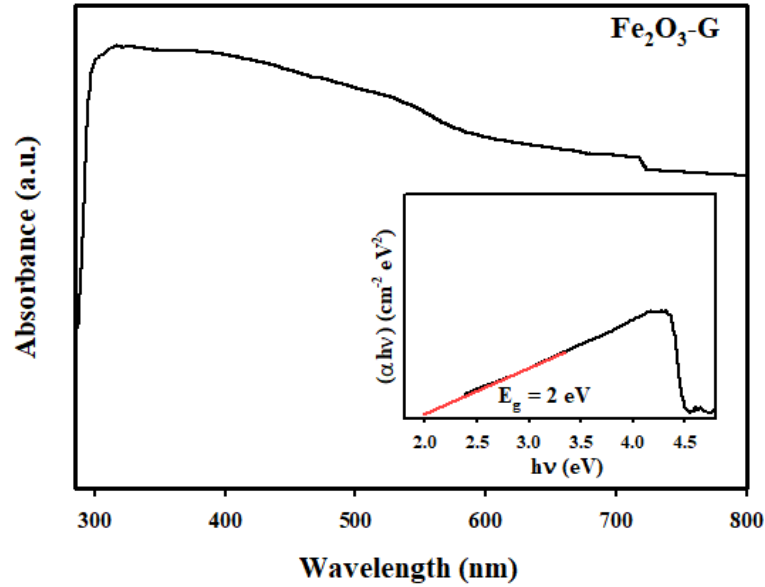


Figure 4. UV-Vis spectra of $\text{Fe}_2\text{O}_3\text{-G}$ composite: Inset shows the Tauc plot of the material

Electro-Optical Properties of the $\text{Fe}_2\text{O}_3\text{-G/n-Si}$ Device Structure

In this study, the devices' current-voltage (I-V) responses were evaluated under two distinct conditions: first, in a dark environment to establish baseline characteristics, and second, under an illumination condition (a visible light source with an intensity of 100 mW/cm^2 , equivalent to 1 sun intensity).

Figure 5 shows the I-V curves of the reference (Au/n-Si/Al) and $\text{Fe}_2\text{O}_3\text{-G/n-Si}$ devices in a dark environment. Both devices exhibit excellent rectifying characteristics with an exponential increase in the forward bias region. The fundamental principles of thermionic emission (TE) theory can be utilized to evaluate the electrical parameters of this kind of diode (Orhan et al., 2020; Daş et al., 2021). According to the thermionic emission (TE) theory, the relationship between current (I) and voltage (V) is described as follows (Gupta et al., 2009):

$$I = I_0 \left[\exp\left(\frac{qV}{nKT}\right) - 1 \right] \quad (1)$$

with

$$I_0 = AA^*T^2 \exp(-q\Phi_b/kT) \quad (2)$$

where I_0 represents the reverse bias saturation current, q is the electronic charge, V is the applied voltage, n is the ideality factor of the diode, k is the Boltzmann constant, T is the temperature in Kelvin, A is the diode area ($7.85 \times 10^{-3} \text{ cm}^2$), and A^* is the Richardson constant ($112 \text{ A/cm}^2\text{K}^2$ for n-Si), and Φ_b is the barrier height (Aydoğan et al., 2010).

By rearranging the above equations, the Φ_b and the n can be calculated using the following formulas:

$$\Phi_b = \frac{kT}{q} \ln\left(\frac{AA^*T^2}{I_0}\right) \quad (3)$$

$$n = \frac{q}{kT} \left(\frac{dV}{d \ln I} \right) \quad (4)$$

The ideality factors (n) for the fabricated diodes were found to be 2.03 for the reference device and 2.59 for the $\text{Fe}_2\text{O}_3\text{-G/n-Si}$ device. These values, being greater than one, suggest that both diodes exhibit non-ideal behavior. This non-ideal behavior can be attributed to several factors, including significant surface leakage currents, a high density of recombination

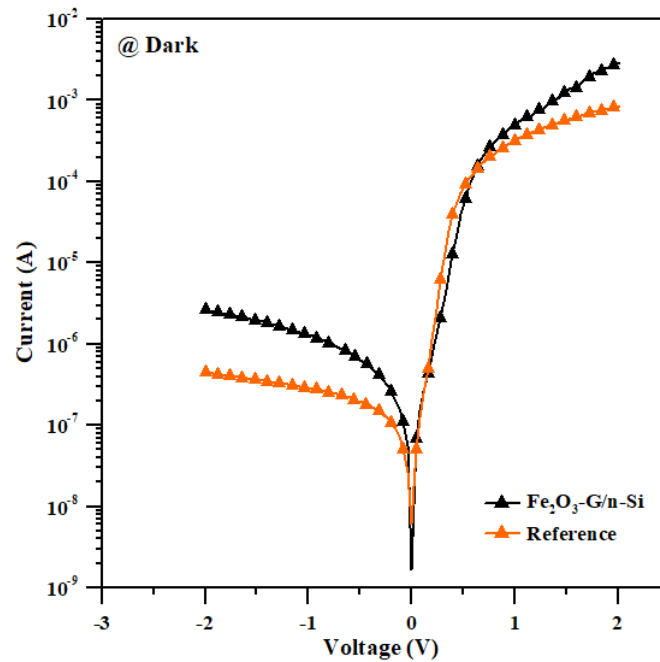


Figure 5. I-V characteristics of the reference and the Fe₂O₃-G/n-Si devices

centers within the depletion region, a high density of interface states, and increased series resistance (Middya et al., 2014; Yıldırım & Daş, 2023). These factors collectively contribute to deviations from the ideal diode behavior, affecting the overall performance of the devices. Additionally, the barrier heights for both devices were determined to be 0.74 eV. The obtained results were tabulated in Table 1.

Table 1. Main electrical parameters of the reference and Fe₂O₃-G/n-Si devices at dark ambient

Reference device					Fe ₂ O ₃ -G/n-Si				
TE method			Norde		TE method			Norde	
I_0 ($\times 10^{-8}$ A)	n	Φ_b (eV)	Φ_b (eV)	R_s (k Ω)	I_0 ($\times 10^{-8}$ A)	n	Φ_b (eV)	Φ_b (eV)	R_s (k Ω)
2.49	2.03	0.74	0.74	490	3.27	2.59	0.74	0.74	70

The elevated ideality factor and the downward concavity observed in the forward bias I-V characteristics at high applied voltages suggest that series resistance (R_s) significantly impacts the device's performance. To address this, Norde developed a method for estimating both the R_s and the Φ_b of diodes (Norde, 1979). Norde's approach involves using a specific function, which can be expressed as follows (Norde, 1979):

$$F(V) = \frac{V}{\gamma} - \frac{kT}{q} \ln \left(\frac{I(V)}{AA^*T^2} \right) \quad (5)$$

where γ is an integer greater than the n from the TE theory and the Φ_b can be derived from the Norde function using the following formula (Norde, 1979):

$$\Phi_b = F(V_{min}) + \frac{V_{min}}{\gamma} - \frac{kT}{q} \quad (6)$$

where V_{min} refers to the minimum forward biased value in Norde's function, $F(V)$. Additionally, the R_s value can be determined from Norde's functions as follows (Norde, 1979):

$$R_s = \frac{kT(\gamma - n)}{qI} \quad (7)$$

where I is the current value that corresponds to the minimum value of Norde's function. Figure 6 presents the variation

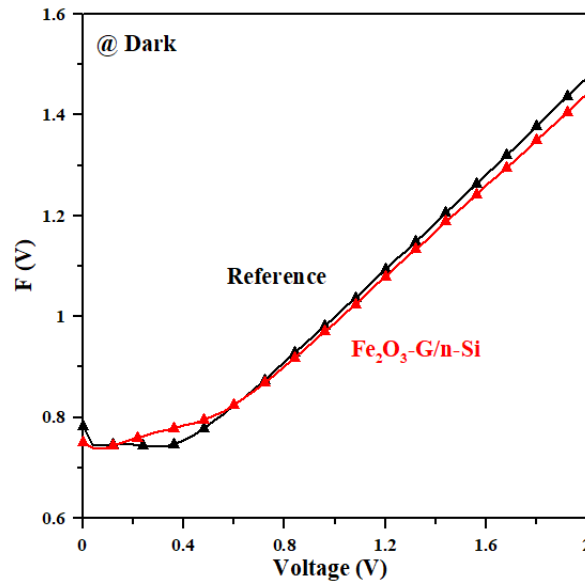


Figure 6. $F(V)$ versus V plots for the reference and the $\text{Fe}_2\text{O}_3\text{-G/n-Si}$ devices

of Norde's function with the applied voltage for the manufactured devices. Additionally, Table 1 provides the calculated values for the R_s and Φ_b . The results indicate that the Φ_b values derived from both traditional I-V analysis and the Norde approximation are identical. On the other hand, the R_s value of the $\text{Fe}_2\text{O}_3\text{-G/n-Si}$ device is found to be lower than that of the reference device. This can be attributed to several factors. Firstly, the incorporation of Fe_2O_3 and graphene likely enhances the electrical conductivity and charge carrier mobility within the device. Graphene, known for its excellent electrical properties, provides a conductive pathway that reduces resistance. Additionally, the Fe_2O_3 NPs may facilitate better contact at the interfaces, improving the overall efficiency of charge transfer. This synergistic effect between Fe_2O_3 and graphene likely contributes to the reduced R_s , thereby enhancing the device's performance.

Furthermore, the I-V characteristics of the $\text{Fe}_2\text{O}_3\text{-G/n-Si}$ device were analyzed under illumination to investigate their photoelectrical properties, as illustrated in Figure 7. The figure demonstrates that illumination significantly increased the dark current in the negative bias region while having minimal impact on the current in the positive bias region. In photodiodes and photodetectors, this type of I-V characteristic is commonly observed. This behavior therefore suggests that the fabricated device has the potential to be used as an effective photodetector. The high current observed under reverse bias is due to the formation of photogenerated electron-hole pairs and their separation by the internal electric field in the depletion region, which enhances carrier drift and thus increases the photocurrent. Additionally, it is evident that the $\text{Fe}_2\text{O}_3\text{-G/n-Si}$ device demonstrates self-powered behavior, meaning it operates without the need for an external power source.

The ON/OFF ratio of a heterojunction photodetector indicates the device's responsiveness to incident light (Yıldırım & Daş, 2023). It is a crucial parameter that reflects the difference between the photocurrent generated when the device is illuminated (ON state) and the dark current when no light is present (OFF state). A high ON/OFF ratio is desirable as it signifies strong light sensitivity and effective suppression of dark current, leading to better detection accuracy. This ratio also provides insights into the signal-to-noise ratio of the device, which is vital for applications requiring precise light detection. Figure 8 and Table 2 show the variation of the ON/OFF ratio of the $\text{Fe}_2\text{O}_3\text{-G/n-Si}$ device as a function of applied voltage. As light intensity increases, the ON/OFF ratio of the device improves, reflecting enhanced sensitivity to light. Conversely, the ratio decreases with increasing applied voltage. Specifically, the highest ON/OFF ratio is achieved at 0 V, indicating optimal performance at this voltage. In contrast, the ratio diminishes at -2 V, suggesting that higher reverse bias reduces the device's effectiveness in distinguishing between light and dark states. This behavior underscores the importance of optimizing the applied voltage to balance the device's sensitivity and performance.

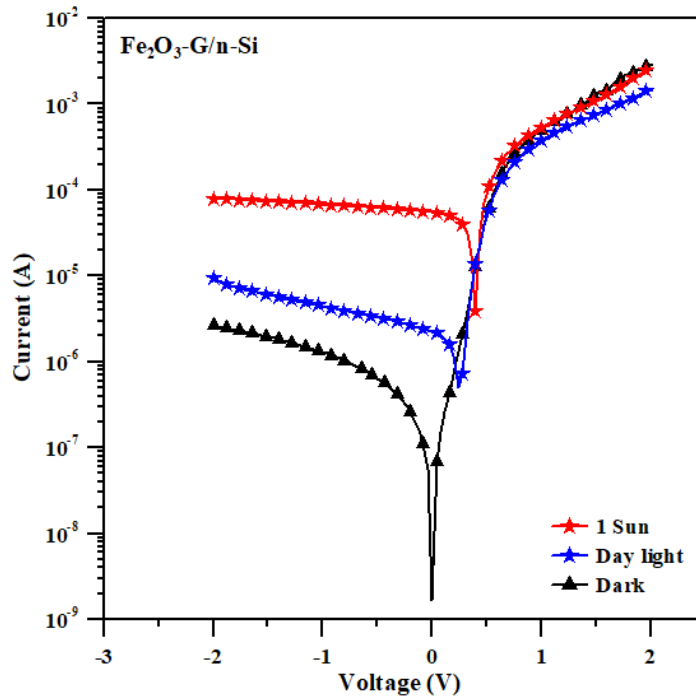


Figure 7. I-V characteristics of the $\text{Fe}_2\text{O}_3\text{-G/n-Si}$ device under illumination

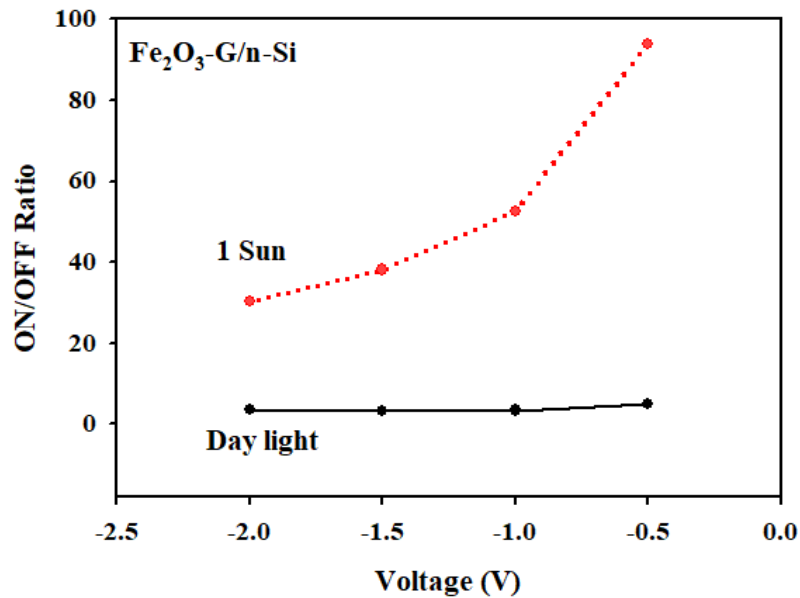


Figure 8. Variation of the ON/OFF ratio of the $\text{Fe}_2\text{O}_3\text{-G/n-Si}$ device as a function of applied voltage

Table 2. ON/OFF ratios of the $\text{Fe}_2\text{O}_3\text{-G/n-Si}$ device for different applied voltages

Device	Ambient	ON/OFF Ratio				
		0V	- 0.5V	-1V	-1.5 V	-2V
$\text{Fe}_2\text{O}_3\text{-G/n-Si}$	Day light	1334	4.9	3.4	3.1	3.6
	1 Sun	32496	93.7	52.6	38.1	30.3

The efficiency of a photodetector in responding to incident light is characterized by its responsivity (R). Responsivity

quantifies the photodetector's capability to convert light into electrical signals under specific bias and illumination conditions. It is defined as follows (Erdoğan et al., 2022; Daş, 2022):

$$R(A/W) = \frac{J_{ph}}{P_{in}} \quad (8)$$

where J_{ph} is the current density generated by the device and P_{in} is the total power of the light incident on the device. Figure 9 and Table 3 illustrate how the responsivity of the $\text{Fe}_2\text{O}_3\text{-G/n-Si}$ device changes with varying applied voltage. The results indicate that the responsivity of the $\text{Fe}_2\text{O}_3\text{-G/n-Si}$ device improves as the reverse bias voltage increases. Specifically, the responsivity is lowest at 0 V, where the device shows minimal sensitivity to light. In contrast, the responsivity reaches its highest value at -2 V, suggesting that the device becomes more efficient in converting incident light into electrical signals under higher reverse bias conditions. This behavior highlights the device's enhanced performance with increased reverse bias, which likely improves the separation and collection of photogenerated carriers, thereby increasing the overall responsivity.

Specific detectivity (D^*) is another crucial performance metric for photodiodes. It quantifies the ability of a photodiode to detect weak optical signals while minimizing noise. It is defined by the following equation (Xiong et al., 2024; Alsharefi & Al-Nafiey, 2024):

$$D^* = \frac{RA^{1/2}}{\sqrt{2qI_d}} \quad (9)$$

here, q represents the electronic charge, and A denotes the active junction area of the diode. The unit of D^* is $\text{cmHz}^{1/2}\text{W}^{-1}$, commonly referred to as Jones. The calculated D^* values for the fabricated device are presented in Table 4 and illustrated in Figure 10.

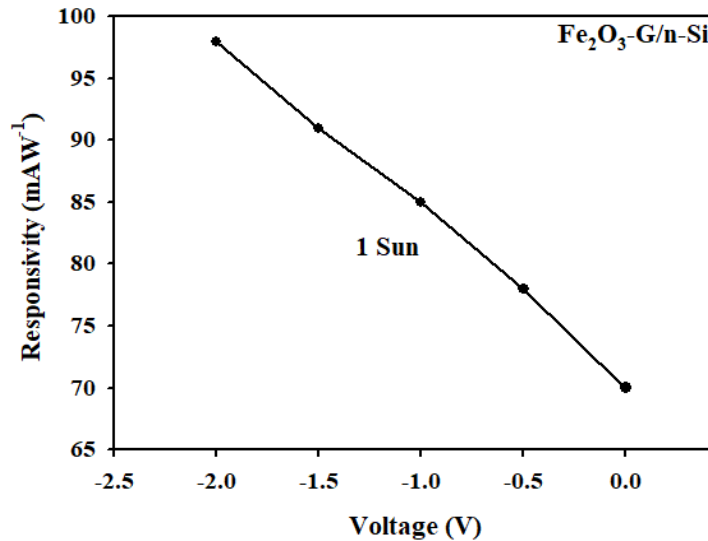


Figure 9. Variation of the responsivity of the $\text{Fe}_2\text{O}_3\text{-G/n-Si}$ device as a function of applied voltage

Table 3. Variation in responsivity of the $\text{Fe}_2\text{O}_3\text{-G/n-Si}$ device with different applied voltages

Device	Ambient	Responsivity (R) (mAW ⁻¹)				
		0V	- 0.5V	-1V	-1.5 V	-2V
$\text{Fe}_2\text{O}_3\text{-G/n-Si}$	1 Sun	70	78	85	91	98

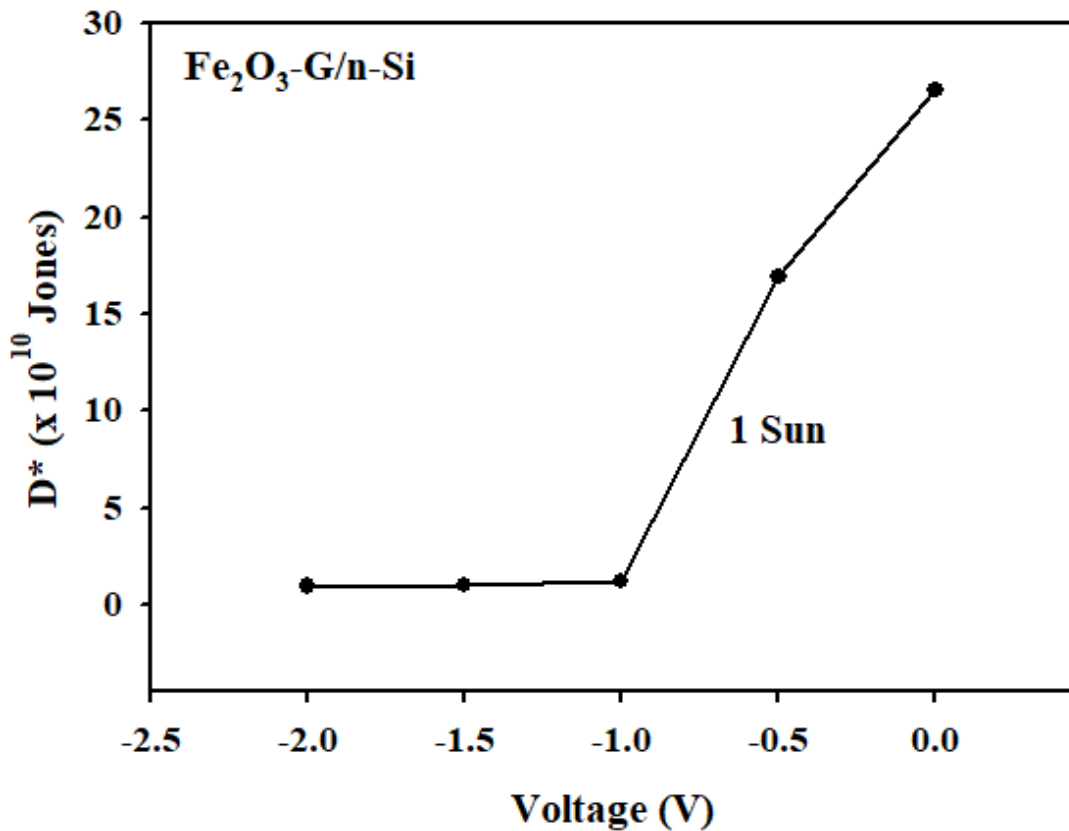


Figure 10. Dependence of D^* on applied voltage for the $\text{Fe}_2\text{O}_3\text{-G/n-Si}$ device

Table 4. Variation in D^* of the $\text{Fe}_2\text{O}_3\text{-G/n-Si}$ device with different applied voltages

Device	Ambient	Specific Detectivity (D^*) ($\times 10^{10}$ (Jones))				
		0V	-0.5V	-1V	-1.5V	-2V
$\text{Fe}_2\text{O}_3\text{-G/n-Si}$	1 Sun	26.6	16.9	1.17	1.03	0.95

The higher the D^* value, the better the photodetector is at distinguishing the signal from the noise, making it more sensitive to weak light signals. This metric is particularly important in applications where detecting faint or low-intensity light is critical. The results show that the highest D^* value is achieved at 0 V, and it decreases as the reverse bias voltage increases. This behavior can be understood by considering the factors that influence D^* . At 0 V, the dark current (I_d) is relatively low, which minimizes the noise in the device. Since D^* is inversely proportional to the square root of the dark current (I_d), a lower dark current leads to a higher D^* , indicating better sensitivity and noise performance. However, as the reverse bias voltage increases, the dark current typically increases due to enhanced carrier generation within the depletion region of the photodiode. This increase in dark current contributes to higher noise levels (shot noise), which reduces D^* . Consequently, the device becomes less sensitive to weak light signals under higher reverse bias conditions. In summary, the decrease in D^* with increasing reverse bias voltage is due to the rise in dark current, which introduces more noise and diminishes the photodiode's ability to detect low-intensity light efficiently.

Conclusion

In this study, $\text{Fe}_2\text{O}_3\text{-G}$ composite material was successfully synthesized as an interlayer on n-Si substrates, and its effect on device performance was evaluated through I-V measurements. The structural and optical properties of the $\text{Fe}_2\text{O}_3\text{-G}$ composite material were investigated through XRD, SEM/EDS, and UV-Vis spectroscopy. The obtained results confirmed that the $\text{Fe}_2\text{O}_3\text{-G}$ composite materials were successfully synthesized. The data from XRD, SEM/EDS, and UV-Vis analyses clearly indicated the proper formation of the composite structure, along with its expected physical and optical properties. Additionally, to provide a comprehensive analysis of the electrical properties, both the $\text{Fe}_2\text{O}_3\text{-G/n-Si}$ device and a reference

device were fabricated for comparison purposes. Both the Fe₂O₃-G/n-Si device and the reference device exhibited good rectifying characteristics, indicating their potential effectiveness in electronic applications. Key electrical parameters were determined using various methods, reinforcing the reliability of the findings. Under illumination at 1 sunlight intensity, the Fe₂O₃-G/n-Si device exhibited notable photoelectrical properties, particularly its self-powered behavior, which enables operation without an external power source. This feature demonstrates strong potential for developing efficient, self-powered photodetectors. The ability to function in remote or off-grid locations is particularly beneficial for applications such as environmental monitoring, remote sensing, and wearable electronics. By eliminating the need for external power, these devices also reduce maintenance costs and enhance sustainability, making them ideal for low-power and autonomous technologies.

Acknowledgements

The author would like to express gratitude to Nanografi Company for supplying the graphene used in this study.

Peer-review: Externally peer-reviewed.

Author Contributions: Concept –ED.; Design-ED.; Materials –GB.; Data Collection and/or Processing –ED.; Analysis and/or Interpretation –ED.; Literature Search –ED.; Writing Manuscript –ED, GB.; Critical Review –GB.

Conflict of Interest: The authors have no conflicts of interest to declare.

Financial Disclosure: The authors declared that this study has received no financial support.

Hakem Değerlendirmesi: Dış bağımsız.

Yazar Katkıları: Konsept –ED.; Tasarım –ED.; Malzemeler –GB.; Veri Toplama ve/veya İşleme –ED.; Analiz ve/veya Yorum –ED.; Literatür Taraması –ED.; Yazma –ED, GB.; Eleştirel İnceleme –GB.

Çıkar Çatışması: Yazarlar, çıkar çatışması olmadığını beyan etmiştir.

Finansal Destek: Yazarlar, bu çalışma için finansal destek almadığını beyan etmiştir.

References

- Abdel-Salam, A. I., Gomaa, I., Khalid, A., & Soliman, T. S. (2022). Investigation of raman spectrum, structural, morphological, and optical features of Fe₂O₃ and Fe₂O₃/reduced graphene oxide hybrid nanocomposites. *Physica Scripta*, 97(12), 125807. <https://doi.org/10.1088/1402-4896/ac9c38>
- Alam, N., Ullah, A., Khan, Y., Oh, W. C., & Ullah, K. (2018). Fabrication and enhancement in photoconductive response of α -Fe₂O₃/graphene nanocomposites as anode material. *Journal of Materials Science Materials in Electronics*, 29(20), 17786–17794. <https://doi.org/10.1007/s10854-018-9886-2>
- Alshareefi, S. J. A., & Al-Nafiey, A. (2024). Graphene and ZnO NPs-enhanced photodetectors based on SiO NWs: Synthesis, characterization, and applications. *Results in Optics*, 16, 100690. <https://doi.org/10.1016/j.rio.2024.100690>
- Aydoğan, A., İncekara, M., & Türüt, A. (2010). Determination of contact parameters of Au/Carmine/n-Si Schottky device. *Thin Solid Films*, 518(23), 7156–7160. <https://doi.org/10.1016/j.tsf.2010.06.019>
- Bozkurt, G. (2020). Synthesis and Characterization of α -Fe₂O₃ Nanoparticles by Microemulsion Method. *Erzincan Üniversitesi Fen Bilimleri Enstitüsü Dergisi*, 13(2), 890–897. <https://doi.org/10.18185/erzifbed.742160>
- Can, M. M., Coşkun, M., & Fırat, T. (2012). A comparative study of nanosized iron oxide particles; magnetite (Fe₃O₄), maghemite (γ -Fe₂O₃) and hematite (α -Fe₂O₃), using ferromagnetic resonance. *Journal of Alloys and Compounds*, 542, 241–247. <https://doi.org/10.1016/j.jallcom.2012.07.091>
- Daş, E. (2022). Some Electrical and Photoelectrical Properties of Conducting Polymer Graphene Composite /n-Silicon Heterojunction Diode. *Sakarya University Journal of Science*, 26(5), 1000–1009. <https://doi.org/10.16984/saufenbilder.1129742>
- Daş, E., İncekara, U., & Aydoğan, A. (2021). A comparative study on electrical characteristics of Ni/n-Si and Ni/p-Si Schottky diodes with Pinus Sylvestris Resin interfacial layer in dark and under illumination at room temperature. *Optical Materials*, 119, 111380. <https://doi.org/10.1016/j.optmat.2021.111380>
- Daş, E., & Yurtcan, A. B. (2022). Synthesis of Reduced Graphene Oxide (rGO) Supported Pt Nanoparticles via Supercritical Carbon Dioxide Deposition Technique for PEM Fuel Cell Electrodes. *Journal of Anatolian Physics and Astronomy*, 1(2), 1–17.
- Erdoğan, M., Orhan, Z., & Daş, E. (2022). Synthesis of electron-rich thiophene triphenylamine based organic material for photodiode applications. *Optical Materials*, 128, 112446. <https://doi.org/10.1016/j.optmat.2022.112446>

- Gao, W., Li, Y., Zhao, J., Zhang, Z., Tang, W., Wang, J., Wu, Z., & Li, Z. (2022). Design and Preparation of Graphene/Fe₂O₃ Nanocomposite as Negative Material for Supercapacitor. *Chemical Research in Chinese Universities*, 38(4), 1097–1104. <https://doi.org/10.1007/s40242-022-1442-1>
- Ghobadi, A., Ghobadi, T. G. U., Karadas, F., & Ozbay, E. (2019). Semiconductor Thin Film Based Metasurfaces and Metamaterials for Photovoltaic and Photoelectrochemical Water Splitting Applications. *Advanced Optical Materials*, 7(14). <https://doi.org/10.1002/adom.201900028>
- Güllü, Ö., Aydoğan, Ş., & Türüt, A. (2008). Fabrication and electrical properties of Al/Safranin T/n-Si/AuSb structure. *Semiconductor Science and Technology*, 23(7), 075005. <https://doi.org/10.1088/0268-1242/23/7/075005>
- Gupta, R., Ghosh, K., & Kahol, P. (2009). Fabrication and electrical characterization of Au/p-Si/STO/Au contact. *Current Applied Physics*, 9(5), 933–936. <https://doi.org/10.1016/j.cap.2008.09.007>
- Han, L. H., Liu, H., & Wei, Y. (2011). In situ synthesis of hematite nanoparticles using a low-temperature microemulsion method. *Powder Technology*, 207(1–3), 42–46. <https://doi.org/10.1016/j.powtec.2010.10.008>
- Idisi, D. O., Ahia, C. C., Meyer, E. L., Bodunrin, J. O., & Benecha, E. M. (2023). Graphene oxide:Fe₂O₃ nanocomposites for photodetector applications: experimental and ab initio density functional theory study. *RSC Advances*, 13(9), 6038–6050. <https://doi.org/10.1039/d3ra00174a>
- Kim, S., Kim, M., & Kim, H. (2024). Self-powered photodetectors based on two-dimensional van der Waals semiconductors. *Nano Energy*, 109725. <https://doi.org/10.1016/j.nanoen.2024.109725>
- Li, Y., & Park, C. W. (1998). Particle Size Distribution in the Synthesis of Nanoparticles Using Microemulsions. *Langmuir*, 15(4), 952–956. <https://doi.org/10.1021/la980550z>
- Lu, W., Guo, X., Yang, B., Wang, S., Liu, Y., Yao, H., Liu, C., & Pang, H. (2019). Synthesis and Applications of Graphene/Iron(III) Oxide Composites. *ChemElectroChem*, 6(19), 4922–4948. <https://doi.org/10.1002/celc.201901006>
- Middya, S., Layek, A., Dey, A., Datta, J., Das, M., Banerjee, C., & Ray, P. P. (2014). Role of zinc oxide nanomorphology on Schottky diode properties. *Chemical Physics Letters*, 610–611, 39–44. <https://doi.org/10.1016/j.cplett.2014.07.003>
- Muhajir, M., Puspitasari, P., & Razak, J. A. (2019). Synthesis and Applications of Hematite α -Fe₂O₃: a Review. *Journal of Mechanical Engineering Science and Technology (JMEST)*, 3(2), 51–58. <https://doi.org/10.17977/um016v3i22019p051>
- Norde, H. (1979). A modified forward I-V plot for Schottky diodes with high series resistance. *Journal of Applied Physics*, 50(7), 5052–5053. <https://doi.org/10.1063/1.325607>
- Orhan, Z., Cinan, E., Çaldıran, Z., Kurucu, Y., & Daş, E. (2020). Synthesis of CuO–graphene nanocomposite material and the effect of gamma radiation on CuO–graphene/p-Si junction diode. *Journal of Materials Science Materials in Electronics*, 31(15), 12715–12724. <https://doi.org/10.1007/s10854-020-03823-8>
- Ramakrishnan, K., Ajitha, B., & Reddy, Y. a. K. (2023). Review on metal sulfide-based nanostructures for photodetectors: From ultraviolet to infrared regions. *Sensors and Actuators. A, Physical*, 349, 114051. <https://doi.org/10.1016/j.sna.2022.114051>
- Saleem, S., Ashiq, M. N., Manzoor, S., Ali, U., Liaqat, R., Algahtani, A., Mujtaba, S., Tirth, V., Alsuhaibani, A. M., Refat, M. S., Ali, A., Aslam, M., & Zaman, A. (2023). Analysis and characterization of opto-electronic properties of iron oxide (Fe₂O₃) with transition metals (Co, Ni) for the use in the photodetector application. *Journal of Materials Research and Technology*, 25, 6150–6166. <https://doi.org/10.1016/j.jmrt.2023.07.065>
- Sarkar, K., & Kumar, P. (2024). Nanostructured carbon heterojunctions for broadband photodetection: Development roadmap, emerging technologies, and future perspectives. *Carbon*, 219, 118842. <https://doi.org/10.1016/j.carbon.2024.118842>
- Sun, M., Liu, H., Liu, Y., Qu, J., & Li, J. (2015). Graphene-based transition metal oxide nanocomposites for the oxygen reduction reaction. *Nanoscale*, 7(4), 1250–1269. <https://doi.org/10.1039/c4nr05838k>
- Talebi, S., & Eshghi, H. (2023). Achievement of high infrared photoresponse in n-MoO₃/p-Si heterostructure photodiode prepared via the thermal oxidation method, the influence of oxygen flow rate. *Materials Chemistry and Physics*, 303, 127792. <https://doi.org/10.1016/j.matchemphys.2023.127792>
- Wang, S., Liu, H., Cao, Z., Wang, X., Zhang, L., Ding, J., Xue, Y., Han, T., Li, F., Shan, L., & Long, M. (2023). Highly Sensitive Long-Wave Infrared Photodetector Based on Two-Dimensional Hematite α -Fe₂O₃. *Advanced Optical Materials*, 11(19). <https://doi.org/10.1002/adom.202300382>
- Xiong, G., Zhang, G., & Feng, W. (2024). High performance photodetectors by integrating CsPbBr₃ perovskite directly on the germanium wafer. *Materials Research Bulletin*, 179, 112959. <https://doi.org/10.1016/j.materresbull.2024.112959>
- Yildirim, G. B., & Daş, E. (2023). The synthesis of MgO and MgO-graphene nanocomposite materials and their diode and photodiode applications. *Physica Scripta*, 98(8), 085911. <https://doi.org/10.1088/1402-4896/ace249>

Yurtcan, A. B., & Daş, E. (2018). Chemically synthesized reduced graphene oxide-carbon black based hybrid catalysts for PEM fuel cells. *International Journal of Hydrogen Energy*, 43(40), 18691–18701. <https://doi.org/10.1016/j.ijhydene.2018.06.186>

Dosimetric Investigation of Acetaminophen Drug Raw Materials by Electron Paramagnetic Resonance Spectroscopy

Firat AKBALIK

Akyurt Anatolian High Scholl, Ankara, Turkey



Acetaminophen İlaç Hammaddelerinin Elektron Paramanyetik Rezonans Spektroskopisi ile Dozimetrik İncelenmesi

Abstract

In this study, powdered crystals of paracetamol, a drug active ingredient known for its use in alleviating postoperative pain and as an adjuvant in chemotherapy for cancer patients, were exposed to gamma radiation. The paramagnetic defects induced by the radiation were thoroughly investigated using Electron Paramagnetic Resonance (EPR) spectroscopy. The suitability of the drug sample for use as a dosimetric material, radical extinction data, saturation information occurring at microwave power values and parameters related to dose-response data were investigated at room temperature. No EPR signal was observed in the sample which was not exposed to gamma radiation. Spectroscopic properties generated as a result of radiation were determined via spectrum simulation.

Keywords: Dosimetry, Gamma Radiation, Drug sample, EPR, Radical, Irradiation.

Öz

Bu çalışmada, ameliyat sonrası ağrıların hafifletilmesi ve kanser hastalarında kemoterapi tedavisinde destekleyici olarak kullanıldığı bilinen parasetamolün toz kristalleri gama radyasyonuna maruz bırakılmıştır. Radyasyon sonucu oluşan paramanyetik bozukluk, Elektron Paramanyetik Rezonans (EPR) spektroskopisi kullanılarak detaylı bir şekilde incelenmiştir. Örneğin dozimetrik malzeme olarak kullanıma uygunluğu, radikal sönüm bilgileri, mikrodalga güç değerlerinde doyum bilgileri ve doz-cevap eğrisi oda sıcaklığında araştırılmıştır. Gama radyasyonuna maruz bırakılmayan örnekte EPR sinyali gözlenmemiştir. Spektrum simülasyonu (benzetişimi) yapılarak ışınlama sonucunda ortaya çıkan spektroskopik özellikleri belirlenmiştir.

Anahtar Kelimeler: Dozimetri, Gama radyasyonu, ilaç örneği, EPR, Radikal, Işınlama.



Sorumlu Yazar/Corresponding Author:

F. Akbalık

E-mail: fakbalik@gmail.com

Geliş Tarihi/Received 27.06.2024

Kabul Tarihi/Accepted 18.11.2024

Yayın Tarihi/ 12.12.2024

Publication Date

Cite this article

Akbalık, F. (2024) Dosimetric Investigation of Acetaminophen Drug Raw Materials by Electron Paramagnetic Resonance Spectroscopy. *Journal of Anatolian Physics and Astronomy*, 3(2), 75-82.

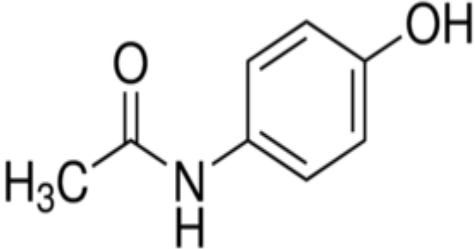
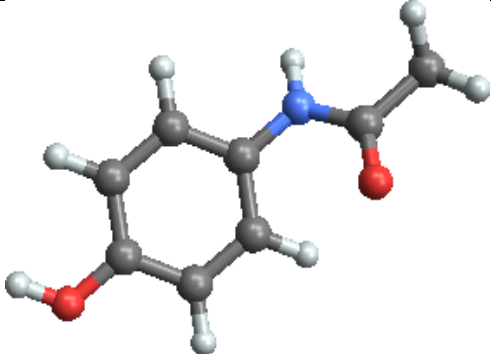


Content of this journal is licensed under a Creative Commons Attribution-Noncommercial 4.0 International License.

Introduction

Studies using EPR spectroscopy, a branch of atomic and molecular physics, can be used to detect free radicals formed in active pharmaceutical ingredients by ionising radiation and to obtain data on the dispersion of a single electron on the molecule (Abbar et al., 2011; Akbalik, 2016; Ghasemi & Bagheri, 2019; Basly & Bernand, 1997; Basly et al., 1997; Bhat et al., 2011; Damian, 2003; Fincur et al., 2021; Gibella et al., 1993; Jeon et al., 2021; Osawa et al., 2019; Polat & Korkmaz, 2006; Proelss et al., 1978; Smyth et al., 2006). The results of EPR spectroscopy studies of irradiated drug samples have shown EPR spectroscopy to be a highly effective method for characterising irradiation-induced free radicals (Basly & Bernand, 1997; Basly et al., 1997; Gibella et al., 1993; Damian, 2003; Polat & Korkmaz, 2006). The molecular formula of Acetaminophen drug is $\text{CH}_3\text{CONHC}_6\text{H}_4\text{OH}$. Its chemical formula is N-acetyl-4-aminophenol and its molecular weight is 151.163 g/mol. Table 1 shows the information of Acetaminophen drug sample.

Table 1. Chemical structure, ring formula, molecular weight and chemical structure of Acetaminophen drug sample

 	
2D chemical structure of Acetaminophen powder crystals	
Ring Formula	$\text{CH}_3\text{CONHC}_6\text{H}_4\text{OH}$
Molecular Weight	151.163 g/mol
Chemical Name	Acetaminophen

The maximum radiation dose that can be used for drug samples accepted by Pharmacopeia (USP XXII, BP 1993) is selected as 25 kGy. During the experimental studies, the Acetaminophen drug sample was irradiated at doses of 1, 5, 10, 15, and 20 kGy and their spectra were recorded. The current study aims to determine the spectral properties of free radicals formed in the Acetaminophen drug sample irradiated with γ -rays and to determine whether they can be used as an example for normal and/or accidental dosimetry by creating dose-response curves as a result of EPR examination at room temperature. In addition, EPR is also used in accident dosimetry.

Material and Method

Irradiations at all doses were carried out with a Cobalt-60 gamma source having an activity of 370.000 curies and a dose rate of 2 kGy/hr at the Industrial Irradiation Facility of Sarayköy Nuclear Research Center SANAEM, now known as TENMAK, located in Kahramankazan district affiliated to the Turkish Atomic Energy Authority. The products to be irradiated in the gamma irradiation facilities in the experimental field are processed in sample packages dosimeters are placed in the product boxes and process control is performed. The samples used in the current study were prepared in a 2 ml Eppendorf tube, placed in the unit, and irradiated. Six prepared samples were irradiated at doses of 1 kGy, 5 kGy, 10 kGy, 15 kGy, and 20 kGy respectively on different dates. Even though Acetaminophen is generally used in the treatment of moderate pain, it is also known to be used to reduce the severity of post operative pain and for chemotherapy in cancer patients. The powder samples of the active pharmaceutical ingredient were placed in an Eppendorf tube with no treatment, and EPR spectra were recorded under various spectrometer operating conditions (Bruker e-scan X-band EPR spectrometer: center magnetic field 349 mT, scan range 10 mT, microwave power ~ 0.1 mW, microwave frequency 9.8 GHz, receiver gain 3.17×10^2 , modulation frequency 86 kHz, modulation amplitude 2 G). All spectra measurements were recorded at room temperature.

Results

Unirradiated and irradiated samples

Except for gamma irradiation, no other physical or chemical treatment was performed on the Acetaminophen drug sample used in the present study. EPR spectra were recorded after the Acetaminophen drug sample was irradiated with γ -rays at certain dose levels. The untreated Acetaminophen sample was irradiated and EPR spectra were recorded. While no EPR signal was observed in the unirradiated Acetaminophen sample, it was recorded that the irradiated Acetaminophen sample gave an EPR spectrum. At this stage, no resonance signal was observed in the Acetaminophen sample before irradiation, while the observation of a significant resonance signal after irradiation gave information about the formation of unpaired electrons in the sample by irradiation. The spectrum shows an EPR spectrum dispersed on an area of 20 mT. Through the simulation program, the excess fine structure constant was calculated as $a=1.1494$ mT and the line width as 3.26 mT. The simulation of irradiated Acetaminophen was obtained using Mc Kelvey software. It was observed that no EPR signal was obtained in the unirradiated sample. Figure 1(a) shows the resonance signals in the irradiated samples from low to high doses that become more significant and stronger depending on the dose value. When Figure 1(a) was examined, the EPR spectrum is seen with an approximate g value of 2.0040. Figure 1(b) shows the spectrum irradiated at a dose of 20 kGy. Figure 1(c) shows the simulation spectrum of the sample irradiated at 20 kGy dose.

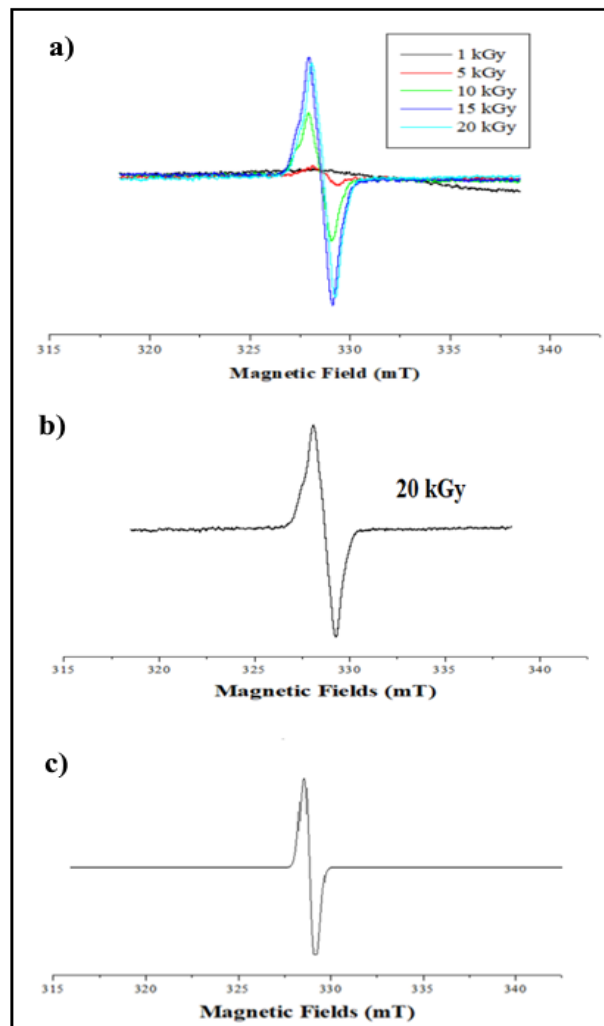


Figure 1a. Spectra obtained from irradiated Acetaminophen drug sample. **1b.** EPR spectrum of acetaminophen drug sample at 20 kGy dose. **1c.** The closest simulation spectrum of the Acetaminophen drug sample obtained at a dose of 20 kGy

Change of EPR signal intensity with microwave power

In this section of the study, EPR spectra of Acetaminophen drug samples irradiated at 10 kGy dose value were recorded at different microwave power values in the range of 0.01-0.1-2-3-4-6-8, and 15 mW. Table 2 shows the microwave power $P^{1/2}(\text{mW})^{1/2}$ and the resonance signal intensity. Origin 6.0 program was used to calculate the resonance signal intensity and the signal intensities were calculated by determining the strong peaks from peak to peak in the spectrum produced using numerical values with the program. Accordingly, the corresponding resonant signal intensity deviates from linearity and reaches saturation at approximately 8 mW power value.

Table 2 Microwave Power $P^{1/2}(\text{mW})^{1/2}$ and resonance signal intensity.

Values of the resonance signal intensity of the Acetaminophen sample depending on the square root of the applied microwave power.

Microwave Power $P^{1/2}(\text{mW})^{1/2}$	0.1	0.15	2	3	4	6	8	15
Central Resonance Signal Intensity (a.u.)	17.02	28.167	43.464	46.8	48.44	48.74	50	49.38

Figure 2 shows the variation of the microwave power of Acetaminophen drug depending on the signal intensity, and Figure 3 shows the spectra of the irradiated Acetaminophen drug sample obtained at 0.1-...-15 mW microwave area values.

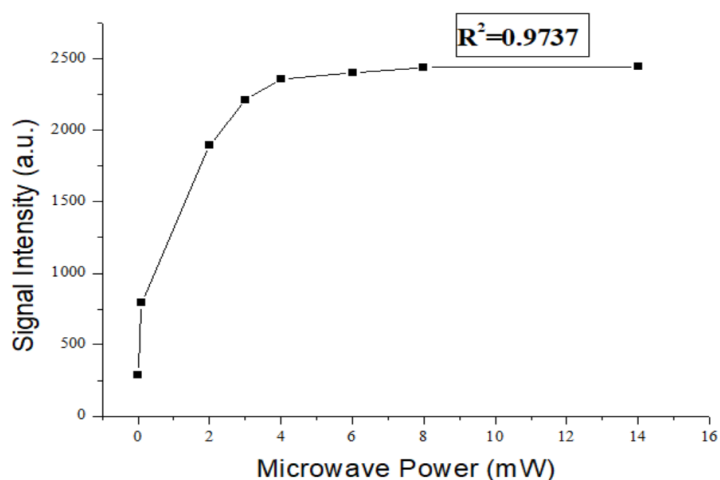


Figure 2. Variation of microwave power of Acetaminophen drug with signal intensity.

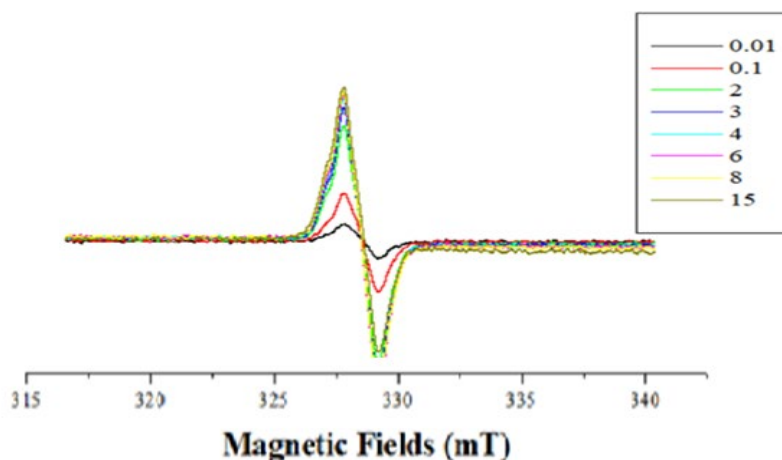


Figure 3. Spectra of irradiated Acetaminophen drug sample obtained different microwave power

Dose-response curve of Acetaminophen sample

In this section, examinations were conducted to determine the dosimetric potential of the Acetaminophen drug sample. The most appropriate mathematical functions that can describe the dose-dependent variations of the resonance signal intensity results were determined by the mathematical functions given in the graph. Figure 4 shows the dose-dependent variations in the resonance signal intensity of the irradiated samples.

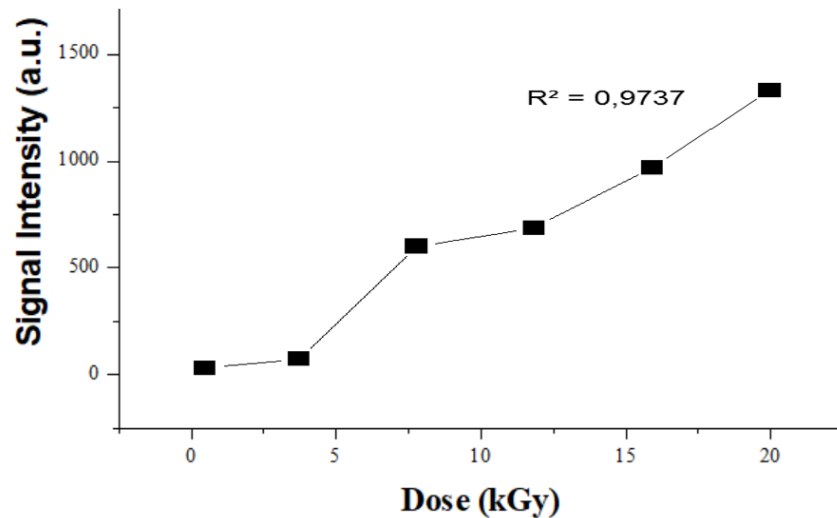


Figure 4. Variation of the signal intensity of irradiated Acetaminophen sample depending on the radiation dose applied

Table 3. Parameter values and coefficients of concordance calculated for three different mathematical functions tested using resonance signal intensity (I) values.

Function	Parameters	I
$I = a + D \ln(x)$ (Logarithmic)	A	5.172
	B	41.396
	C
	R^2	0.9671
$I = a + bD + cD^2$ (Polynomial)	A	13.977
	B	66.077
	C	0.304
	R^2	0.9737
$I = aD^b$ (Exponential)	A	96.09
	B	0.8749
	C
	R^2	0.9039

Although the radiation dose applied to the sample increased, no significant change was observed in the g value and EPR spectrum form of the sample. However, as shown in Figure 4, as the amount of radiation absorbed by the sample increased, there is a significant increase in the intensity of the EPR resonance signal obtained. Where I is the resonance signal intensity measured from the EPR spectrum of the sample and D is the radiation dose applied to the sample. The values shown as squares in Figure 4 show the experimental results. The mathematical functions closest to the experimental results were tested. The most appropriate mathematical functions to describe the dose-dependent changes of the resonance signal intensity findings were determined by trying the mathematical functions given in Table 3. For example, it was found that the dose-response curve was compatible with logarithmic, polynomial, and exponential functions. The best fit of the

experimental results was determined by the biggest value of $R^2=0.9737$. One of the necessary conditions for a material to be used dosimetrically is that the dose-response curve should be linear. When the table was analyzed, it was determined that the curve obtained showed the best fit with the polynomial function $I=a+bD+cD^2$. As the acetaminophen sample showed linearity, it is considered that it can be used as a dosimetric material.

Extinction findings of gamma irradiated Acetaminophen drug

After acetaminophen was irradiated with 20 kGy, the EPR spectra were recorded at regular intervals in a dark environment at room temperature and kept airtight. Figure 5 shows the variation of the central resonance signal intensity calculated from the spectra obtained over a period of 145 days after gamma irradiation of the sample depending on the dwell time. The regions with a black square in the figure show the peak-to-peak signal values exposed in the spectrum. When the EPR spectra were examined during this process, a decrease in the resonance signal of the sample was observed proportional to the elapsed time, and when the change in the peak-to-peak signal values was examined, it was found that the decrease in the extinction kinetics was 18% on the 30th day, the extinction kinetics reached 30% on the 53rd day, and the decrease in the extinction kinetics was 70% in the measurement taken on the 145th day.

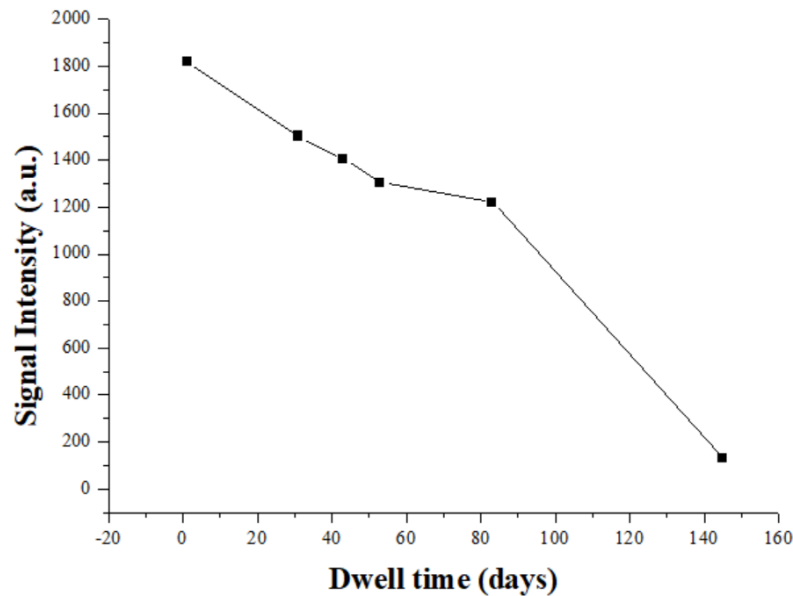


Figure 5. The central resonance signal intensity was calculated from the spectra obtained over 145 days.

The resonance signal obtained from irradiation in irradiated drugs should be testable throughout the shelf life of the sample. Although the resonance signal can be measured weakly, in the spectrum taken at the end of the 145th day in the Acetaminophen sample, it showed that even at the end of the 145th day, the irradiated Acetaminophen sample can be differentiated from the unirradiated sample using the EPR spectrometry method. Also, it was found that there was no significant change in the g -value measurements during this period. Figure 5 shows the variation of the resonance signal intensity of the irradiated Acetaminophen sample depending on the dwell time.

Conclusion

Acetaminophen, which is widely used in the USA, Canada, Japan, South Korea, and Colombia, is a medication commonly used to reduce the severity of post-operative pain and in anthracycline chemotherapy for cancer patients, although it is also used to treat moderate pain. Anthracyclines, used in cancer treatment, are known for their wide application in the treatment of various types of cancer, including leukemia, breast cancer, uterine cancer, and lung cancer (Ghasemi & Bagheri, 2019). The EPR spectrum of Acetaminophen drug sample irradiated with gamma rays was observed. It was determined that the form revealed in the spectrum did not change depending on the applied dose variation, and the signal strength increased in the spectrum. In Acetaminophen sample, it was observed that at approximately 8 mW power, the resonance signal intensity deviated from linearity and saturated. The mathematical functions closest to the experimental results were tested with the dose response study. The most appropriate mathematical functions that can describe the dose-dependent variations of experimental resonance signal intensity findings were tried. For example, it was determined that the dose-response curve was highly compatible with linear, exponential, and polynomial functions. The smallest value of the best fit of the experimental results was determined with $R^2=0.9737$. Acetaminophen spectrum simulation was performed by evaluating the extinction results at room temperature. It was concluded that the theoretical spectrum created by using the calculated theoretical spectroscopic parameter values was in good fit with the experimental spectrum and was appropriate and successful in terms of evaluating the results.

The absence of EPR signal in the Acetaminophen drug sample before irradiation and the dose-response curve showing linearity in a wide range are positive results in dosimetric terms. When the EPR spectra were examined in the extinction spectra, a decrease in the resonance signal of the sample proportional to the elapsed time was observed, and when the change in peak-to-peak signal values was examined by origin 6.0 program, it was observed that the decrease in extinction kinetics on the 30th day was 18%, the extinction kinetics reached 30% on the 53rd day, and the decrease in extinction kinetics in the measurement taken on the 145th day was 70%. According to these results, it can be said that if the Acetaminophen drug sample irradiated at a dose of 20 kGy is used for dosimetric purposes, no disadvantage can be stated when the measurement is made within two days following the irradiation process.

Acknowledgement: I would like to thank Prof. Dr. Şemsettin OSMANOĞLU and Dicle University Institute of Science.

Hakem Değerlendirmesi: Dış bağımsız.

Çıkar Çatışması: Yazar, çıkar çatışması olmadığını beyan etmiştir.

Finansal Destek: Bu çalışma Dicle Üniversitesi Fen Bilimleri Enstitüsü "'Fen15-001" no ile finance edilmiştir.

Peer-review: Externally peer-reviewed.

Conflict of Interest: The author have no conflicts of interest to declare.

Financial Disclosure: This study was financed by Dicle University Institute of Science with the number "'Fen15-001"

References

- Abbar, J. C., Lamani, S. D., & Nandibewoor, S. T. (2011). Ruthenium(III) Catalyzed Oxidative Degradation of Amitriptyline-A Tricyclic Antidepressant Drug by Permanganate in Aqueous Acidic Medium. *Journal of Solution Chemistry*, 40(3), 502–520. <https://doi.org/10.1007/s10953-011-9655-9>
- Akbalık, F. (2016). Analysis of structural defects caused by gamma radiation on some medicines through electron paramagnetic resonance and simulation techniques. PhD thesis, Dicle University.
- Basly, J., & Bernard, M. (1997). Radio sterilization dosimetry by ESR spectroscopy: Ritodrine hydrochloride and comparison with other sympathomimetics. *International Journal of Pharmaceutics*, 149(1), 85–91. [https://doi.org/10.1016/s0378-5173\(96\)04855-7](https://doi.org/10.1016/s0378-5173(96)04855-7)
- Basly, J., Longy, I., & Bernard, M. (1997). ESR identification of radiosterilized pharmaceuticals: latamoxef and ceftriaxone. *International Journal of Pharmaceutics*, 158(2), 241–245. [https://doi.org/10.1016/s0378-5173\(97\)00257-3](https://doi.org/10.1016/s0378-5173(97)00257-3)
- Bhat, R., & Sridhar, K. (2011). Influence of ionizing radiation and conventional food processing treatments on the status of free radicals in lotus seeds: An ESR study. *Journal of Food Composition and Analysis*, 24(4–5), 563–567. <https://doi.org/10.1016/j.jfca.2010.12.008>
- Damian, G. (2003). EPR investigation of γ -irradiated anti-emetic drugs. *Talanta*, 60(5), 923–927.

[https://doi.org/10.1016/s0039-9140\(03\)00153-x](https://doi.org/10.1016/s0039-9140(03)00153-x)

Finčur, N. L., Grujić-Brojčin, M., Šćepanović, M. J., Četojević-Simin, D. D., Maletić, S. P., Stojadinović, S., & Abramović, B. F. (2021). UV-driven removal of tricyclic antidepressive drug amitriptyline using TiO₂ and TiO₂/WO₃ coatings. *Reaction Kinetics Mechanisms and Catalysis*, 132(2), 1193–1209. <https://doi.org/10.1007/s11144-021-01936-7>

Ghasemi, A., & Bagheri, A. (2019). Effects of alkyl chain length on synergetic interaction and micelle formation between a homologous series of n-alkyltrimethylammonium bromides and amphiphilic drug propranolol hydrochloride. *Journal of Molecular Liquids*, 298, 111948. <https://doi.org/10.1016/j.molliq.2019.111948>

Gibella, M., Crucq, A., & Tilquin, B. (1993). Détection RPE de l'irradiation de médicaments. *Journal De Chimie Physique*, 90, 1041–1053. <https://doi.org/10.1051/jcp/1993901041>

Jeon, M., Jun, B., Kim, S., Cho, J., Park, C. M., Choong, C. E., Jang, M., & Yoon, Y. (2021). Sonodegradation of amitriptyline and ibuprofen in the presence of Ti₃C₂T_x MXene. *Journal of Hazardous Materials Letters*, 2, 100028. <https://doi.org/10.1016/j.hazl.2021.100028>

Osawa, R. A., Barrocas, B. T., Monteiro, O. C., Oliveira, M. C., & Florêncio, M. H. (2019). Visible light photocatalytic degradation of amitriptyline using cobalt doped titanate nanowires: Kinetics and characterization of transformation products. *Journal of Environmental Chemical Engineering*, 8(1), 103585. <https://doi.org/10.1016/j.jece.2019.103585>

Polat, M., & Korkmaz, M. (2006). Effect of radiation on solid paracetamol: ESR identification and dosimetric features of γ -irradiated paracetamol. *Radiation Effects and Defects in Solids*, 161(1), 51–62. <https://doi.org/10.1080/10420150500467471>

Proelss, H. F., Lohmann, H. J., & Miles, D. G. (1978). High-performance liquid-chromatographic simultaneous determination of commonly used tricyclic antidepressants. *Clinical Chemistry*, 24(11), 1948–1953. <https://doi.org/10.1093/clinchem/24.11.1948>

Smyth, W. F., Leslie, J. C., McClean, S., Hannigan, B., McKenna, H. P., Doherty, B., Joyce, C., & O'Kane, E. (2006). The characterisation of selected antidepressant drugs using electrospray ionisation with ion trap mass spectrometry and with quadrupole time-of-flight mass spectrometry and their determination by high-performance liquid chromatography/electrospray ionisation tandem mass spectrometry. *Rapid Communications in Mass Spectrometry*, 20(11), 1637–1642. <https://doi.org/10.1002/rcm.2485>

Lityum İyon Pillerin Tarihten Bugüne Gelişimi ve Son Teknolojide Geline Nokta

Development of Lithium Ion Batteries From the History of Batteries to the Present and the Latest Technology Statement

Hüseyin PEHLİVAN

Atatürk University, Department of Physics,
Faculty of Sciences, Erzurum, Turkey



Erdoğan ÖZ

Atatürk University, Department of Physics,
Faculty of Sciences, Erzurum, Turkey



Muhammet YILDIRIM

Atatürk University, Institute of Natural and
Applied Sciences, Department of Physics,
Erzurum, Turkey



Öz

Bu derleme makalesi, lityum iyon pillerin antik çağlardan günümüze kadar olan tarihsel gelişimini, çalışma prensiplerini, avantajlarını, dezavantajlarını ve gelecekteki potansiyelini incelemektedir. Lityum iyon piller, yüksek enerji yoğunluğu, uzun çevrim ömrü ve düşük kendi kendine deşarj oranı gibi avantajları sayesinde taşınabilir elektronik cihazlardan elektrikli araçlara ve yenilenebilir enerji depolama sistemlerine kadar çeşitli alanlarda kullanılmaktadır. Bu teknolojinin geleceği, malzeme bilimi, pil tasarımı ve üretim süreçlerindeki yeniliklerle şekillenecektir. Katı hal piller, lityum-sülfür piller ve sodyum-iyon piller gibi alternatif teknolojiler de gelecekte enerji depolama alanında önemli bir rol oynayabilir.

Anahtar Kelimeler: Lityum iyon piller, enerji depolama sistemleri, yenilenebilir enerji, batarya teknolojileri.

Abstract

This review article examines the historical development of lithium-ion batteries from antiquity to the present day and their working principles, advantages, disadvantages, and future potential. Lithium-ion batteries are used in various areas, from portable electronic devices to electric vehicles and renewable energy storage systems, thanks to their advantages such as high energy density, long cycle life, and low self-discharge rate. Innovations in materials science, battery design, and manufacturing processes will shape the future of this technology. Alternative technologies such as solid-state batteries, lithium-sulfur batteries, and sodium-ion batteries may also play an important role in the field of energy storage in the future.

Keywords: Lithium-ion batteries, energy storage systems, renewable energy, battery technologies.

Sorumlu Yazar/Corresponding Author:

H. Pehlivan

E-mail: yildirim_pehlivan@hotmail.com

Geliş Tarihi/Received 31.10.2024

Kabul Tarihi/Accepted 22.11.2024

Yayın Tarihi/ 12.12.2024

Publication Date

Cite this article

Pehlivan, H., Öz, E., & Yıldırım, M., (2024)

Development of Lithium Ion Batteries

From the History of Batteries to the

Present and the Latest Technology

Statement. Journal of Anatolian

Physics and Astronomy, 3(2), 83-94.



Content of this journal is licensed under a Creative
Commons Attribution-Noncommercial 4.0
International License.

Giriş

Modern dünyanın hızla artan enerji talebi, yeni ve verimli enerji depolama çözümlerinin geliştirilmesini kaçınılmaz hale getirmiştir. Bu arayışta, lityum iyon piller yüksek enerji yoğunluğu, uzun çevrim ömrü ve hafiflikleri gibi özellikleriyle öne çıkan bir teknoloji olarak karşımıza çıkmaktadır (Armand & Tarascon, 2008). Taşınabilir elektronik cihazlardan elektrikli araçlara ve yenilenebilir enerji depolama sistemlerine kadar geniş bir yelpazede kullanılan lityum iyon piller, enerji depolama teknolojilerinde devrim yaratmıştır ve yaşam tarzımızı derinden etkilemiştir (Goodenough & Park, 2013).

Lityum iyon pillerinin bu denli yaygınlaşmasının ardında yatan temel etkenlerden biri, sunduğu benzersiz avantajlardır. Li, herhangi bir element arasında en düşük indirgeme potansiyeline sahiptir ve Li bazlı pillerin mümkün olan en yüksek hücre potansiyeline sahip olmasını sağlar (M. Li vd., 2018). Ayrıca, Li üçüncü en hafif elementtir ve herhangi bir tek yüklü iyonun en küçük iyonik yarıçaplarından birine sahiptir (Winter vd., 2018). Bu faktörler, Li bazlı pillerin yüksek gravimetrik ve hacimsel kapasiteye ve güç yoğunluğuna sahip olmasını sağlar (Nitta vd., 2015). Buna ek olarak, düşük kendi kendine deşarj oranları, cihazların şarj edilmeden daha uzun süre bekletilebilmesini sağlar. Bu özellikler, lityum iyon pillerini özellikle taşınabilir elektronik cihazlar ve elektrikli araçlar gibi uygulamalar için ideal bir seçenek haline getirir.

Tüm piller katot ve anottan oluşan iki elektrot ve bu elektrotları iyonik olarak birleştiren elektrolitten oluşur. Her iki elektrot kimyasal yapılarından kaynaklanan kimyasal potansiyel farkına sahiptirler ve bu sayede elektrotlar bir dış devre ile bağlandığında elektronların akışı sağlanır ve bu sayede pil şarj ve deşarj edilebilir. Pillerin içerisindeki bu bileşenlerin özellikleri pillerin çalışma voltajları, kapasiteleri veya çalışma ömürleri gibi birçok önemli özelliği belirler. Örneğin katot olarak LiNiO_2 bileşiği kullanılan bir Li-iyon pilde kapasite 200 mAh/g (Dong vd., 2024) iken LiFePO_4 olan bir pilde yaklaşık 150 mAh/g (Abdelaal & Alkhedher, 2024) olarak ölçülür. Bu nedenle pillerde kullanılan bileşenler seçilirken bunların fiziksel ve kimyasal özellikleri göz önünde bulundurulmalıdır.

Lityum iyon pillerinin yaygın kullanımı, beraberinde bazı zorlukları da getirmektedir. Örneğin pil üretiminde kullanılan hammaddeler giderek tükenmekte ve bunun sonucunda maliyet artışı yaşanmaktadır (Orangi vd., 2024). Buna ek olarak bileşenlerin oksidasyona eğilimli olması sonucu kimyasal reaksiyonlar sonucunda yanma veya patlama riski taşınması ortadaki diğer problemlerden biridir (Chombo & Laonual, 2020). Elektrolit bileşenlerinin geliştirilmesi, elektrotta kullanılan malzemelerin düşük maliyetlilerle değiştirilmesi sentez yöntemlerinin geliştirilmesi gibi çalışmalar bu problemlerin çözümü için bulunan yollardan bazılarıdır. Örneğin Ahmed ve araştırma grubu katot malzemesi sentezi için yeni bir teknik olan eş-çökertme yöntemini kullanarak $\text{LiNi}_{1/3}\text{Mn}_{1/3}\text{Co}_{1/3}\text{O}_2$ katot materyalinin üretim maliyetini yaklaşık olarak %19 oranında azalttığını rapor etmiştir (Ahmed vd., 2017).

Bu derleme makalesi, lityum iyon pillerinin çok yönlü bir incelemesini sunmayı amaçlamaktadır. Tarihsel gelişiminden başlayarak, çalışma prensipleri, avantajları, dezavantajları ve gelecekteki potansiyelleri detaylı bir şekilde ele alınacaktır. Ayrıca, lityum iyon pillerin geri dönüşümü ve sürdürülebilirlik konuları da incelenecek ve bu teknolojinin gelecekteki yönüne ışık tutulacaktır.

1. Pillerin Tarihsel Gelişimi

Elektrokimyasal enerji depolama kavramı, antik çağlara kadar uzanmaktadır. Mezopotamya'da MÖ 250 - MS 640 yılları arasında yapıldığı tahmin edilen Bağdat Pili, bu alandaki en eski örneklerden biridir (Lu & Anariba, 2014). Bir kil kap, bir bakır tüp ve bir demir çubuktan oluşan bu gizemli alet, elektro kaplama veya tıbbi amaçlar için kullanılmış olabileceği düşünülmektedir. Her ne kadar işlevi tam olarak anlaşılmasa da Bağdat Pili, insanlığın elektriği anlama ve kullanma yolculuğunda önemli bir kilometre taşıdır ve günümüz pil teknolojilerinin temelini oluşturan elektrokimyasal prensiplerin antik çağlarda dahi bilindiğini göstermektedir.

Modern pil teknolojisinin doğuşu, 1800 yılında Alessandro Volta'nın volta pilini icat etmesiyle gerçekleşmiştir. Volta, çinko ve bakır diskleri tuzlu suya batırılmış bezlerle ayırarak bir dizi elektrokimyasal hücre oluşturmuş ve bu sayede sürekli elektrik akımı üretebilen bir düzenek geliştirmiştir (Cecchini & Pelosi, 1992). Volta pili, elektrik alanında bir devrim yaratarak, elektrikli telgraf, elektroliz ve elektrikli aydınlatma gibi yeni teknolojilerin gelişmesine zemin hazırlamıştır. Ayrıca, Volta'nın çalışmaları, elektrokimya alanındaki araştırmaları hızlandırmış ve daha gelişmiş pil teknolojilerinin geliştirilmesine yol açmıştır.

19. yüzyıl, pil teknolojilerinde önemli ilerlemelerin kaydedildiği bir dönem olmuştur. 1836 yılında John Frederic Daniell tarafından icat edilen Daniell pili, volta piline göre daha kararlı bir voltaj sağlamıştır (Yuan vd., 2024). 1859 yılında ise Gaston Planté tarafından geliştirilen kurşun-asit pil, şarj edilebilir olması özelliğiyle öne çıkmış ve günümüzde hala otomotiv sektöründe yaygın olarak kullanılmaktadır. Bu dönemde geliştirilen diğer önemli pil teknolojileri arasında Georges Leclanché

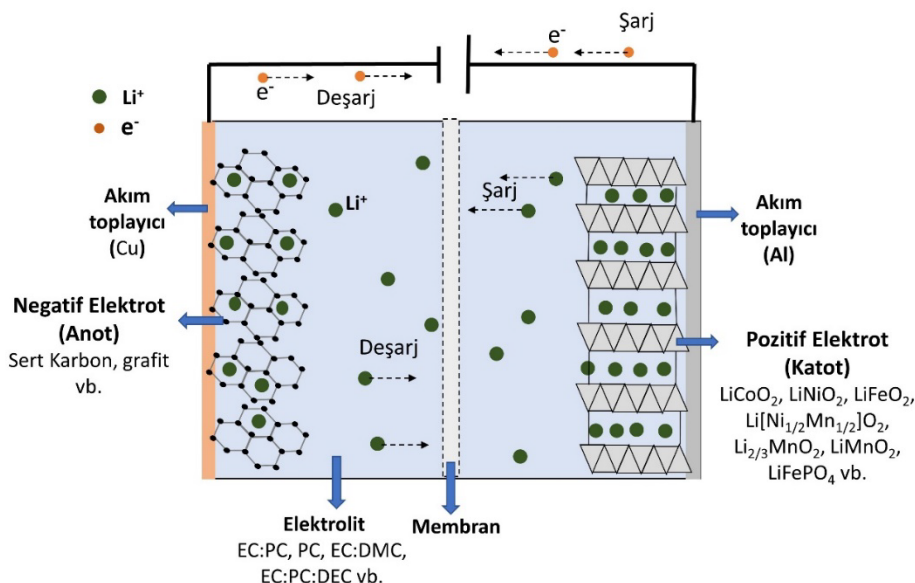
tarafından 1866 yılında icat edilen Leclanché pili ve Carl Gassner tarafından 1886 yılında geliştirilen çinko-karbon pil bulunmaktadır (Kordesch & Taucher-Mautner, 2009). Bu piller, taşınabilir elektrikli cihazların gelişimine katkıda bulunmuş ve günlük yaşamda elektriğin kullanımını yaygınlaştırmıştır.

20. yüzyıl, taşınabilir elektronik cihazların ve elektrikli araçların gelişmesiyle birlikte daha gelişmiş pil sistemlerine olan ihtiyacı artırmıştır. Bu dönemde nikel-kadmiyum (NiCd) (Tsai & Chan, 2013), nikel-metal hidrit (NiMH; Arya & Verma, 2020) ve lityum iyon piller gibi yeni pil teknolojileri ortaya çıkmıştır. Lityum iyon piller, ilk olarak 1970'lerde Stanley Whittingham'ın çalışmalarıyla araştırılmaya başlanmış (Crabtree vd., 2015; Whittingham, 1974) ve 1991 yılında Sony tarafından ticari olarak piyasaya sürülerek taşınabilir elektronik cihazlar ve daha sonra elektrikli araçlar için vazgeçilmez bir enerji kaynağı haline gelmiştir (Mizushima vd., 1980). Bu dönemde pil teknolojilerindeki gelişmeler, elektronik cihazların minyatürleştirilmesi ve performanslarının artırılmasında önemli rol oynamıştır.

Günümüzde ise lityum iyon pil teknolojisi, baş döndürücü bir hızla ilerlemeye devam etmekte ve enerji depolama alanında sınırları zorlamaktadır. Günümüzde, lityum iyon piller, akıllı telefonlar ve dizüstü bilgisayarlar gibi günlük hayatta kullandığımız elektronik cihazlardan, elektrikli araçlara ve yenilenebilir enerji depolama sistemlerine kadar geniş bir yelpazede karşımıza çıkmaktadır. Bu hızlı gelişim, farklı ihtiyaçlara cevap verebilen çeşitli lityum iyon pil kimyalarının ortaya çıkmasını sağlamıştır. Örneğin, taşınabilir elektronik cihazlarda ağırlıklı olarak lityum kobalt oksit (LiCoO_2) katotlu piller kullanılırken (Lyu vd., 2021), elektrikli araçlarda daha yüksek enerji yoğunluğu ve güvenlik sağlayan lityum demir fosfat (LiFePO_4) (Zhu & Chen, 2020) ve lityum nikel mangan kobalt oksit (NMC) katotlu piller tercih edilmektedir (Iturrodoiteia vd., 2017). Bunun yanı sıra, lityum iyon piller, rüzgar, güneş jeotermal gibi yenilenebilir enerji kaynaklarının ürettiği enerjiyi depolama, elektrikli araçlar, portatif elektronik cihazlar gibi çok geniş alanlarda kullanılmaktadır (Kim vd., 2020). Lityum iyon pillerin bu denli yaygınlaşması, teknolojinin sunduğu yüksek enerji yoğunluğu, uzun çevrim ömrü ve tasarım esnekliği gibi avantajların bir sonucudur. Ancak, bu teknolojinin maliyet, güvenlik ve sürdürülebilirlik gibi zorlukları aşarak gelecekte de enerji depolama alanındaki lider konumunu koruyabilmesi için araştırma ve geliştirme çalışmalarına devam edilmesi gerekmektedir.

2. Li-iyon Pillerin Çalışma Prensibi

Lityum iyon piller, lityum iyonlarının anot ve katot arasında tersinir bir şekilde hareket etmesi prensibiyle çalışır (Şekil 1). Şarj işlemi sırasında, harici bir güç kaynağı tarafından sağlanan elektrik enerjisi, lityum iyonlarının anottan ayrılıp elektrolit aracılığıyla katoda göç etmesine neden olur. Katotta, lityum iyonları katot malzemesinin kristal yapısına yerleşir. Deşarj işlemi sırasında ise, katotta depolanan lityum iyonları tekrar elektrolit aracılığıyla anota geri döner ve anot malzemesine yerleşir (Chawla vd., 2019). Bu iyon hareketi, pilin dış devresinde elektron akışına sebep olur ve böylece elektrik enerjisi üretilir. Lityum iyonlarının anot ve katot arasında bu şekilde ileri geri hareketi, pilin tekrar tekrar şarj edilip deşarj edilmesini sağlar. Pilin voltajı ise, kullanılan anot ve katot malzemelerinin elektrokimyasal potansiyelleri arasındaki farka bağlıdır.



Şekil 1. Lityum iyon pillerin bileşenleri ve çalışma mekanizması.

Lityum iyon pillerin temel bileşenleri; anot, katot, elektrolit ve ayırıcıdır.

Anot, pilin negatif elektrotudur ve genellikle grafit gibi karbon bazlı malzemelerden yapılır. Anotun görevi, lityum iyonlarını deşarj sırasında depolamak ve şarj sırasında serbest bırakmaktır. Bazı yaygın kullanılan anot materyalleri ve fiziksel özellikleri Tablo 1’de görülmektedir.

Tablo 1. Farklı anot malzemelerinin enerji yoğunluğu ve karşılık gelen ortalama voltajı.

Malzeme	Özgül Kapasite (mAhg ⁻¹)	Raporlanan Döngü Ömrü	Ortalama Gerilim (V)	Kaynak
Grafit (G)	372	>1000	0,1	(Cen vd., 2018)
Silisyum Bazlı (Si)	4200	100-200	0,4	(Marino vd., 2012)
Fosfor Bazlı (P)	2595	-	0,8	(Aslam vd., 2021)
Lityum Metal (Li)	3860	300	0,0	(Choi vd., 2020)
Titanyum Dioksit Bazlı	335	-	1,7	(Luo vd., 2012)

Katot, pilin pozitif elektrotudur ve genellikle lityum kobalt oksit (LiCoO₂), lityum mangan oksit (LiMn₂O₄) veya lityum demir fosfat (LiFePO₄) gibi lityum içeren metal oksitlerden yapılır. Katot, şarj sırasında lityum iyonlarını depolar ve deşarj sırasında serbest bırakır. Yaygın kullanılan bazı katot materyalleri ve fiziksel özellikleri Tablo 2’de görülmektedir.

Tablo 2. Li iyon bataryalarda en sık kullanılan katot malzemeleri ve bazı fiziksel özellikleri (Costa vd., 2019).

Katot Aktif Malzemesi	Kristal Sistemi/Uzay Grubu (Nokta Grubu)	Özgül Kapasite (mAh-g ⁻¹)	Tipik Voltaj Aralığı (V)
LiCoO ₂	Ortorombik/R3m [C _{3v}]	274	2,5-4,45
LiFePO ₄	Ortorombik/Pnma [D ₂ ^h]	170	2,5-4,2
LiMn ₂ O ₄	Kübik/Fd3m [O ^h]	148	3,0-4,3
LiNiO ₂	Trigonal/R3m [C _{3v}]	275	3,0-4,3
LiNi _{1-x} Co _x O ₂ (0.2 ≤ x ≤ 0.5)	Rhombohedral/R3m [C _{3v}]	~275	3,5-4,3
LiNi _{1/3} Mn _{1/3} Co _{1/3} O ₂	Rhombohedral/R3m [C _{3v}]	278	2,3-4,3
LiNi _{0.5} Mn _{1.5} O ₂	Trigonal/R3m [C _{3v}]	147	3,5-4,9

Elektrolit, Lityum-iyon pil performansını etkileyen önemli faktörlerden biridir. Son dönemde, özellikle düşük sıcaklıklarda çalışan piller için özel olarak tasarlanmış elektrolitler üzerine yoğunlaşmış araştırmalar bulunmaktadır (Das vd., 2023). Sıvı elektrolitler, LIB’lerde en yaygın kullanılan elektrolit türüdür. Ancak düşük sıcaklıklarda, viskozite artışı, iyon iletkenliğinin düşmesi ve katı elektrolit ara yüzey (SEI) oluşumu gibi sorunlarla karşılaşılır. Bu durum, pilin iç direncini yükselterek performansını düşürür. Bu nedenle, düşük sıcaklıklarda çalışan LIB’ler için uygun elektrolit mühendisliği çalışmaları oldukça önemlidir.

Sıvı elektrolitler genellikle üç ana bileşenden oluşur: lityum tuzu, çözücü ve katkı maddeleri. Çözücü, elektrolitin temel bileşenidir ve genellikle dietil karbonat (DEC), dimetil karbonat (DMC), etilen karbonat (EC), propilen karbonat (PC) ve vinil karbonat (VC) gibi organik karbonatlardan oluşur. Düşük sıcaklıklarda daha iyi performans elde etmek için, metil asetat (MA), metil propiyonat (MP), etil asetat (EA) ve propil asetat (PA) gibi daha düşük donma noktalı esterler gibi alternatif çözücüler araştırılmaktadır (Haregewoin vd., 2016).

Elektrolitlerde kullanılan farklı tuzlar ve çözücü karışımlarının pil performanslarını etkilediği yapılan çalışmalar sonucunda rapor edilmiştir. Örneğin 1M LiPF₆ tuzunun içerisinde çözüldüğü Fluoroethylene karbonat (FEC), DMC, EC ve EMC çözücülerinin farklı kombinasyonları LiNi_{0.5}Co_{0.2}Mn_{0.3}O₂ (NCM523) katot materyali ve Si/Gr anot materyali olarak kullanılan bir pilde elektrolit olarak denenmiş ve FEC:DMC karışımının diğer karışımlara göre daha yüksek kapasite sağladığı rapor edilmiştir (Zhao vd., 2021).

Ayırıcı, anot ve katot arasında fiziksel bir bariyer oluşturarak kısa devreyi önlerken, lityum iyonlarının geçişine izin verir. Ayırıcının gözenekli yapısı, iyonların serbestçe hareket etmesini sağlarken, elektronik iletkenliği engelleyerek pilin güvenliğini sağlar (S. S. Zhang, 2007). Bu dört bileşen, birlikte çalışarak lityum iyon pilinin enerji depolama ve boşaltma fonksiyonlarını yerine getirmesini sağlar.

3. Li-iyon Bataryaların Avantaj ve Dezavantajları

Lityum iyon piller, günümüzde enerji depolama alanında en yaygın kullanılan teknolojilerden biri haline gelmiştir. Bu popülerliğin ardında yatan sebep, diğer pil türlerine göre sunduğu çok sayıda avantajdır. Bu avantajlar, lityum iyon pillerini taşınabilir elektronik cihazlardan elektrikli araçlara ve yenilenebilir enerji depolama sistemlerine kadar geniş bir uygulama yelpazesi için ideal bir seçenek haline getirir. Lityum iyon pillerin avantaj ve dezavantajları Tablo 3’de görülmektedir.

Lityum iyon pillerinin en önemli avantajlarından biri, yüksek enerji yoğunluğudur. Bu, belirli bir ağırlık veya hacim için diğer pil türlerine göre daha fazla enerji depolayabildikleri anlamına gelir. Yüksek enerji yoğunluğu, daha küçük ve hafif pillerin üretilmesini sağlar, bu da özellikle taşınabilir elektronik cihazlar ve elektrikli araçlar için önemlidir. Örneğin, bir lityum iyon pil, aynı ağırlıktaki bir kurşun-asit pile göre yaklaşık üç kat daha fazla enerji depolayabilir. Bu sayede, akıllı telefonlar ve dizüstü bilgisayarlar gibi cihazlar daha uzun süre şarj edilmeden kullanılabilir ve elektrikli araçlar daha uzun mesafeler kat edebilir (Niu vd., 2024).

Lityum iyon pillerin bir diğer önemli avantajı, uzun çevrim ömrüdür. Bir pilin çevrim ömrü, pilin kaç kez şarj edilip deşarj edilebileceğinin bir ölçüsüdür. Lityum iyon piller, diğer pil türlerine göre daha uzun çevrim ömrüne sahiptir, bu da pillerin daha uzun süre dayanmasını sağlar (J. Zhang vd., 2024). Örneğin, bir lityum iyon pil, tipik olarak bir kurşun-asit pile göre çok daha uzun döngülerde çalışabilir (Dufo-López vd., 2021). Bu, lityum iyon pillerin daha az sıklıkla değiştirilmesi gerektiği anlamına gelir, bu da hem maliyet tasarrufu sağlar hem de çevresel etkiyi azaltır.

Bunların yanı sıra, lityum iyon pillerin düşük kendi kendine deşarj oranı da önemli bir avantajdır. Kendi kendine deşarj, pillerin kullanılmadıkları zamanlarda bile enerji kaybetme eğilimidir (Babu, 2024). Lityum iyon piller, diğer pil türlerine göre çok daha düşük bir kendi kendine deşarj oranına sahiptir, bu da pillerin daha uzun süre şarjlı kalmasını sağlar (Dunn vd., 2011; Larcher & Tarascon, 2014). Bu özellik, lityum iyon pillerini, uzun süre kullanılmayan cihazlar veya acil durum güç kaynakları için ideal bir seçenek haline getirir.

Son olarak, lityum iyon piller hafıza etkisinden etkilenmezler. Hafıza etkisi, pillerin tam olarak deşarj edilmeden şarj edilmeleri durumunda kapasitelerinin azalmasıdır (Ventosa vd., 2016). Lityum iyon pillerde bu sorun yaşanmaz, bu da pillerin herhangi bir zamanda şarj edilebilmesini ve performanslarının etkilenmemesini sağlar (Sasaki vd., 2013).

Tüm bu avantajlar, lityum iyon pillerini günümüzde enerji depolama alanında lider konuma getirmiştir. Teknolojinin sürekli gelişmesiyle birlikte, lityum iyon pillerin gelecekte daha da yaygınlaşması ve daha da gelişmiş özelliklere sahip olması beklenmektedir.

Lityum iyon piller, enerji depolama alanında devrim yaratmış ve birçok avantaj sunmalarına rağmen, bazı dezavantajlara da sahiptirler. Bu dezavantajlar, özellikle maliyet, güvenlik ve çevresel etki gibi konularda yoğunlaşmaktadır.

Lityum iyon pillerin en önemli dezavantajlarından biri, yüksek maliyetleridir. Diğer pil türlerine kıyasla, lityum iyon pillerin üretimi daha pahalıdır. Bu durum, lityum iyon pillerin kullanıldığı ürünlerin fiyatlarını da etkilemektedir. Örneğin, elektrikli araçların yüksek maliyetinin önemli bir kısmı, lityum iyon pillere atfedilebilir. Ayrıca, lityum iyon pillerin ömrü sınırlıdır ve belirli bir süre sonra değiştirilmeleri gerekir. Bu da ek bir maliyet unsuru oluşturur. Maliyetlerin düşürülmesi, lityum iyon pillerin daha yaygın olarak kullanılabilmesi için önemli bir hedeftir ve bu alanda araştırmalar devam etmektedir.

Bir diğer önemli dezavantaj ise güvenlik konusudur. Lityum iyon piller, aşırı şarj, aşırı deşarj, aşırı ısınma veya fiziksel hasar gibi durumlarda güvenlik sorunları oluşturabilir (Chombo & Laonual, 2020). Bu durumlar, pilin aşırı ısınmasına, alev almasına ve hatta patlamasına neden olabilir. Bu nedenle, lityum iyon pillerin kullanımı sırasında dikkatli olunması ve güvenlik önlemlerinin alınması önemlidir (Gandoman vd., 2019; Liang vd., 2020). Pil yönetim sistemleri, bu tür riskleri azaltmak için tasarlanmıştır ve pilin güvenli bir şekilde çalışmasını sağlar (Ramkumar vd., 2022).

Lityum iyon pillerin çevresel etkisi de göz ardı edilmemesi gereken bir konudur. Lityum iyon pillerin üretimi, lityum,

kobalt ve nikel gibi hammaddelerin çıkarılmasını ve işlenmesini gerektirir. Bu süreçler, çevresel sorunlara yol açabilir. Ayrıca, lityum iyon pillerin geri dönüşümü de zorlu bir süreçtir ve çevreye zarar verebilecek atıklar oluşturabilir. Örneğin pirometalurji adı verilen bir yöntemle yüksek sıcaklıklarda işlenmiş metallerin geri kazanımı hedeflenmektedir. Ancak yüksek sıcaklıklarda elektrolit ve bağlayıcı malzemelerin yanması sırasında toksik gazların salınması çevre için tehlike arz edebilmektedir (Piątek vd., 2021). Li-iyon bataryaların bileşenleri için bu yöntem sırasında daha az zararlı olan hidrometalurji yöntemi genel olarak yaygınlaşmaya başlamıştır (Harper vd., 2019). Lityum iyon pillerin çevresel etkisini azaltmak için, geri dönüşüm süreçlerinin geliştirilmesi ve daha çevre dostu malzemelerin kullanılması önemlidir (Piątek vd., 2021).

Son olarak, lityum iyon pillerin performansı sıcaklığa bağlı olarak değişebilir. Düşük sıcaklıklarda, pilin kapasitesi ve performansı azalabilir. Yüksek sıcaklıklarda ise, pilin ömrü kısalsabilir ve güvenlik sorunları ortaya çıkabilir. Bu nedenle, lityum iyon pillerin optimum sıcaklık aralığında kullanılması önemlidir. Örneğin yükseltilmiş sıcaklıkta döngü sırasında LiB'nin maksimum şarj depolama kapasitesinin artan bozulma oranının, esas olarak elektrotlardaki bozulmalarla ilişkili olduğu ve yükseltilmiş sıcaklıkta LiCoO₂ katodunun bozulmasının grafit anodundan daha büyük olduğu bulunmuştur (Leng vd., 2015).

Lityum iyon pillerin avantajları ve dezavantajları göz önünde bulundurularak, belirli bir uygulama için en uygun pil teknolojisinin seçilmesi önemlidir. Teknolojinin sürekli gelişmesiyle birlikte, lityum iyon pillerin dezavantajlarının azaltılması ve performanslarının artırılması beklenmektedir.

Tablo 3. Li-iyon pillerin avantaj ve dezavantajları (El Kharbachi vd., 2020; Nitta vd., 2015).

Avantajlar	Dezavantajlar
<ul style="list-style-type: none"> Kapalı hücre olması ve bakım gerektirmemesi Uzun ömürlü olması (300 – 500 çevrim) Geniş çalışma sıcaklık aralığı (-20 ila 60°C arası) Uzun raf ömrü (2 – 3 yıl) Çabuk şarj olabilme kabiliyeti Yüksek deşarj kapasitesi Yüksek enerji verimi (%98) Yüksek spesifik enerji ve enerji yoğunluğu Hafıza etkisinin olmayışı 	<ul style="list-style-type: none"> Fiyatı (Talebin artmasıyla fiyat azalmaktadır) Yüksek sıcaklıklarda bozulması Koruyucu devre ihtiyacının oluşu Aşırı şarj sonucunda kapasite kaybı veya termal bozulma

4. Li-iyon Pillerin Uygulama Alanları

Lityum iyon piller, yüksek enerji yoğunluğu, uzun çevrim ömrü ve düşük kendi kendine deşarj oranı gibi avantajları sayesinde günümüzde çok çeşitli alanlarda kullanılmaktadır. Taşınabilir elektronik cihazlardan elektrikli araçlara ve yenilenebilir enerji depolama sistemlerine kadar, lityum iyon piller modern yaşamın vazgeçilmez bir parçası haline gelmiştir.

Taşınabilir Elektronik Cihazlar: Lityum iyon piller, akıllı telefonlar, tabletler, dizüstü bilgisayarlar, dijital kameralar, giyilebilir teknolojiler ve diğer birçok taşınabilir elektronik cihazda yaygın olarak kullanılmaktadır. Bu cihazlarda lityum iyon pillerin tercih edilmesinin temel nedeni, küçük boyutları, hafiflikleri ve yüksek enerji kapasiteleridir. Bu sayede, cihazlar daha uzun süre şarj edilmeden kullanılabilir ve daha kompakt tasarımlar elde edilebilir.

Elektrikli Araçlar: Lityum iyon piller, elektrikli araçların (EA) gelişiminde kritik bir rol oynamaktadır. Elektrikli arabalar, hibrit arabalar, elektrikli bisikletler, elektrikli scooterlar ve elektrikli otobüsler gibi birçok EA türünde lityum iyon piller kullanılmaktadır. Lityum iyon pillerin yüksek enerji yoğunluğu, EA'ların daha uzun menziller kat etmesini sağlar. Ayrıca, hızlı şarj edilebilirlik özelliği ve uzun çevrim ömrü, EA'ların günlük kullanım için daha pratik hale gelmesine katkıda bulunur.

Yenilenebilir Enerji Depolama: Lityum iyon piller, güneş enerjisi ve rüzgâr enerjisi gibi yenilenebilir enerji kaynaklarının depolanmasında da önemli bir rol oynamaktadır. Güneş panelleri ve rüzgâr türbinleri tarafından üretilen enerji, lityum iyon pillerde depolanarak daha sonra kullanılabilir. Bu, yenilenebilir enerji kaynaklarının sürekliliğini ve güvenilirliğini artırır ve enerji şebekesinin dengesini sağlar. Ayrıca, evlerde ve işyerlerinde kullanılan güneş enerjisi sistemlerinde de lityum iyon piller tercih edilmektedir.

Diğer Uygulama Alanları: Lityum iyon piller, yukarıda belirtilen alanların yanı sıra birçok farklı sektörde de kullanılmaktadır. Bunlar arasında:

- **Endüstriyel ekipmanlar:** Forkliftler, elektrikli el aletleri ve diğer endüstriyel ekipmanlar
- **Tıbbi cihazlar:** Kalp pilleri, defibrilatörler ve insülin pompaları
- **Havacılık ve uzay:** Uydular, uçaklar ve insansız hava araçları
- **Askeri uygulamalar:** Haberleşme cihazları, gece görüş sistemleri ve insansız hava araçları

Lityum iyon pillerin uygulama alanları sürekli olarak genişlemekte ve yeni teknolojilerin geliştirilmesiyle birlikte daha da yaygınlaşması beklenmektedir.

5. Li-iyon Pillerin Geleceği

Lityum iyon piller, günümüzde enerji depolama alanında baskın teknoloji olsa da sürekli gelişen ihtiyaçlar ve teknolojik ilerlemeler, bu alanda yeni arayışlara yol açmaktadır. Gelecekte lityum iyon pillerin daha da gelişerek enerji depolama çözümlerindeki yerini koruması ve yeni uygulama alanlarında kullanılması beklenmektedir. Bu gelişim, malzeme bilimi, pil tasarımı ve üretim süreçlerindeki yeniliklerle mümkün olacaktır.

Malzeme bilimi alanındaki araştırmalar, lityum iyon pillerin enerji yoğunluğunu, güvenliğini ve ömrünü artırmaya odaklanmaktadır. Katot malzemelerinde lityum-nikel-mangan-kobalt oksit (NMC) ve lityum demir fosfat (LFP) gibi yeni nesil malzemelerin kullanımı yaygınlaşırken çok geniş yüzey alanlarına sahip olan metal-organik yapılar (MOF'lar; 700 – 2500 m²/g) gibi materyaller yeni katot malzemeleri olarak karşımıza çıkmaktadır (Kaushik vd., 2024). Bu malzemeler geleneksel katotlara kıyasla çeşitli avantajlar sunmaktadır. MOF'lar çok geniş bir spesifik yüzey alanına sahip oldukça gözenekli bir yapıya sahiptir, bu da lityum iyonlarının şarj ve deşarj sırasında elektrotun içine ve dışına hareket etmesi için gelişmiş verimlilik anlamına gelir. Bu da hem lityum iyonlarını depolamak için daha yüksek kapasite hem de daha hızlı şarj oranları sağlar (Q. Wang vd., 2015).

Anot malzemeleri arasında silikon (4200 mAh/g teorik kapasite; McDowell vd., 2013; Ozanam & Rosso, 2016) ve grafen (744 mAh/g teorik kapasite) gibi yüksek kapasiteli malzemeler üzerinde çalışmalar devam etmektedir (Yu vd., 2022; Zubi vd., 2018). Grafitin eksfoliyasyon ürünü olan grafen, sp² hibridizasyonuna sahip, üstün mekanik, termal ve elektriksel özellikler ortaya koyan bir tür iki boyutlu tek katmanlı karbon malzemedir (Guo vd., 2021). Dahası, kristal grafende lityumlaşmanın grafen tabakalarının iki tarafında gerçekleştiği kanıtlanmıştır, bu da teorik lityum depolama kapasitesinin grafitin iki katı olduğu anlamına gelmektedir (Rajkamal & Thapa, 2019).

Lityum iyon pillerde enerji yoğunluğunu artırmak amacıyla yüksek voltajlı katot malzemeleri kullanımı, sıvı elektrolitin yüksek voltaj koşullarında bozunması ve güvenlik endişeleri nedeniyle sınırlı kalmaktadır (Moradi vd., 2023). Bu doğrultuda, katı hal elektrolitleri, yüksek termal kararlılık, geniş elektrokimyasal kararlılık penceresi ve sızdırmazlık gibi üstün özellikleriyle güvenli ve yüksek performanslı piller için umut verici bir alternatif sunar (Yue vd., 2016). Yüksek iyonik iletkenlik ve düşük elektronik iletkenlik sayesinde hızlı şarj yeteneği de bu teknolojinin önemli avantajları arasındadır (Lanjan vd., 2020).

Pil tasarımındaki yenilikler de lityum iyon pillerin geleceğini şekillendirecek önemli bir faktördür. Üç boyutlu pil yapıları, daha yüksek enerji yoğunluğu ve daha hızlı şarj sağlayarak özellikle elektrikli araçlar ve taşınabilir elektronik cihazlar için önemli avantajlar sunabilir. Ayrıca, mikro ölçekli piller, giyilebilir teknolojiler, tıbbi implantlar ve sensörler gibi küçük ölçekli cihazlarda kullanım için yeni olanaklar yaratabilir. Üretim süreçlerindeki gelişmeler, lityum iyon pillerin maliyetini düşürerek daha erişilebilir hale gelmesini sağlayabilir. Otomasyon ve yapay zekâ gibi teknolojilerin üretim süreçlerine entegrasyonu, verimliliği artırarak maliyetleri düşürebilir ve üretim hızını artırabilir. Ayrıca, geri dönüşüm teknolojilerindeki gelişmeler, lityum iyon pillerin çevresel etkisini azaltarak sürdürülebilirliğini artırabilir.

Lityum iyon pillerin geleceği, bu teknolojinin sınırlarını zorlayan ve yeni ufuklar açan sürekli araştırmalar ve geliştirmelerle şekillenecektir. Enerji depolama alanındaki artan talebin karşılanması ve yeni teknolojilerin geliştirilmesi, lityum iyon pillerin gelecekte de önemli bir rol oynayacağını göstermektedir.

6. Lityum İyon Pillerin Ötesinde

Lityum iyon piller, günümüzde enerji depolama alanında önemli bir yer tutsa da araştırmacılar sürekli olarak daha iyi performans, güvenlik ve sürdürülebilirlik sunabilecek yeni pil teknolojileri geliştirmek için çalışmaktadır. Bu çalışmalar, lityum iyon pillerin sınırlamalarını aşmayı ve gelecekteki enerji ihtiyaçlarını karşılamayı hedeflemektedir. İşte lityum iyon pillerin

ötesinde umut vadeden bazı pil teknolojileri:

a. Katı Hal Piller:

Katı hal piller, geleneksel lityum iyon pillerdeki sıvı elektrolitin yerine katı bir elektrolit kullanır (Schmaltz vd., 2023). Bu, pilin güvenliğini önemli ölçüde artırır, çünkü yanıcı sıvı elektrolitlerin neden olabileceği yangın riskini ortadan kaldırır. Ayrıca, katı hal elektrolitleri daha yüksek enerji yoğunluğuna olanak tanır ve pilin ömrünü uzatabilir. Katı hal piller, elektrikli araçlar, taşınabilir elektronik cihazlar ve enerji depolama sistemleri gibi çeşitli uygulamalar için gelecek vadeden bir teknoloji olarak kabul edilmektedir (Bates vd., 2022).

b. Lityum-Sülfür Piller:

Lityum-sülfür piller, lityum iyon pillere göre daha yüksek teorik enerji yoğunluğuna sahiptir. Bu, aynı ağırlıkta veya hacimde daha fazla enerji depolayabilecekleri anlamına gelir. Lityum-sülfür piller, özellikle elektrikli havacılık ve uzay araştırmaları gibi ağırlığın önemli bir faktör olduğu uygulamalar için cazip bir seçenektir. Ancak, lityum-sülfür pillerin çevrim ömrü ve performansının iyileştirilmesi için hala bazı zorlukların üstesinden gelinmesi gerekmektedir (Bi vd., 2023; Castillo vd., 2023; Fan vd., 2018).

c. Sodyum-İyon Piller:

Sodyum-iyon piller, lityum iyon pillerle benzer bir çalışma prensibine sahiptir, ancak lityum yerine sodyum kullanır. Sodyum, lityuma göre daha bol ve daha ucuz bir elementtir, bu da sodyum-iyon pillerin daha düşük maliyetli olmasını sağlar. Sodyum-iyon piller, özellikle büyük ölçekli enerji depolama sistemleri ve elektrikli araçlar için potansiyel bir alternatif olarak görülmektedir (Y. Wang vd., 2019).

d. Metal-Hava Piller:

Metal-hava piller, metal anot ve hava katodu kullanır. Bu, çok yüksek teorik enerji yoğunluğuna sahip pillerin üretilmesini sağlar. Lityum-hava ve çinko-hava pilleri gibi metal-hava pilleri, özellikle elektrikli araçlar için uzun menzil sağlayabilir. Ancak, metal-hava pillerinin pratik uygulamalarda kullanılabilmesi için çevrim ömrü, verimlilik ve maliyet gibi konularda iyileştirmeler yapılması gerekmektedir (T. Li vd., 2023; Olabi vd., 2021; Rahman vd., 2013).

e. Redoks Akış Pilleri:

Redoks akış pilleri, enerjiyi kimyasal olarak depolanan sıvı elektrolitlerde depolar. Bu piller, büyük ölçekli enerji depolama uygulamaları için uygundur ve uzun ömürlüdür. Ayrıca, redoks akış pilleri güvenlidir ve çevre dostudur (Pan & Wang, 2015; Weber vd., 2011).

Bu teknolojilerin yanı sıra, sürekli olarak yeni pil kimyaları ve tasarımları araştırılmaktadır. Gelecekte, bu yeni pil teknolojilerinin lityum iyon pillerin yerini alması veya lityum iyon pillerle birlikte kullanılması beklenmektedir. Hangi teknolojinin ön plana çıkacağı, performans, maliyet, güvenlik ve sürdürülebilirlik gibi faktörlere bağlı olacaktır.

Sonuç

Lityum iyon piller, taşınabilir elektronik cihazlardan elektrikli araçlara ve yenilenebilir enerji depolama sistemlerine kadar geniş bir uygulama yelpazesinde devrim yaratarak modern yaşamın vazgeçilmez bir parçası haline gelmiştir. Bu makalede, lityum iyon pillerin tarihsel gelişiminden başlayarak, çalışma prensipleri, avantajları, dezavantajları ve gelecekteki potansiyeli detaylı bir şekilde incelenmiştir.

Bağdat Pili gibi antik dönem örneklerinden Alessandro Volta'nın volta piline ve günümüzdeki gelişmiş lityum iyon pillere kadar uzanan tarihsel yolculuk, pil teknolojilerinin insanlık için önemini ve sürekli gelişimini gözler önüne sermektedir. Lityum iyon pillerin yüksek enerji yoğunluğu, uzun çevrim ömrü ve düşük kendi kendine deşarj oranı gibi avantajları, onları diğer pil teknolojilerine göre öne çıkarmaktadır. Ancak, maliyet, güvenlik ve çevresel etki gibi dezavantajların da göz ardı edilmemesi gerekmektedir.

Lityum iyon pil teknolojisi sürekli olarak gelişmekte ve gelecekte daha da iyi performans, güvenlik ve sürdürülebilirlik sağlaması beklenmektedir. Yeni malzemelerin keşfi, pil tasarımının optimize edilmesi ve akıllı pil yönetim sistemlerinin geliştirilmesi, bu alanda yapılan çalışmalara örnek olarak verilebilir. Katı hal piller, lityum-sülfür piller ve sodyum-iyon piller gibi alternatif teknolojiler de gelecekte enerji depolama alanında önemli bir rol oynayabilir.

Sonuç olarak, lityum iyon piller, enerji depolama alanında önemli bir yere sahip olmaya devam edecek ve teknolojik gelişmelerle birlikte daha da yaygınlaşacaktır. Lityum iyon pillerinin dezavantajlarının giderilmesi için yapılacak bilimsel çalışmalar bu pillerin daha yaygın hale gelmesine ve öne çıkmasına yol açacaktır. Bu teknolojinin gelecekteki potansiyeli, araştırma ve geliştirme çalışmalarına devam edilmesiyle daha da ortaya çıkacaktır.

Hakem Değerlendirmesi: Dış bağımsız.

Yazar Katkıları: Fikir-MY, EÖ, HP; Tasarım-MY, HP; Denetleme-MY, EÖ; Kaynaklar- HP, EÖ; Veri Toplanması ve/veya İşlemesi- HP; Analiz ve/veya Yorum- HP, MY, EÖ; Literatür Taraması- HP, EÖ; Yazıyı Yazan- HP; Eleştirel İnceleme- MY, EÖ; Diğer- MY, EÖ, HP.

Çıkar Çatışması: Yazarlar, çıkar çatışması olmadığını beyan etmiştir.

Finansal Destek: Bu çalışma için herhangi bir kurumdan finansal destek alınmamıştır.

Peer-review: Externally peer-reviewed.

Author Contributions: Concept - MY, EÖ, HP; Design- MY, HP; Supervision- MY, EÖ; Resources- HP, EÖ; Data Collection and/or Processing- HP; Analysis and/or Interpretation- HP, MY, EÖ; Literature Search- HP, EÖ; Writing Manuscript- HP; Critical Review- MY, EÖ; Other- MY, EÖ, HP.

Conflict of Interest: The authors have no conflicts of interest to declare.

Financial Disclosure: No financial support was received from any institution for this study.

Kaynaklar

- Abdelaal, M. M., & Alkhedher, M. (2024). Dual optimization of LiFePO₄ cathode performance using manganese substitution and a hybrid lithiated Nafion-modified PEDOT:PSS coating layer for lithium-ion batteries. *Electrochimica Acta*, 506, 145050. <https://doi.org/10.1016/J.ELECTACTA.2024.145050>
- Ahmed, S., Nelson, P. A., Gallagher, K. G., Susarla, N., & Dees, D. W. (2017). Cost and energy demand of producing nickel manganese cobalt cathode material for lithium ion batteries. *Journal of Power Sources*, 342, 733-740. <https://doi.org/10.1016/J.JPOWSOUR.2016.12.069>
- Armand, M., & Tarascon, J. M. (2008). Building better batteries. *Nature* 2008 451:7179, 451(7179), 652-657. <https://doi.org/10.1038/451652a>
- Arya, S., & Verma, S. (2020). Nickel-Metal Hydride (Ni-MH) Batteries. İçinde *Rechargeable Batteries*. <https://doi.org/10.1002/9781119714774.ch8>
- Aslam, M. K., Niu, Y., Hussain, T., Tabassum, H., Tang, W., Xu, M., & Ahuja, R. (2021). How to avoid dendrite formation in metal batteries: Innovative strategies for dendrite suppression. *Nano Energy*, 86, 106142. <https://doi.org/10.1016/J.NANOEN.2021.106142>
- Babu, B. (2024). Self-discharge in rechargeable electrochemical energy storage devices. *Energy Storage Materials*, 67, 103261. <https://doi.org/10.1016/J.ENSME.2024.103261>
- Bates, A. M., Preger, Y., Torres-Castro, L., Harrison, K. L., Harris, S. J., & Hewson, J. (2022). Are solid-state batteries safer than lithium-ion batteries? İçinde *Joule* (C. 6, Sayı 4). <https://doi.org/10.1016/j.joule.2022.02.007>
- Bi, C. X., Hou, L. P., Li, Z., Zhao, M., Zhang, X. Q., Li, B. Q., Zhang, Q., & Huang, J. Q. (2023). Protecting lithium metal anodes in lithium-sulfur batteries: A review. *Energy Material Advances*, 4. <https://doi.org/10.34133/energymatadv.0010>
- Castillo, J., Coca-Clemente, J. A., Rikarte, J., Sáenz De Buruaga, A., Santiago, A., & Li, C. (2023). Recent progress on lithium anode protection for lithium-sulfur batteries: Review and perspective. İçinde *APL Materials* (C. 11, Sayı 1). <https://doi.org/10.1063/5.0107648>
- Cecchini, R., & Pelosi, G. (1992). From the Historian--Alessandro Volta and his battery. *IEEE Antennas and Propagation Magazine*, 34(2). <https://doi.org/10.1109/74.134307>
- Cen, Y., Sisson, R. D., Qin, Q., & Liang, J. (2018). Current Progress of Si/Graphene Nanocomposites for Lithium-Ion Batteries. *C 2018, Vol. 4, Page 18, 4(1)*, 18. <https://doi.org/10.3390/C4010018>
- Chawla, N., Bharti, N., & Singh, S. (2019). Recent Advances in Non-Flammable Electrolytes for Safer Lithium-Ion Batteries. *Batteries 2019, Vol. 5, Page 19, 5(1)*, 19. <https://doi.org/10.3390/BATTERIES5010019>
- Choi, S. Il, Jung, E. J., Park, M., Shin, H. S., Huh, S., & Won, Y. S. (2020). Phase-dependent performance of lotus-root shaped TiO₂ anode for lithium-ion batteries (LIBs). *Applied Surface Science*, 508, 145237. <https://doi.org/10.1016/J.APSUSC.2019.145237>
- Chombo, P. V., & Laonual, Y. (2020). A review of safety strategies of a Li-ion battery. *Journal of Power Sources*, 478, 228649. <https://doi.org/10.1016/J.JPOWSOUR.2020.228649>
- Costa, C. M., Gonçalves, R., & Lanceros-Méndez, S. (2019). Advances in Cathode Nanomaterials for Lithium-Ion Batteries.

- İçinde *Nanostructured Materials for Next-Generation Energy Storage and Conversion* (ss. 105-145). Springer Berlin Heidelberg. https://doi.org/10.1007/978-3-662-58675-4_3
- Crabtree, G., Kócs, E., & Trahey, L. (2015). The energy-storage frontier: Lithium-ion batteries and beyond. *MRS Bulletin*, 40(12). <https://doi.org/10.1557/mrs.2015.259>
- Das, D., Manna, S., & Puravankara, S. (2023). Electrolytes, Additives and Binders for NMC Cathodes in Li-Ion Batteries—A Review. İçinde *Batteries* (C. 9, Sayı 4). <https://doi.org/10.3390/batteries9040193>
- Dong, B., Poletayev, A. D., Cottom, J. P., Castells-Gil, J., Spencer, B. F., Li, C., Zhu, P., Chen, Y., Price, J. M., Driscoll, L. L., Allan, P. K., Kendrick, E., Islam, M. S., & Slater, P. R. (2024). Effects of sulfate modification of stoichiometric and lithium-rich LiNiO₂ cathode materials. *Journal of Materials Chemistry A*, 12(19), 11390-11402. <https://doi.org/10.1039/D4TA00284A>
- Dufo-López, R., Cortés-Arcos, T., Artal-Sevil, J. S., & Bernal-Agustín, J. L. (2021). Comparison of Lead-Acid and Li-Ion Batteries Lifetime Prediction Models in Stand-Alone Photovoltaic Systems. *Applied Sciences* 2021, Vol. 11, Page 1099, 11(3), 1099. <https://doi.org/10.3390/APP11031099>
- Dunn, B., Kamath, H., & Tarascon, J. M. (2011). Electrical energy storage for the grid: A battery of choices. *Science*, 334(6058), 928-935. https://doi.org/10.1126/SCIENCE.1212741/SUPPL_FILE/DUNN-SOM.PDF
- El Kharbachi, A., Zavorotynska, O., Lacroche, M., Cuevas, F., Yartys, V., & Fichtner, M. (2020). Exploits, advances and challenges benefiting beyond Li-ion battery technologies. *Journal of Alloys and Compounds*, 817, 153261. <https://doi.org/10.1016/J.JALLCOM.2019.153261>
- Fan, X., Sun, W., Meng, F., Xing, A., & Liu, J. (2018). Advanced chemical strategies for lithium–sulfur batteries: A review. İçinde *Green Energy and Environment* (C. 3, Sayı 1). <https://doi.org/10.1016/j.gee.2017.08.002>
- Gandoman, F. H., Jaguemont, J., Goutam, S., Gopalakrishnan, R., Firouz, Y., Kalogiannis, T., Omar, N., & Van Mierlo, J. (2019). Concept of reliability and safety assessment of lithium-ion batteries in electric vehicles: Basics, progress, and challenges. *Applied Energy*, 251, 113343. <https://doi.org/10.1016/J.APENERGY.2019.113343>
- Goodenough, J. B., & Park, K. S. (2013). The Li-ion rechargeable battery: A perspective. *Journal of the American Chemical Society*, 135(4), 1167-1176. https://doi.org/10.1021/JA3091438/ASSET/IMAGES/JA-2012-091438_M014.GIF
- Guo, B., Ji, X., Wang, W., Chen, X., Wang, P., Wang, L., & Bai, J. (2021). Highly flexible, thermally stable, and static dissipative nanocomposite with reduced functionalized graphene oxide processed through 3D printing. *Composites Part B: Engineering*, 208, 108598. <https://doi.org/10.1016/J.COMPOSITESB.2020.108598>
- Haregewoin, A. M., Wotango, A. S., & Hwang, B. J. (2016). Electrolyte additives for lithium ion battery electrodes: progress and perspectives. *Energy & Environmental Science*, 9(6), 1955-1988. <https://doi.org/10.1039/C6EE00123H>
- Harper, G., Sommerville, R., Kendrick, E., Driscoll, L., Slater, P., Stolkin, R., Walton, A., Christensen, P., Heidrich, O., Lambert, S., Abbott, A., Ryder, K., Gaines, L., & Anderson, P. (2019). Recycling lithium-ion batteries from electric vehicles. *Nature* 2019 575:7781, 575(7781), 75-86. <https://doi.org/10.1038/s41586-019-1682-5>
- Iturrondobeitia, A., Aguesse, F., Genies, S., Waldmann, T., Kasper, M., Ghanbari, N., Wohlfahrt-Mehrens, M., & Bekaert, E. (2017). Post-Mortem Analysis of Calendar-Aged 16 Ah NMC/Graphite Pouch Cells for EV Application. *Journal of Physical Chemistry C*, 121(40). <https://doi.org/10.1021/acs.jpcc.7b05416>
- Kaushik, S., Chand, P., & Sharma, S. (2024). High-performance pristine ZIF-67 asymmetric supercapacitor device with excellent energy and power density for energy storage application. *Electrochimica Acta*, 497, 144565. <https://doi.org/10.1016/J.ELECTACTA.2024.144565>
- Kim, H. J., Krishna, T. N. V., Zeb, K., Rajangam, V., Muralee Gopi, C. V. V., Sambasivam, S., Raghavendra, K. V. G., & Obaidat, I. M. (2020). A comprehensive review of li-ion battery materials and their recycling techniques. İçinde *Electronics (Switzerland)* (C. 9, Sayı 7). <https://doi.org/10.3390/electronics9071161>
- Kordesch, K., & Taucher-Mautner, W. (2009). Primary Batteries - Aqueous Systems | Leclanché and Zinc-Carbon. İçinde *Encyclopedia of Electrochemical Power Sources*. <https://doi.org/10.1016/B978-044452745-5.00097-6>
- Lanjan, A., Ghalami Choobar, B., & Amjad-Iranagh, S. (2020). Promoting lithium-ion battery performance by application of crystalline cathodes LixMn1-zFezPO4. *Journal of Solid State Electrochemistry*, 24(1), 157-171. <https://doi.org/10.1007/S10008-019-04480-6/TABLES/5>
- Larcher, D., & Tarascon, J. M. (2014). Towards greener and more sustainable batteries for electrical energy storage. *Nature Chemistry* 2014 7:1, 7(1), 19-29. <https://doi.org/10.1038/nchem.2085>
- Leng, F., Tan, C. M., & Pecht, M. (2015). Effect of Temperature on the Aging rate of Li Ion Battery Operating above Room Temperature. *Scientific Reports* 2015 5:1, 5(1), 1-12. <https://doi.org/10.1038/srep12967>
- Li, M., Lu, J., Chen, Z., & Amine, K. (2018). 30 Years of Lithium-Ion Batteries. *Advanced Materials*, 30(33), 1800561.

- <https://doi.org/10.1002/ADMA.201800561>
- Li, T., Huang, M., Bai, X., & Wang, Y. X. (2023). Metal–air batteries: A review on current status and future applications. İçinde *Progress in Natural Science: Materials International* (C. 33, Sayı 2). <https://doi.org/10.1016/j.pnsc.2023.05.007>
- Liang, H., Zuo, X., Zhang, L., Huang, W., Chen, Q., Zhu, T., Liu, J., & Nan, J. (2020). Nonflammable LiTFSI-Ethylene Carbonate/1,2-Dimethoxyethane Electrolyte for High-Safety Li-ion Batteries. *Journal of The Electrochemical Society*, 167(9), 090520. <https://doi.org/10.1149/1945-7111/AB8803>
- Lu, X., & Anariba, F. (2014). Fostering innovation through an active learning activity inspired by the baghdad battery. *Journal of Chemical Education*, 91(11), 1929-1933. https://doi.org/10.1021/ED400869C/SUPPL_FILE/ED400869C_SI_002.DOCX
- Luo, J., Zhao, X., Wu, J., Jang, H. D., Kung, H. H., & Huang, J. (2012). Crumpled graphene-encapsulated Si nanoparticles for lithium ion battery anodes. *Journal of Physical Chemistry Letters*, 3(13), 1824-1829. https://doi.org/10.1021/JZ3006892/SUPPL_FILE/JZ3006892_SI_001.PDF
- Lyu, Y., Wu, X., Wang, K., Feng, Z., Cheng, T., Liu, Y., Wang, M., Chen, R., Xu, L., Zhou, J., Lu, Y., & Guo, B. (2021). An Overview on the Advances of LiCoO₂ Cathodes for Lithium-Ion Batteries. İçinde *Advanced Energy Materials* (C. 11, Sayı 2). <https://doi.org/10.1002/aenm.202000982>
- Marino, C., Boulet, L., Gaveau, P., Fraisse, B., & Monconduit, L. (2012). Nanoconfined phosphorus in mesoporous carbon as an electrode for Li-ion batteries: performance and mechanism. *Journal of Materials Chemistry*, 22(42), 22713-22720. <https://doi.org/10.1039/C2JM34562E>
- McDowell, M. T., Lee, S. W., Nix, W. D., & Cui, Y. (2013). 25th Anniversary Article: Understanding the Lithiation of Silicon and Other Alloying Anodes for Lithium-Ion Batteries. *Advanced Materials*, 25(36), 4966-4985. <https://doi.org/10.1002/ADMA.201301795>
- Mizushima, K., Jones, P. C., Wiseman, P. J., & Goodenough, J. B. (1980). Li_xCoO₂ (0 < x < 1): A new cathode material for batteries of high energy density. *Materials Research Bulletin*, 15(6), 783-789. [https://doi.org/10.1016/0025-5408\(80\)90012-4](https://doi.org/10.1016/0025-5408(80)90012-4)
- Moradi, Z., Lanjan, A., Tyagi, R., & Srinivasan, S. (2023). Review on current state, challenges, and potential solutions in solid-state batteries research. *Journal of Energy Storage*, 73, 109048. <https://doi.org/10.1016/J.EST.2023.109048>
- Nitta, N., Wu, F., Lee, J. T., & Yushin, G. (2015). Li-ion battery materials: present and future. *Materials Today*, 18(5), 252-264. <https://doi.org/10.1016/J.MATTOD.2014.10.040>
- Niu, H., Zhang, N., Lu, Y., Zhang, Z., Li, M., Liu, J., Song, W., Zhao, Y., & Miao, Z. (2024). Strategies toward the development of high-energy-density lithium batteries. *Journal of Energy Storage*, 88, 111666. <https://doi.org/10.1016/J.EST.2024.111666>
- Olabi, A. G., Sayed, E. T., Wilberforce, T., Jamal, A., Alami, A. H., Elsaid, K., Rahman, S. M. A., Shah, S. K., & Abdelkareem, M. A. (2021). Metal-air batteries—a review. İçinde *Energies* (C. 14, Sayı 21). <https://doi.org/10.3390/en14217373>
- Orangi, S., Manjong, N., Clos, D. P., Usai, L., Burheim, O. S., & Strømman, A. H. (2024). Historical and prospective lithium-ion battery cost trajectories from a bottom-up production modeling perspective. *Journal of Energy Storage*, 76, 109800. <https://doi.org/10.1016/J.EST.2023.109800>
- Ozanam, F., & Rosso, M. (2016). Silicon as anode material for Li-ion batteries. *Materials Science and Engineering: B*, 213, 2-11. <https://doi.org/10.1016/J.MSEB.2016.04.016>
- Pan, F., & Wang, Q. (2015). Redox species of redox flow batteries: A review. İçinde *Molecules* (C. 20, Sayı 11). <https://doi.org/10.3390/molecules201119711>
- Piątek, J., Afyon, S., Budnyak, T. M., Budnyk, S., Sipponen, M. H., & Slabon, A. (2021). Sustainable Li-Ion Batteries: Chemistry and Recycling. *Advanced Energy Materials*, 11(43), 2003456. <https://doi.org/10.1002/AENM.202003456>
- Rahman, Md. A., Wang, X., & Wen, C. (2013). High Energy Density Metal-Air Batteries: A Review. *Journal of The Electrochemical Society*, 160(10). <https://doi.org/10.1149/2.062310jes>
- Rajkamal, A., & Thapa, R. (2019). Carbon Allotropes as Anode Material for Lithium-Ion Batteries. *Advanced Materials Technologies*, 4(10), 1900307. <https://doi.org/10.1002/ADMT.201900307>
- Ramkumar, M. S., Reddy, C. S. R., Ramakrishnan, A., Raja, K., Pushpa, S., Jose, S., & Jayakumar, M. (2022). Review on Li-Ion Battery with Battery Management System in Electrical Vehicle. *Advances in Materials Science and Engineering*, 2022(1), 3379574. <https://doi.org/10.1155/2022/3379574>
- Sasaki, T., Ukyo, Y., & Novák, P. (2013). Memory effect in a lithium-ion battery. *Nature Materials* 2013 12:6, 12(6), 569-575. <https://doi.org/10.1038/nmat3623>
- Schmaltz, T., Hartmann, F., Wicke, T., Weymann, L., Neef, C., & Janek, J. (2023). A Roadmap for Solid-State Batteries. *Advanced Energy Materials*, 13(43). <https://doi.org/10.1002/aenm.202301886>

- Tsai, P. J., & Chan, S. L. I. (2013). Nickel-based batteries: materials and chemistry. İçinde *Electricity Transmission, Distribution and Storage Systems*. <https://doi.org/10.1533/9780857097378.3.309>
- Ventosa, E., Löffler, T., La Mantia, F., & Schuhmann, W. (2016). Understanding memory effects in Li-ion batteries: evidence of a kinetic origin in TiO₂ upon hydrogen annealing. *Chemical Communications*, 52(77), 11524-11526. <https://doi.org/10.1039/C6CC06070F>
- Wang, Q., Zou, R., Xia, W., Ma, J., Qiu, B., Mahmood, A., Zhao, R., Yang, Y., Xia, D., & Xu, Q. (2015). Facile Synthesis of Ultrasmall CoS₂ Nanoparticles within Thin N-Doped Porous Carbon Shell for High Performance Lithium-Ion Batteries. *Small*, 11(21), 2511-2517. <https://doi.org/10.1002/SMLL.201403579>
- Wang, Y., Song, S., Xu, C., Hu, N., Molenda, J., & Lu, L. (2019). Development of solid-state electrolytes for sodium-ion battery—A short review. *Nano Materials Science*, 1(2). <https://doi.org/10.1016/j.nanoms.2019.02.007>
- Weber, A. Z., Mench, M. M., Meyers, J. P., Ross, P. N., Gostick, J. T., & Liu, Q. (2011). Redox flow batteries: A review. İçinde *Journal of Applied Electrochemistry* (C. 41, Sayı 10). <https://doi.org/10.1007/s10800-011-0348-2>
- Whittingham, M. S. (1974). Electrointercalation in transition-metal disulphides. *Journal of the Chemical Society, Chemical Communications*, 9, 328-329. <https://doi.org/10.1039/C39740000328>
- Winter, M., Barnett, B., & Xu, K. (2018). Before Li Ion Batteries. *Chemical Reviews*, 118(23), 11433-11456. https://doi.org/10.1021/ACS.CHEMREV.8B00422/ASSET/IMAGES/LARGE/CR-2018-00422Q_0014.JPEG
- Yu, S., Guo, B., Zeng, T., Qu, H., Yang, J., & Bai, J. (2022). Graphene-based lithium-ion battery anode materials manufactured by mechanochemical ball milling process: A review and perspective. *Composites Part B: Engineering*, 246, 110232. <https://doi.org/10.1016/J.COMPOSITESB.2022.110232>
- Yuan, H., Luan, J., Liu, J., & Zhong, C. (2024). Hail to Daniell Cell: From Electrometallurgy to Electrochemical Energy Storage. İçinde *Advanced Functional Materials* (C. 34, Sayı 33). <https://doi.org/10.1002/adfm.202400289>
- Yue, L., Ma, J., Zhang, J., Zhao, J., Dong, S., Liu, Z., Cui, G., & Chen, L. (2016). All solid-state polymer electrolytes for high-performance lithium ion batteries. *Energy Storage Materials*, 5, 139-164. <https://doi.org/10.1016/J.ENSM.2016.07.003>
- Zhang, J., Huang, H., Zhang, G., Dai, Z., Wen, Y., & Jiang, L. (2024). Cycle life studies of lithium-ion power batteries for electric vehicles: A review. *Journal of Energy Storage*, 93, 112231. <https://doi.org/10.1016/J.EST.2024.112231>
- Zhang, S. S. (2007). A review on the separators of liquid electrolyte Li-ion batteries. İçinde *Journal of Power Sources* (C. 164, Sayı 1). <https://doi.org/10.1016/j.jpowsour.2006.10.065>
- Zhao, E., Gu, Y., Fang, S., Yang, L., & Hirano, S. I. (2021). Systematic Investigation of Electrochemical Performances for Lithium-Ion Batteries with Si/Graphite Anodes: Effect of Electrolytes Based on Fluoroethylene Carbonate and Linear Carbonates. *ACS Applied Energy Materials*, 4(3), 2419-2429. https://doi.org/10.1021/ACSAEM.0C02946/ASSET/IMAGES/LARGE/AE0C02946_0009.JPEG
- Zhu, L., & Chen, M. (2020). Research on spent LiFePO₄ electric vehicle battery disposal and its life cycle inventory collection in China. *International Journal of Environmental Research and Public Health*, 17(23). <https://doi.org/10.3390/ijerph17238828>
- Zubi, G., Dufo-López, R., Carvalho, M., & Pasaoglu, G. (2018). The lithium-ion battery: State of the art and future perspectives. *Renewable and Sustainable Energy Reviews*, 89, 292-308. <https://doi.org/10.1016/J.RSER.2018.03.002>